Theory and Application of Source Independent Full Wavefield Elastic Converted Phase Seismic Imaging and Velocity Analysis

by

Andrey Hanan Shabelansky

B.S. Geophysics and Mathematics, Tel-Aviv University, Israel (2005)
M.S. Geophysics, Tel-Aviv University, Israel (2007)

Submitted to the Department of Earth, Atmospheric and Planetary Sciences
in partial fulfillment of the requirements for the degree of
Doctor of Philosophy
at the
MASSACHUSETTS INSTITUTE OF TECHNOLOGY
February 2015 [June 2015]

Signature redacted
Author ....
Department of Earth, Atmospheric and Planetary Sciences
February 13, 2015

Signature redacted
Certified by ....
Alison E. Malcolm
Associate Professor
Thesis Supervisor

Signature redacted
Certified by ....
Michael C. Fehler
Senior Research Scientist
Thesis Supervisor

Signature redacted
Accepted by ....
Robert van der Hilst
Schlumberger Professor of Earth Sciences
Head, Department of Earth, Atmospheric and Planetary Sciences

Dedicated
to my Loving Parents,
David and Marina Shabelansky
and
to the memory of my Elder Brother,
Mark Shabelansky (1973-1988)

Theory and Application of Source Independent Full Wavefield Elastic Converted Phase Seismic Imaging and Velocity Analysis

by

Andrey Hanan Shabelansky

Submitted to the Department of Earth, Atmospheric and Planetary Sciences
on February 13, 2015, in partial fulfillment of the
requirements for the degree of
Doctor of Philosophy

Abstract

The recorded seismic signal contains full information about the source that generated the seismic waves and the path along which the seismic waves travel and interfere with subsurface. However, source information is not an explicit part of the seismic record and thus is a large source of uncertainty in seismic imaging and velocity analysis applications. In this thesis, we develop source-independent methods for seismic imaging, seismic trace interpolation and velocity analysis using the interference between pure (PP and SS) and converted-phase (PS and SP) waves. For seismic imaging, we develop amplitude-balancing source-independent converted-phase seismic imaging conditions and introduce a concept of conversion ratio coefficients to provide a physical and mathematical foundation for source-independent converted-phase (SICP) imaging. For seismic trace interpolation, we develop a scheme for migration/de-migration to suppress migration-based artifacts due to sparse station deployments. For velocity analysis, we present first a source-independent space-lag domain Extended SICP imaging condition (ESICP-IC). Then, we mathematically derive an optimization scheme for source independent converted-phase wave equation migration velocity analysis (SICP-WEMVA). We investigate numerically the stability and convergence of SICP-ICs, SICP interpolation and SICP-WEMVA with synthetic data. Finally, using the developed methodologies, we investigate the subsurface structure of the Hengill geothermal area in Iceland using the abundant micro-seismic activity of the region. The constructed SICP seismic images show detailed subsurface structure of the Hengill area that is well correlated with previous seismic and resistivity studies. Also, we find that the amplitudes of the images are well correlated with a low resistivity region of the geothermal area. The reason for this correlation is not fully understood, but may provide an additional tool for investigation of the Hengill site.

Thesis Supervisor: Alison E. Malcolm

Title: Associate Professor

Thesis Supervisor: Michael C. Fehler
Title: Senior Research Scientist

Acknowledgements

This is an immense pleasure for me to recollect the years I spent at MIT and to thank all people who have been part of this journey and influenced my life in their special ways.

First of all, I would like to thank my supervisors Prof. Alison Malcolm and Dr. Mike Fehler, without whom this thesis would not be possible. Their guidance, support and feedback helped me to become a better scientist and researcher, and I am very much thankful to them for that. In particular, I am very grateful to Alison that her door was always open to discuss new ideas and to chat about theoretical and analytical aspects of my research. To Mike, I am so thankful for his encouragement and for exposing me to the areas of micro-seismicity and geothermal. Thank you so much Alison and Mike.

I am very much indebted to Dr. Yves Bernabé and Dr. Bill Rodi. Yves revealed to me the world of rock physics and took my curiosity far beyond my initial research interests (second general exam project), for what I am so thankful to him. Bill has been my informal co-advisor and made my last several years very exciting and inspiring with broadening my interests in the area of geophysical inverse/optimization theory. Bill and Yves are extraordinary researches and I was very fortunate to work with them. Thank you so much Yves and Bill.

I would like to thank other members of my thesis committee: Prof. M. Nafi Toksöz, Prof. J. Brian Evans (also second general exam project advisor) and Dr. Hugues Djikpesse for their valuable questions, suggestions and advices.

I would also like to thank Prof. F. Dale Morgan, Prof. Laurent Demanet, Prof. Robert van der Hilst, Prof. Thomas Herring, Prof. Daniel Rothman, Prof. Stephane Rondenay, Prof. Ruben Juanes, Prof. Bradford Hager, Prof. Taylor Perron, Prof. Samuel Bowring, Prof. German Prieto, Prof. Olafur Gudmundsson, Prof. Ari Tryggvason, Prof. Boris Gurevich, Prof. Jie Zang, and Prof. Anton Ziolkowski for their classes, field and summer trips, inspiration and helpful discussions.

I would like to thank Total S.A., ConocoPhillips and the founding members of

Earth Resources Laboratory (ERL) for their financial support during all these years.

I would like thank all my friends and colleagues at MIT for their help and encouragement in my life and study. Particularly, I would like to acknowledge: Sudhish K. Bakku, Xinding Fang, Yingcai Zheng, Xuefeng Shang, Chunquan Yu, S. Ahmad Zamanian, Yuval Tal, Yang Zhang, Yulia Agramakova, Diego Concha, Di Yang, Gabi Melo Silva, Lucas (Bram) Willemsen, Alan Richardson, Abdulaziz Al-Muhaidib, Junlun Li, Hui Huang, Nasruddin Nazerali, Fuxian Song, Alejandra Quintanilla, Mirna Slim, Hussam Busfar, Bongani Mashele, Fred Pearce, Sami Alsaadan, Scott Burdick, Xin Zhang, Tim Sayer, Noa Bechor Ben-Dov, Stephen Brown, Martina Coccia, Beatrice Parker, Clarion Hess, Piero Poli, Thomas Gallot, Dan Burns, Luis Cueto-Felgueroso, Oleg Poliannikov, Bill Durham, Ulrich Mok, Anna Shaughnessy, Susan Turbak, Natalie Counts, Tianrun Chen, Greg Ely, Jared Atkinson, Chen Gu, Jing Liu, Haoyue Wang, Manuel Torres, Eva Golos, Dylan Mikesell, Aurelien Mordret, Douglas Miller, Zhulin Yu, Hua Wang, Russell Hewett, Vincent Jugnon, Hyoungsu Baek, Peter Kang, Yunyue (Elita) Li, Pierre Gouedard, Haijiang Zhang, Berenice Froment, Elizabeth Day, Nathaniel Dixson, Saleh Al Nasser, Leonardo Zepada, Bing Ju, Josimar Alvez da Silva, Kevin Chao, Farrokh Sheibani, Saied Mighani and others.

Last, and certainly not the least, I would like to thank my family: my parents for their love and encouragement; my wife Anastasia, who made all this journey with me, for her special support and patience and for giving birth to our daughter Bella Eden; my brother Leon and his family, and my mother- and sister-in-law Olga and Yulia for their help during all these years.

Contents

---

[1] Shabelansky, A.H., Malcolm, A.E., and Fehler, M.C., (submitted), Geophysics

---

[2] Shabelansky, A.H., Malcolm, A.E., Fehler, M.C., and Rodi, W.L., SEG 84th Annual Meeting, Denver 2014

[3] Shabelansky, A.H., Malcolm, A.E., Fehler, M.C., Shang, X. and Rodi, W.L., 2015, Geophysical Journal International

---

[4] Shabelansky, A.H., Fehler, M.C., and Malcolm, A.E., AGU 46th Fall Meeting, San Francisco 2013.

List of Figures

Chapter 1

Introduction

1.1 Thesis structure

This work is composed of four major components which we present in the following sequence: first, amplitude-balancing source-independent seismic imaging conditions and their relationship with reflection, transmission and conversion coefficients using a concept of conversion ratio coefficients; second, source-independent migration-based seismic trace interpolation of sparse micro-seismic data; third, source-independent migration velocity analysis for updating elastic wave speed models; and fourth, the application of the developed source independent seismic imaging methods to micro-seismic field data obtained from monitoring of Hengill geothermal (volcanic) area in southwest Iceland.

1.2 Motivation and challenges

This thesis has been motivated by the three component broadband micro-seismic data from monitoring abundant natural and induced seismic activity of the Hengill geothermal (volcanic) area in southwest Iceland. My initial research goal has been to investigate the subsurface structure of the Hengill area using full waveform seismic imaging methods from exploration geophysics. However, when I started my research, I faced several challenges in achieving this goal. First, the recording stations were sparsely distributed on the surface with spacing of about 4 km. Second, earthquake/source information for location, origin time, and moment magnitude that I obtained from the Icelandic Meteorological Office for Earthquakes contained a large source of uncertainty because it was estimated using a simplified 1D wave speed models. Third, although I received 3D wave speed models for the Hengill area with more spatial details from my colleagues, Olafur Gudmundsson and Ari Tryggvason from Uppsala University in Sweden, these models were very sparse; on the order of the station spacing, and provided poor spatial resolution for seismic imaging. Questioning myself on how I could improve the wave speed models without having accurate source information, and vice versa, in both cases with sparse seismic data, made me to refocus my research goals by searching for an answer to a more general question: how can I estimate wave speed models and interpolate sparse seismic data, both without having and using source information? In my opinion, this question is of a great importance in both earthquake and exploration seismic communities.

1.3 Why new seismic imaging and velocity analysis approach are important?

In general, standard wave equation seismic imaging and velocity analysis methods all require at least source location information. This information is used either for forward propagation of point source wave fields for wave-type applications such as reverse-time migration (RTM) (Baysal et al., 1983; Chang & McMechan, 1986, 1994) or/and full waveform inversion (FWI) (Tarantola, 1984, 1986; Pratt, 1999; Virieux & Operto, 2009), for ray-tracing for travel time tomography (e.g., Bording et al., 1987; Farra & Madariaga, 1988) or for the projection of seismic data along isochrones for Kirchhoff type imaging (Schneider, 1978; Beylkin, 1985; Bleistein et al., 1987; Bleistein, 1987), where an isochrone is defined by the source-receiver geometry. However, source information is in general not an explicit part of seismic data. Thus, seismic imaging and velocity analysis methods that rely on source information have increased uncertainty because of this assumption in both active and passive seismic source applications.

The principal question this thesis addresses is how to construct seismic images or update wave speed models using a full waveform seismic signal without having any information about its source (e.g., location, mechanism, radiation pattern, rise time, amount of seismic energy release). To answer this question in this thesis we follow a general reasoning that any active or passive seismic signal from surface, VSP, micro-seismic or tele-seismic acquisition satisfies the equations of elastic wave propagation, and all types of waves including reflected, transmitted, and converted-phases generated due to heterogeneous media are recorded by the seismometers. Thus, the seismic signal can be propagated forward and backward in time using an elastic wave simulator and the longitudinal (P) and shear (S) body waves can be separated into independent components. We use the interference between the pure P- and converted-phase S- (or/and pure S- and converted-phase P-) waves to form an image, where the pure waves are responsible for generating the converted-phase waves through interactions with medium heterogeneities. To illustrate this P- and S-wave interference, I show in Figure 1-1 snapshots of the elastic wavefields generated from a single vertical point force source at the surface, at the location marked with a red asterisk. The Z- and X-components of the wavefield $\underline{u} = (u_x, u_z)$ and decomposed P- and S-wave components at a fixed time are shown in the left and right columns respectively in Figure 1-1. The P- and S-wave decomposition is obtained by calculating $\nabla\nabla \cdot \underline{u}$ and $-\nabla \times \nabla \times \underline{u}$, respectively. The interference between the pure (i.e., P, S, PP and SS) and converted-phase (i.e., PS and SP) waves, shown in Figure 1-1 for forward propagation, occurs when the converted-phase wave is split from the pure wave mode. This happens when the wave encounters a change in the subsurface medium parameters (e.g., wave speed or density). The goal of this work is to image the locations at which these conversions take place. This is done by applying an imaging condition, such as zero-lag in time cross-correlation or deconvolution. Since wave propagation is reversible in time, we can locate the position where these conversions occur by propagating a recorded seismic signal backward in time with the correct P- and S-wave speed models. This is the main assumption behind this thesis, and it raises several questions. First, what is the best imaging condition to apply between the interfering P- and S-wavefields? Second, how do we ensure that the wave speed models are correct so that the wavefields propagate accurately backward in time? In other words, how accurately can we estimate the wave speed models without having source information? Third, a more practical question is how to remove spatial artifacts that might be caused by a sparse station distribution such as is often used for micro-seismic or other type of seismic monitoring? All of these questions are addressed in this thesis.

1.4 Thesis chapters summary

I now summarize the main chapters of the thesis.

In chapter 2, I present cross-correlational and de-convolutional source-independent converted-phase (SICP) imaging conditions (ICs) and show the relationship between them using a concept of conversion ratio coefficients, a concept that I introduce through reflection, transmission and conversion coefficients. Tests of imaging conditions with the synthetic Marmousi model and field micro-seismic data highlight the effect of amplitude-balancing in the constructed images.

In chapter 3, I present a source-independent method that alleviates the imaging artifacts caused by the often very sparse surface receiver deployments used for micro-seismic monitoring. The method is based on converted-phase elastic seismic migration and de-migration. We show that despite the spatial aliasing of the recorded data, we are able to suppress the receiver-side migration-operator aliasing artifacts and reconstruct the shallow part of the image. The merit of this approach is that it is elastic, fully data-driven, and does not suffer from migration operator source aliasing, even when a small number of shots or micro-seismic events is used. I present a derivation of the method and test it with a synthetic model and a field data set from the Hengill geothermal reservoir that has abundant natural and induced seismicity.

In chapter 4, I present an approach for source-independent converted-phase elastic wave equation migration velocity analysis (SICP-WEMVA) that is based on the

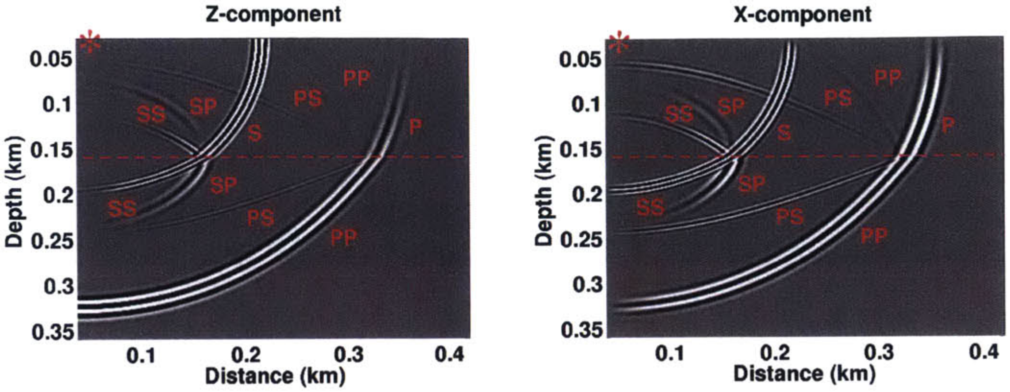

(a) Z-component

(b) X-component

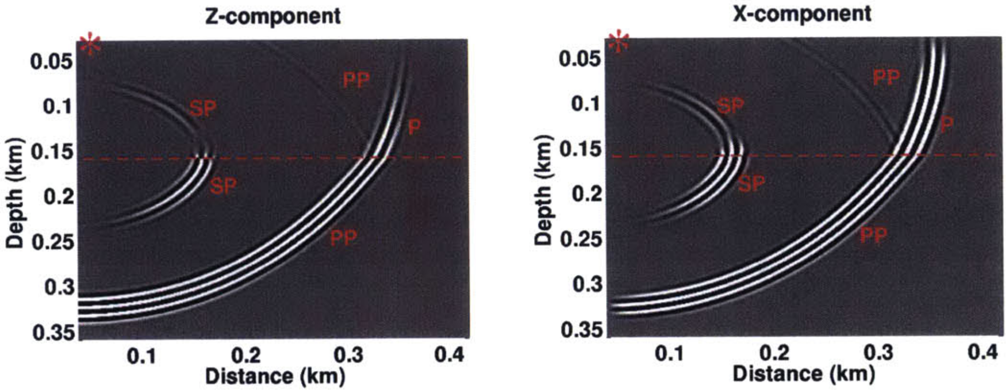

(c) Z-component of P-wavefield

(d) X-component of P-wavefield

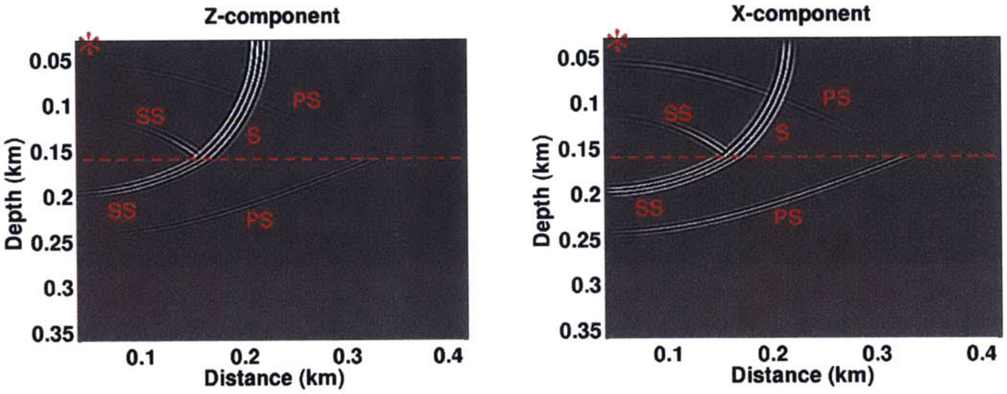

(e) Z-component of S-wavefield

(f) X-component of S-wavefield

Figure 1-1: A snapshot of 2D elastic wave propagation through a horizontal layer, marked with dashed red line. The source is a vertical point force at the surface; its location is marked with the red asterisk. (a) Z- and (b) X-components of the displacement wavefield. (c) Z- and (d) X-components of the decomposed P-wavefield. (e) Z- and (f) X-components of the decomposed S-wavefield. The wave phases are marked in red.

extended space-lag domain SICP imaging condition, and is formulated as an optimization problem with a differential semblance criterion objective function for the simultaneous update of both P- and S-wave velocity models. The merit of this approach is that it is fully data-driven, uses full waveform information, and requires only one elastic backward propagation to form an image rather than the two (one forward and one backward) propagations needed for standard RTM. Moreover, as the method does not require forward propagation, it does not suffer from migration operator source aliasing when a small number of shots is used. I present a derivation of the method and test it with a synthetic model and field micro-seismic data from Hengill.

In chapter 5, I use the source-independent converted-phase reverse time migration methodology developed in previous chapters to construct 2D and 3D images of the Hengill geothermal area in Iceland. Although the sparse station distribution on the surface produces aliased images at shallow depths, the deeper parts are well imaged. The application of the method to seismic data produces images that are well correlated with previous seismic and resistivity studies. In particular, the amplitudes of the images have good correlation with the low resistivity region of the geothermal area. The reason for this correlation is not fully understood, but may provide an additional tool for understanding the Hengill region.

In Appendix A, I review the scheme for numerical solution of the isotropic elastic wave equation calculated as a second order in time staggered grid pseudo-spectral method with Perfectly Matched Layers (PML) absorbing boundary conditions that is used for all my simulations of the elastic seismic waves, presented in this thesis.

In Appendix B, I present the mathematical foundation for the source-independent converted-phase elastic wave equation migration velocity analysis (SICP-WEMVA).

In Appendix C, I present an analytical sensitivity analysis of the moveout in the extended domain common image gather used for SICP-WEMVA.

1.5 Thesis contribution

The contribution of this thesis can be summarized as follows: (1) I present amplitude-balancing source-independent converted-phase seismic imaging conditions and demonstrate their superiority to more conventional cross-correlational imaging condition, (2) I introduce a concept of conversion ratio coefficients to provide a physical and mathematical foundation for the SICP imaging condition, (3) I develop a scheme for source-independent migration-based seismic trace interpolation to remove the migration artifacts caused by sparse station deployment, (4) I present a source-independent extended space-lag domain imaging condition (ESICP-IC), (5) I derive mathematically the optimization scheme for source independent converted-phase velocity analysis (SICP-WEMVA), (6) I numerically investigate the stability and convergence of SICP-WEMVA with synthetic and field data, (7) I investigate analytically the sensitivity of the moveout used for SICP-WEMVA, (8) I investigate the Hengill geothermal area using the developed source-independent imaging methodology.

Parts of this thesis work can also be found in Shabelansky et al. (2013c, 2014b, 2015b).

1.6 Additional contribution beyond this thesis

In addition to the chapters of the thesis, there are additional studies of my pre-general exam projects that have been published, but are not part of this thesis. In these projects, I present methods and case studies for monitoring a heavy oil reservoir under steam injection, for monitoring the CO_2 sequestration process, a numerical investigation of the effect of seismic source mechanism on (source-dependent) seismic imaging and on experimental investigation of the temperature effect on rock permeability in the presence of two-fluid phases. Here are their short summaries.

Data-Driven Estimation of the Sensitivity of Target-Oriented Time-Lapse Seismic Imaging to Source Geometry

The goal of time-lapse imaging is to identify and characterize regions in which the earth's material properties have changed between surveys. This requires an effective deployment of sources and receivers to monitor the region where changes are anticipated. Because each source adds to the acquisition cost, we should ensure that only those sources that best image the target are collected and used to form an image of the target region. This study presented a data-driven approach that estimates the sensitivity of target-oriented imaging to source geometry. The approach is based on the propagation of the recorded baseline seismic data backward in time through the entire medium and coupling it with the estimated perturbation in the subsurface. We tested this approach using synthetic surface seismic and time-lapse VSP field-data from the SACROC field. These tests showed that the use of the baseline seismic data enhances the robustness of the sensitivity estimate to errors, and can be used to select data that best image a target zone, thus increasing the SNR of the image of the target region and reducing the cost of time-lapse acquisition, processing, and imaging. More details can be found in Shabelansky et al. (2011, 2013b).

Monitoring Viscosity Changes from Time Lapse Seismic Attenuation: Case Study from a Heavy Oil Reservoir

Heating heavy oil reservoirs is a common method for reducing the high viscosity of heavy oil and thus increasing the recovery factor. Monitoring of these viscosity changes in the reservoir is essential for delineating the heated region and controlling production. In this study, we present an approach for estimating viscosity changes in a heavy oil reservoir. The approach consists of three steps: measuring seismic wave attenuation between reflections from above and below the reservoir, constructing time-lapse Q and Q^{-1} factor maps, and interpreting these maps using Kelvin-Voigt and Maxwell viscoelastic models. We used a 4D-relative spectrum method to measure changes in attenuation. The method was tested with synthetic seismic data that are noise-free and data with additive Gaussian noise to show the robustness and the accuracy of the estimates of the Q-factor. The results of the application of the method to a field data set exhibited alignment of high attenuation zones along the steam-injection wells, and indicate that temperature dependent viscosity changes in the heavy oil reservoir can be explained by the Kelvin-Voigt model. More details can be found in Shabelansky et al. (2012a, 2015a).

Seismic imaging of hydraulically-stimulated fractures: A numerical study of the effect of the source mechanism

We presented a numerical study of seismic imaging of hydraulically stimulated fractures using a single source from an adjacent fracturing-process. The source is either a point force generated from the perforation of the casing of the well or a double-couple as is typically observed from the induced microseismicity. We assume that the fracture is sufficiently stimulated to be imaged by reflected seismic energy. We show for a specific monitoring geometry of hydrofracturing that not only different waves (P and S) but also different source mechanisms from the same region form an image of different parts of the target fracture and thus add complementary information. The strategy presented in this work could be used as an additional monitoring tool of the hydrofracturing process. More details can be found in Shabelansky et al. (2012b)

Temperature Influence on Permeability of Sioux Quartzite Containing Mixtures of Water and Carbon Dioxide

This work studies the effect of dissolution/exsolution of CO_2 in water in varying temperatures on the permeability of Sioux quartzite saturated with a H_2O/CO_2 mixture. The oscillating pore pressure method (OPPM) was used to minimize overall fluid motions and was, thus, unlikely to disturb the distributions of the immiscible fluids in the pore space. In thermally treated Sioux quartzite, a low porosity rock predominantly containing fissures, the measurements exhibited a counterintuitive increase in permeability, when CO_2 exsolved. Two possible reasons for this behavior are increases in interfacial tension of CO_2 and water or decreases in the viscosity of the exsolved

CO_2 phase. More details can be found in Shabelansky et al. (2014a).

Chapter 2

Amplitude-Balancing Source-Independent Converted-Phase Seismic Imaging Conditions[1]

2.1 Summary

Source independent converted-phase (SICP) imaging is a powerful tool for studying earth structure. It can be easily applied to both active and passive source data and has enormous advantages in processing and calibration time and cost, compared to source-dependent imaging. In this chapter, we present cross-correlational and de-convolutional forms of a source-independent converted-phase imaging condition (IC) and show the relationship between them using a concept of conversion ratio coefficients, a concept that we introduce through reflection, transmission and conversion coefficients. We test these imaging conditions with the synthetic Marmousi model and field micro-seismic data. The results show significant advantages to deconvolutional ICs for high spatial resolution and amplitude-balancing imaging over

---

[1] Shabelansky, A.H., Malcolm, A.E., and Fehler, M.C., (submitted), Geophysics

the cross-correlational form. This opens up the possibility of source-independent true-amplitude full-wavefield imaging with considerable improvement of quality and resolution.

2.2 Introduction

Seismic imaging of the earth's interior is of a great importance in exploration and global seismology. It produces images of subsurface discontinuities associated with impedance contrasts through reflection, transmission or conversion coefficients of propagating waves. One of the pioneering studies on seismic imaging was presented by Claerbout (1971) in which the concept of imaging condition (IC) was introduced. This concept is based on the fundamental assumption that the acquisition/survey geometry is well known: both source and receiver locations are known and seismic waves can be numerically propagated from these locations. This imaging condition has been extensively investigated for the last five decades with algorithms for post- and pre-stack migrations such as survey sinking migration (e.g., Claerbout, 1982; Popovici, 1996), Kirchhoff type migration (Schneider, 1978; Bleistein, 1987), shot profile migration (Stoffa et al., 1990), and reverse time migration (Baysal et al., 1983; Chang & McMechan, 1994). However, when source information is not available, seismic images cannot be constructed using Claerbout's approach. An alternative approach is to use interference between different wave types propagated backward in time from receiver locations only (e.g., Xiao & Leaney, 2010; Brytic et al., 2012; Shang et al., 2012; Shabelansky et al., 2013a, 2014b). We call this imaging condition Source-Independent Converted-Phase Imaging Condition (SICP-IC). In this chapter, we discuss the physical meaning of the SICP-IC and present an amplitude-balancing approach. The chapter is divided into three parts. In the first part, we review the relationship between both the Claerbout (1971) and SICP imaging conditions with reflection, transmission and conversion coefficients. In the second part we introduce the concept of conversion ratio coefficients and show how to associate them with different forms of SICP-IC. In the third part, we present numerical tests of different forms of SICP-IC applied to the synthetic Marmousi model and a micro-seismic field data from geothermal area.

2.3 Relationship between imaging conditions and reflection, transmission and conversion coefficients

In this section, we present multiple forms of a Source-Independent Converted-Phase Imaging Condition (SICP-IC) following the approach of Claerbout (1971) for standard imaging condition.

2.3.1 Standard imaging condition

The relationship between the reflection (or reflection-conversion) coefficients, R, associated with impedance contrasts (see Figure 2-1(a)), is defined as the ratio between the reflected (or reflected-converted) and the incident wavefields

$$R_{pp} = \frac{u_{pp}^{refl}}{u_p^{inc}}, \qquad R_{ps} = \frac{u_{ps}^{refl}}{u_p^{inc}}, \tag{2.1}$$

and for the transmission (or transmission-conversion) coefficients T as the ratio between the transmitted (or transmitted-converted) and the incident wavefields

$$T_{pp} = \frac{u_{pp}^{tran}}{u_p^{inc}}, \qquad T_{ps} = \frac{u_{ps}^{tran}}{u_p^{inc}}. \tag{2.2}$$

For the sake of simplicity we omit the vector notation of the wavefield u (e.g., displacement, particle-velocity or acceleration) as well as the spatial and time indices. The superscripts inc, $refl$, and $tran$ refer to incident, reflected and transmitted waves, and their subscripts p and s denote the wave type, P and/or S. Note that we denote u_{ps}^{refl} and u_{ps}^{tran} as reflected-converted and transmitted-converted from p to s, respectively.

The imaging condition in Claerbout (1971) attempts to mimic R_{pp}, where the incident wavefield is calculated by forward propagation from the source and often is called the source wavefield, and the reflected (or reflected-converted) wavefield is calculated by back-propagation in time from the receivers and is called the receiver wavefield. Note that the wavefield in the denominator of equations 2.1 and 2.2 can be zero. Many studies have investigated how to avoid the division by zero and suggest different solutions (e.g., Valenciano et al., 2003; Kaelin et al., 2006; Schleicher et al., 2008; Chattopadhyay & McMechan, 2008). One of the solutions is to multiply both the numerator and denominator by the denominator and add a small number to the denominator (Valenciano et al., 2003). Thus for equation 2.1 we obtain

$$I_{pp}^{decon} = \frac{u_{pp}^{refl} u_{p}^{inc}}{(u_{p}^{inc})^2 + \epsilon^2}, \tag{2.3}$$

where I is the calculated image and ϵ^2 is a small number. This form is called a de-convolutional imaging condition, denoted with the superscript *decon*. This imaging condition depends strongly on the choice of the ϵ^2, which changes for different data sets, and may still be unstable. As an alternative to the de-convolutional imaging condition, Claerbout (1971) introduced the cross-correlational imaging condition by taking only the numerator of equation 2.3 giving

$$I_{pp}^{cross} = u_{pp}^{refl} u_{p}^{inc}, \tag{2.4}$$

where the superscript *cross* refers to cross-correlation. Figure 2-1(b) shows schematically the application of the concept of the imaging condition between forward-propagating (incident) P and backward propagating (reflected) P wavefields, and Figure 2-1(c) between forward-propagating (incident) P and and backward propagating (reflected-converted) S wavefields. Note that with Claerbout (1971) imaging condition we back-propagate only one reflected or reflected-converted wavefield (i.e., either PP or PS) at a time and the other wave type, marked with grey line is not used.

2.3.2 Source independent converted-phase imaging condition

The source independent converted phase imaging condition (SICP-IC) uses both back-propagated wavefields simultaneously (see Figure 2-1(d)) in the cross-correlational form as

$$I^{cross} = u_{pp}^{refl} u_{ps}^{refl}. \tag{2.5}$$

Note that the source location, marked with the star in Figure 2-1(d), is irrelevant for SICP-IC because we use only the reflected and (reflected-) converted-phase wavefields (i.e., the incident wavefield marked with the grey line is not used). Moreover, the source location can be anywhere along the grey lines (see Figure 2-2), which makes SICP-IC applicable to both reflection and transmission (active and passive) seismic data. The sources along these grey lines can in general be outside of the computational grid and the image is constructed only in the vicinity of the receivers (i.e., far from the sources). In addition, the SICP-IC is computationally very efficient because it uses only one elastic wave propagation, backward in time, during which the back-propagated (either displacement or particle velocity) vector wavefield is simultaneously separated into the P and S wavefield components and the image is formed (using SICP-IC) without storing (and subsequently reading) any of the separated wavefields, as is common practice for (both acoustic and elastic) standard reverse-time migration (RTM).

The images produced with SICP-IC depend on the wavefield separation approach. Separation using the Helmholtz decomposition produces images with flipped amplitude polarity that thus require correction before or after the construction of the images (Shang et al., 2012; Shabelansky et al., 2013c). Separation using the vector wavefield decomposition is computationally more expensive, but produces images with consistent amplitude polarity (more details are given in appendix 2.8). Thus,

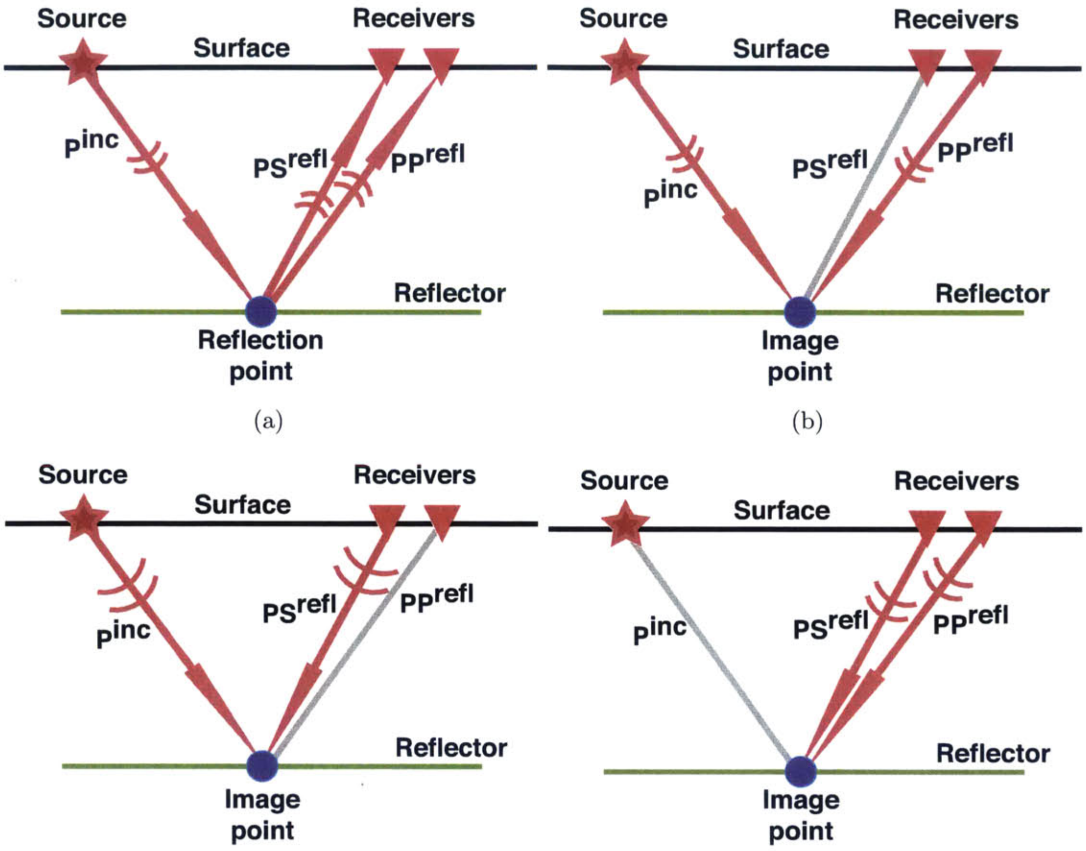

(a) (b) (c) (d)

Figure 2-1: Schematics illustrating (a) elastic wave propagation that samples a point (blue dot) on a reflector with an incident P-wave, (b) imaging of the reflection point using Claerbout's imaging condition (IC) with forward and backward propagating P waves, and with (c) forward propagating P-wave and backward propagating S wave. (d) SICP-IC with both P and S backward propagating waves. The red arrows in (b), (c) and (d) indicate the direction of the propagating waves that form an image. The grey lines mark available wave types that are not used in the image construction. Although source information, marked with a star, indicates the origin of the waves, the image obtained with SICP-IC in (d) uses receiver information only.

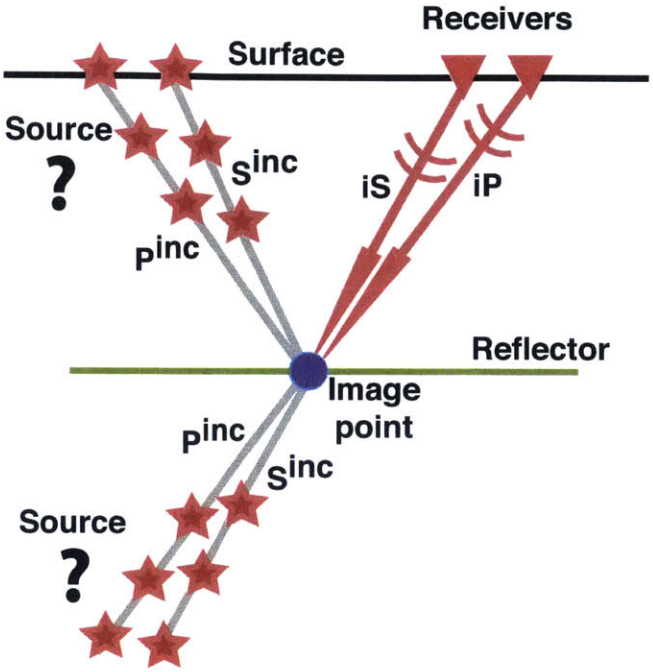

Figure 2-2: A schematic showing generalization of SICP-IC for reflection and transmission seismic data with either (or both) incident P- or/and S-wavefield(s). The red arrows indicate the direction of the propagating waves that form an image. The grey lines mark available wave types that are not used in the image construction. The index i marks an incident wave and can be either P or S. Although source information, marked with stars, indicates the origin of the waves, the image obtained with SICP-IC uses receiver information only.

the separated P- and S-wavefields are

$$\underline{u}_p = \nabla\nabla\cdot\underline{u}, \qquad \underline{u}_s = -\nabla\times\nabla\times\underline{u}, \tag{2.6}$$

where $\underline{u}_p$ and $\underline{u}_s$ are the P- and S-components of the displacement vector wavefield $\underline{u}$. The gradient, divergence and curl operators are ∇, $\nabla\cdot$ and $\nabla\times$, respectively.

As we have shown above, Claerbout's imaging condition is directly related to reflection, transmission and conversion coefficients. However, SICP-IC is instead associated with the relative energy between pure reflected (or transmitted) and the converted-phase reflected (or transmitted) waves. To understand what physical property is imaged using this imaging condition, we define the conversion ratio coefficient, C as the ratio between the reflection or transmission coefficients of the converted and pure wave modes. For an incident P-wave, this gives

$$C_{ps}^{R} := \frac{R_{ps}}{R_{pp}} = \frac{\frac{u_{ps}^{refl}}{u_{p}^{inc}}}{\frac{u_{pp}^{refl}}{u_{p}^{inc}}} = \frac{u_{ps}^{refl}}{u_{pp}^{refl}}, \qquad C_{ps}^{T} := \frac{T_{ps}}{T_{pp}} = \frac{\frac{u_{ps}^{tran}}{u_{p}^{inc}}}{\frac{u_{pp}^{tran}}{u_{p}^{inc}}} = \frac{u_{ps}^{tran}}{u_{pp}^{tran}}, \tag{2.7}$$

and for an incident S-wave we have

$$C_{sp}^{R} := \frac{R_{sp}}{R_{ss}} = \frac{\frac{u_{sp}^{refl}}{u_{s}^{inc}}}{\frac{u_{ss}^{refl}}{u_{s}^{inc}}} = \frac{u_{sp}^{refl}}{u_{ss}^{refl}}, \qquad C_{sp}^{T} := \frac{T_{sp}}{T_{ss}} = \frac{\frac{u_{sp}^{tran}}{u_{s}^{inc}}}{\frac{u_{ss}^{tran}}{u_{s}^{inc}}} = \frac{u_{sp}^{tran}}{u_{ss}^{tran}}, \tag{2.8}$$

where the superscripts T and R denote transmitted and reflected wavefields respectively, and the subscripts refer to the wave type conversion (e.g., ps means from P to S). Note that C is independent of the incident wavefield. It depends however on the angle of incidence, which can be tracked using Snell's law through reflected and reflected-converted (and/or transmitted and transmitted-converted) angles.

From equations 2.7 and 2.8 we define the source-independent converted-phase imaging condition similarly to Claerbout's de-convolution IC as

$$I_{ps}^{R} := \frac{u_{ps}^{refl} u_{pp}^{refl}}{(u_{pp}^{refl})^2 + \epsilon^2}, \tag{2.9}$$

$$I_{ps}^{T}(\underline{x}) := \frac{u_{ps}^{tran} u_{pp}^{tran}}{(u_{pp}^{tran})^2 + \epsilon^2}, \tag{2.10}$$

$$I_{sp}^{R} := \frac{u_{sp}^{refl} u_{ss}^{refl}}{(u_{ss}^{refl})^2 + \epsilon^2}, \tag{2.11}$$

and

$$I_{sp}^{T} := \frac{u_{sp}^{tran} u_{ss}^{tran}}{(u_{ss}^{tran})^2 + \epsilon^2}. \tag{2.12}$$

When we back propagate entire seismic records simultaneously without time windowing different phases, we do not discriminate between reflected, transmitted and converted waves and their mode of incidence. We therefore omit the superscript and the first letter of the subscript of the wavefield u in equations 2.9, 2.10, 2.11 and 2.12 (i.e., we write p instead of pp or sp and s instead of ss or ps). Thus, an explicit form of de-convolutional SICP-IC for N_s sources is

$$I_p^{decon}(\underline{x}) := \sum_j^{N_s} \int_T^0 \frac{\underline{u}_s^j(\underline{x},t) \cdot \underline{u}_p^j(\underline{x},t)}{(\underline{u}_p^j(\underline{x},t))^2 + \epsilon^2} dt, \tag{2.13}$$

and

$$I_s^{decon}(\underline{x}) := \sum_j^{N_s} \int_T^0 \frac{\underline{u}_p^j(\underline{x},t) \cdot \underline{u}_s^j(\underline{x},t)}{(\underline{u}_s^j(\underline{x},t))^2 + \epsilon^2} dt, \tag{2.14}$$

where $\cdot$ is the dot product and the subscript of I denotes the wavefield of the denominator, which is called the illuminating wavefield. The spatial and time coordinates are $\underline{x}$ and t, and the (new) superscript j is the source index. Note that the ICs in equations 2.13 and 2.14 construct images only from the combination between the pure and the converted-phase wave modes (i.e., either pp with ps or ss with sp) as shown in equations 2.9, 2.10, 2.11 and 2.12. This is because the pure (pp and ss) wave modes are separated in time during the back-propagation and their combination should not contribute to image, as well as the combination between ps and sp.

By taking the numerator only, we obtain an explicit cross-correlational SICP-IC form (Shabelansky et al., 2014b):

$$I^{cross}(\underline{x}) = \sum_j^{N_s} \int_T^0 \underline{u}_p^j(\underline{x},t) \cdot \underline{u}_s^j(\underline{x},t) dt, \tag{2.15}$$

Note that the cross-correlational SICP-IC is unconditionally stable. However, because the denominator is omitted, the cross-correlational image is not-amplitude balanced (i.e., not-true amplitude).

To investigate the conversion ratio coefficients and their relationship with SICP-IC, we choose an example for a free-surface reflection and conversion coefficients from Aki & Richards (2002, page 137) with P- and S-wave speeds $V_p = 5$ km/s and

$V_s = 3$ km/s, respectively. We plot these coefficients along with their conversion ratios in Figure 2-3. We observe that when the denominator approaches zero, the ratio trends toward infinity, and when denominator approaches 1, the ratio goes toward coefficient of the numerator. We also calculate the reflection, transmission and conversion coefficients for a two half-space model to test how the conversion ratio coefficients are correlated with the reflection, transmission and conversion coefficients (Figures 2-4 and 2-5). We use the same V_p and V_s having $\Delta V_p = 0.5$ km/s and $\Delta V_s = 0.2$ km/s. We observe in Figure 2-4 that the conversion ratio is completely uncorrelated with the reflection or reflection-conversion coefficients because neither of them is around 1. For the transmission case (Figure 2-5) when the pure transmitted mode (i.e., PP or SS) is generally 1, the conversion ratio has good correlation with the transmission-conversion coefficients.

The conversion ratio coefficients presented in equations 2.7 and 2.8 and their deconvolutional imaging condition forms, equations 2.13 and 2.14 go to infinity when the coefficient or the wavefield of the denominator is zero. This contradicts the idea behind an imaging condition: when one wavefield is zero the image should be zero. Another downside of the imaging condition in equations 2.13 and 2.14 is that only one wavefield is used for normalization/illumination (either P- or S-wave but not both). To alleviate these two limitations, we propose normalized conversion ratio coefficients that will be set to zero when one of the waves is zero and will be between -1 and 1: the values of ±1 are when both wavefields are equal in amplitude with the same or different sign. The normalized conversion ratio coefficients are given as

$$M_p^R = \frac{4R_{pp}R_{ps}}{(|R_{pp}| + |R_{ps}|)^2} = \frac{4u_{pp}^{refl}u_{ps}^{refl}}{(u_{pp}^{refl})^2 + 2|u_{pp}^{refl}u_{ps}^{refl}| + (u_{ps}^{refl})^2}, \tag{2.16}$$

$$M_p^T = \frac{4T_{pp}T_{ps}}{(|T_{pp}| + |T_{ps}|)^2} = \frac{4u_{pp}^{tran}u_{ps}^{tran}}{(u_{pp}^{tran})^2 + 2|u_{pp}^{tran}u_{ps}^{tran}| + (u_{ps}^{tran})^2}, \tag{2.17}$$

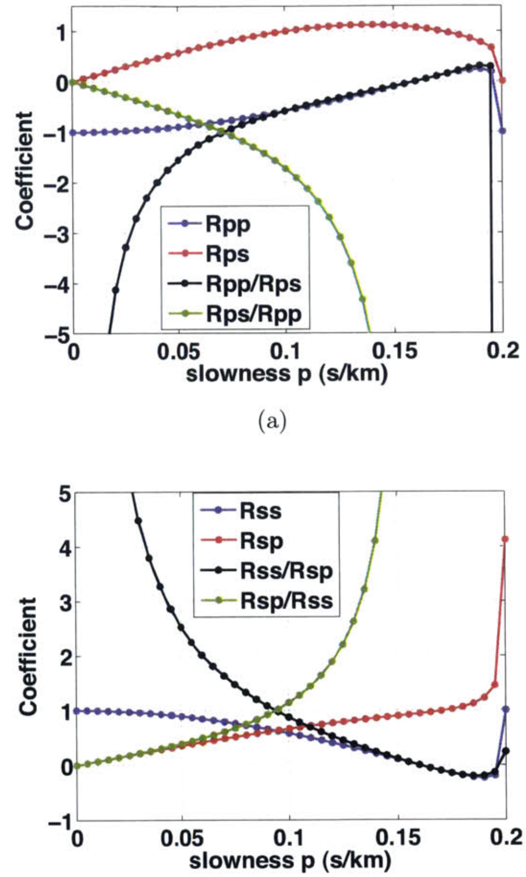

(a)

(b)

Figure 2-3: P-SV reflection, conversion and their conversion ratio coefficients (for displacements) for a free-surface shown against horizontal slowness, $p = sin(\theta)/V_p = \sin(\phi)/V_s$ where θ and ϕ are P- and S-wave incident angles, $V_p = 5$ km/s and $V_s = 3$ km/s. For (a) P incident wave and (b) S incident wave. The conversion ratio is not defined (i.e., infinity) when the denominator is zero.

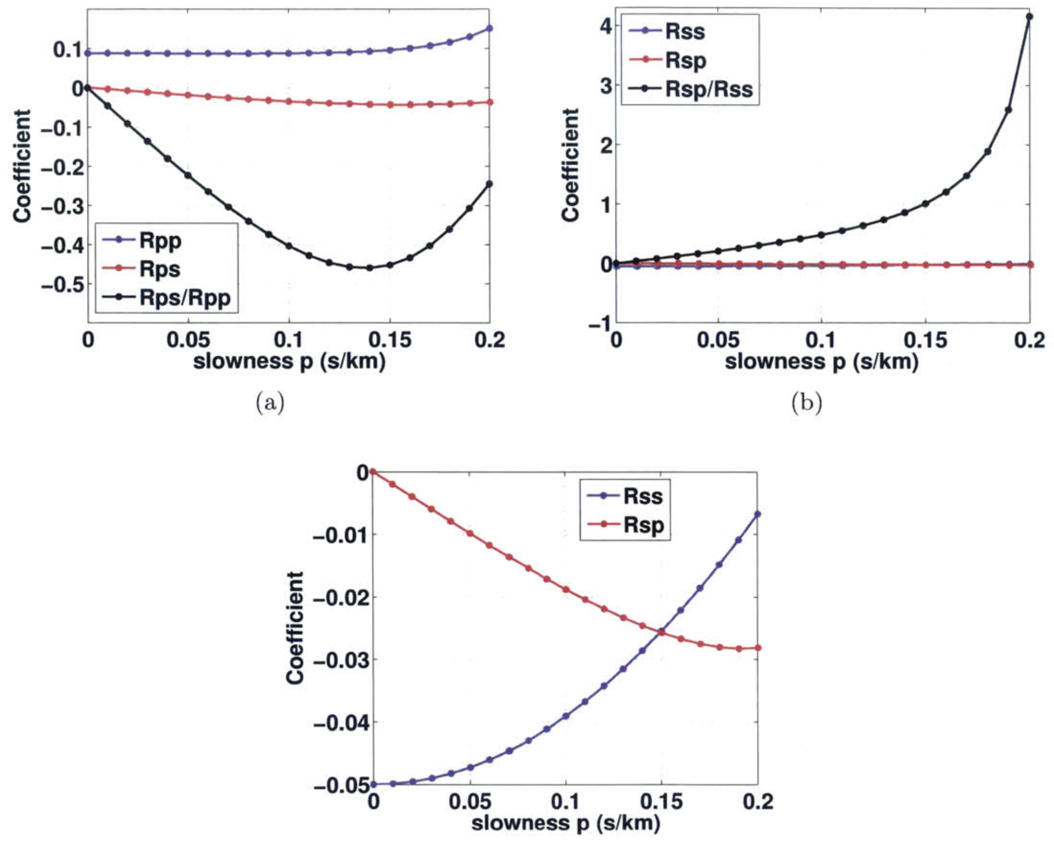

(a) (b)

(c)

Figure 2-4: P-SV reflection, reflection-conversion and their conversion ratio coefficients (for displacements) for a half-space model shown against horizontal slowness, $p = sin(\theta)/V_p = \sin(\phi)/V_s$ where θ and ϕ are P- and S-wave incident angles, $V_p =$ 5 km/s, $V_s = 3$ km/s, $\Delta V_p = 0.5$ km/s, and $\Delta V_s = 0.2$ km/s. For (a) P incident wave and (b) S incident wave. (c) is the zoom in of (b) for R_{ss} and R_{sp}. Note that the conversion ratios are not correlated with the reflection and reflection-conversion coefficients.

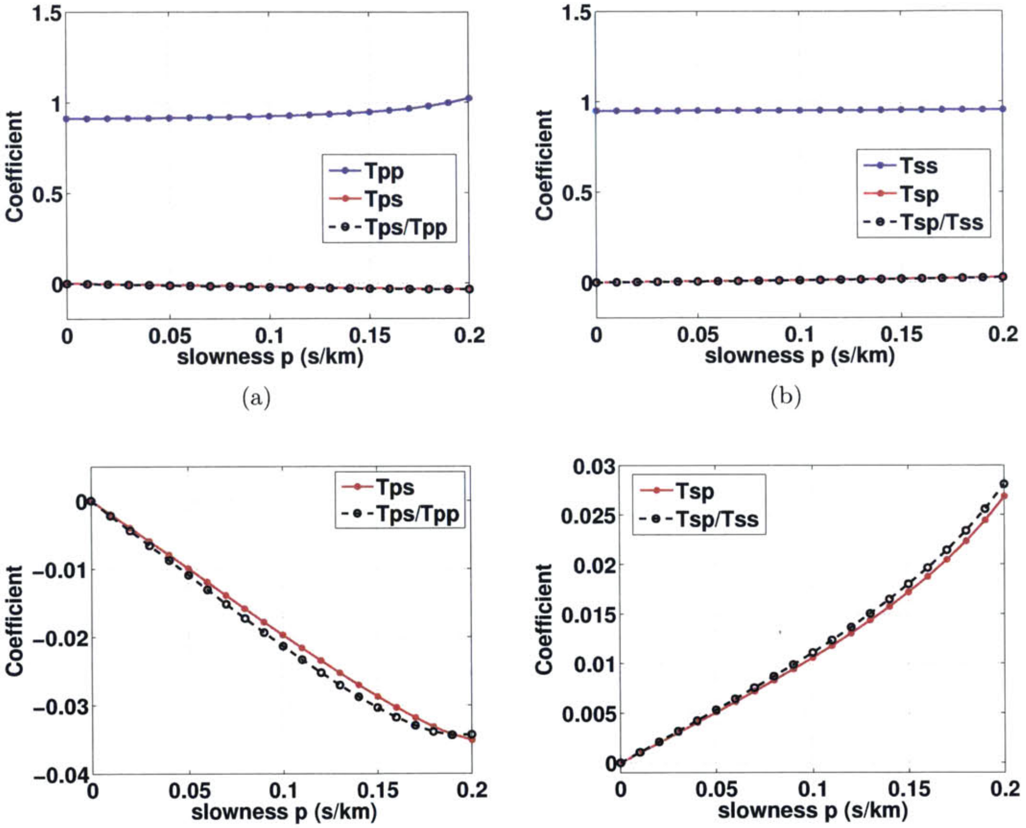

(a) (b)

(c) (d)

Figure 2-5: P-SV transmission, transmission-conversion and their conversion ratio coefficients (for displacements) for a half-space model shown in Figure 2-4 for (a) P incident wave and (b) S incident wave. (c) and (d) are the zoom in of their respective coefficients in (a) and (b). Note that the conversion ratios are correlated with the transmission-conversion coefficients, T_{ps} and T_{sp}.

$$M_s^R = \frac{4R_{ss}R_{sp}}{(|R_{ss}| + |R_{sp}|)^2} = \frac{4u_{ss}^{refl}u_{sp}^{refl}}{(u_{ss}^{refl})^2 + 2|u_{ss}^{refl}u_{sp}^{refl}| + (u_{sp}^{refl})^2}, \tag{2.18}$$

and

$$M_s^T = \frac{4T_{ss}T_{sp}}{(|T_{ss}| + |T_{sp}|)^2} = \frac{4u_{ss}^{tran}u_{sp}^{tran}}{(u_{ss}^{tran})^2 + 2|u_{ss}^{tran}u_{sp}^{tran}| + (u_{sp}^{tran})^2}. \tag{2.19}$$

In Figures 2-6 and 2-7, we show the coefficients calculated using equations 2.16, 2.17, 2.18 and 2.19 for the free-surface and half-space examples discussed above. We observe that their behavior is stable.

For imaging purposes, we back-propagate entire seismic records simultaneously without discriminating between reflected and transmitted waves and drop their mode of incidence as in equations 2.13, 2.14 and 2.15. Thus, the explicit form for the normalized SICP-IC is:

$$I^M(\underline{x}) := \sum_j^{N_s} \int_T^0 \frac{4\underline{u}_p^j(\underline{x},t) \cdot \underline{u}_s^j(\underline{x},t)}{(\underline{u}_p^j(\underline{x},t))^2 + 2|\underline{u}_p^j(\underline{x},t) \cdot \underline{u}_s^j(\underline{x},t)| + (\underline{u}_s^j(\underline{x},t))^2 + \epsilon^2} dt, \tag{2.20}$$

where we have also added a stabilization factor, ϵ^2, to the denominator as in equations 2.13 and 2.14. In the next sections we will investigate numerically each SICP-IC presented here, and highlight the advantages of the normalized SICP-IC.

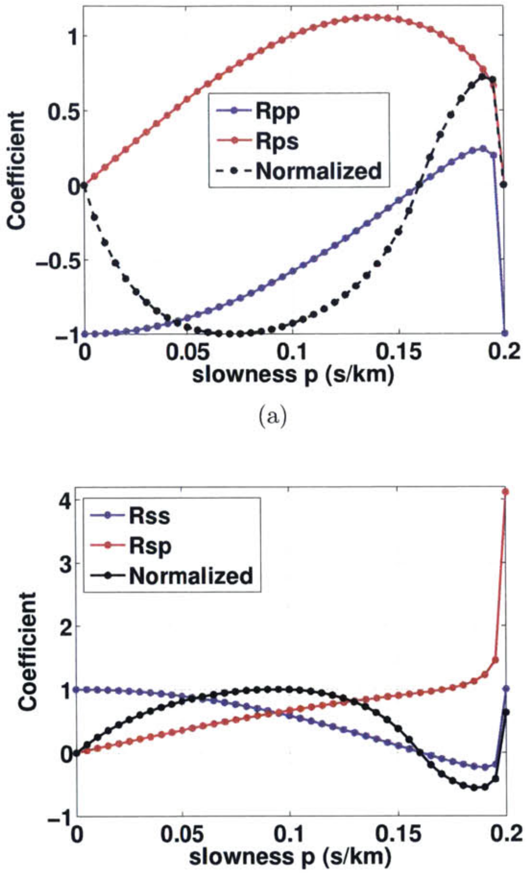

(a)

(b)

Figure 2-6: Normalized conversion ratio coefficients for the free surface example shown in Figure 2-3.

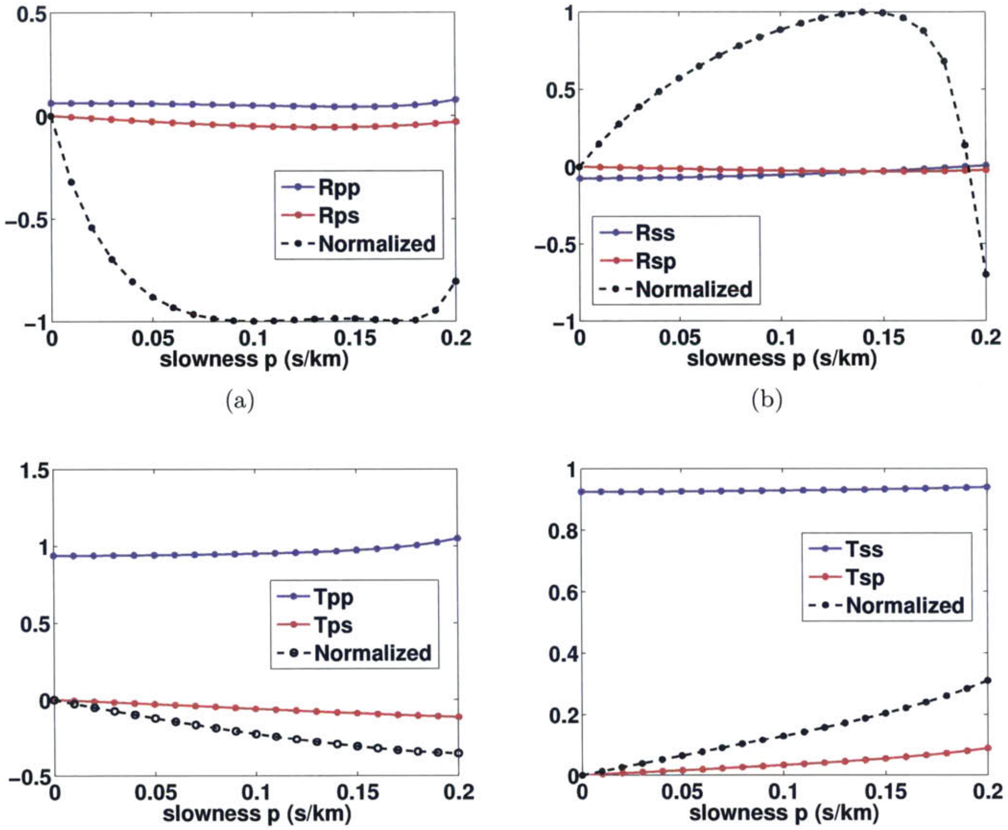

(a) (b)

(c) (d)

Figure 2-7: Normalized conversion ratio coefficients for the half-space example shown in Figures 2-4 and 2-5.

2.4 Numerical tests

To examine the stability and illustrate advantages of different forms of the imaging conditions given in equations 2.13, 2.14, 2.15 and 2.20, we test them with the Marmousi synthetic model and field data from passive source micro-seismic monitoring of a geothermal area in Iceland. All elastic wave solutions for imaging are modeled with a 2D finite-difference solver, using a second order in time staggered-grid pseudo-spectral method with perfectly matched layer (PML) absorbing boundary conditions (details are shown in appendix A).

2.4.1 Marmousi model

We use the P-wave speed model, shown in Figure 2-8(a) with constant density of 2500 kg/m^3, and V$_p$/V$_s$ of 2. The number of grid points in the models is $N_z = 150$ and $N_x = 287$, and the spatial increments are $\Delta x = \Delta z = 12$ m. In Figure 2-8(b) we show a model of discontinuities for Marmousi that we use as a perfect reference for the imaging results: this model was produced from the difference between the original squared P-wave slowness (Figure 2-8(a)) and a spatially smoothed squared P-wave slowness. We model two sets of sources; each consists of 27 sources with vertical point force mechanism, equally distributed horizontally with 120 m spacing at one of two depths: one at the surface, 0 km, and one at a depth of 1.7 km. The reason for choosing source sets at two depths is to test both transmission-like and reflection-like acquisition geometries. We use a Ricker wavelet with a peak frequency of 30 Hz and time step of 0.0005 s. The seismic data are recorded with two-component receivers that are equally distributed and span the same computational grid at the surface. In Figure 2-9 we show imaging results produced with sources on the surface and the four imaging conditions given in equations 2.13, 2.14, 2.15 and 2.20. Note that we have applied no vertical gain nor compensation for geometric spreading, in contrast to common practice (e.g., Claerbout, 1982, page 235), in order to highlight the differences between different imaging conditions. Figure 2-9(a), obtained with the de-convolutional SICP-IC with P-wave illumination (equation 2.13), illustrates good amplitude balancing with depth, although it amplifies the shallow part, particularly the top right between 0 and 0.4 km in depth and 2 and 3 km in horizontal distance. The result in Figure 2-9(b), obtained with the de-convolutional SICP-IC with S-wave illumination (equation 2.14), is the most similar to the model of discontinuities (perfect reference shown in Figure 2-8(b)) and illustrates higher resolution because of the short S-wavelengths. However, it suffers from noise, caused by instabilities in the imaging condition. Figure 2-9(c), obtained with equation 2.15, clearly shows that the amplitudes are attenuated with depth. The image in Figure 2-9(d) produced by equation 2.20 is similar to Figure 2-9(a). However, the amplitudes in Figure 2-9(d) are considerably better balanced and have better spatial resolution with depth using both P- and S-illuminating wavefields, compared with those in Figures 2-9(a), 2-9(b) and 2-9(c) (see particularly the shallow region between 0 and 0.4 km in depth, and the deep region of anticlines).

To enhance the spatial resolution of the images shown in Figure 2-9, we apply a Laplacian filter (see Figure 2-10). We observe the same conclusions as those obtained for Figure 2-9. Nevertheless, the images in Figure 2-10 are more similar to the reference model than those in Figure 2-9. Again the image with normalized illumination by both P- and S-wavefields (in Figure 2-10(d)) has the most balanced amplitudes compared with these in Figures 2-10(a), 2-10(b) and 2-10(c).

In Figures 2-11 and 2-12 we present images generated with sources at a depth of 1.7 km. We observe again that the image obtained with the cross-correlational SICP-IC has poorer amplitude recovery compared with those produced with the de-convolutional SICP-ICs. Also the images with the normalized illumination, Figures 2-11(d) and 2-12(d), have amplitude balancing most similar to that of the perfect reference model.

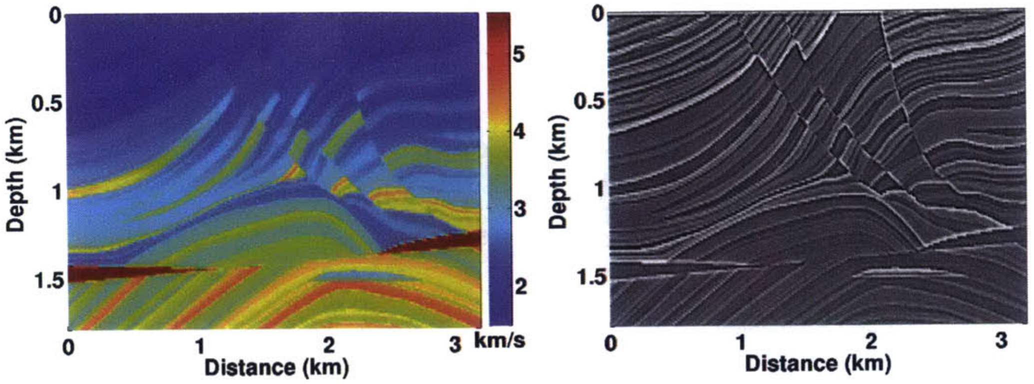

(a) (b)

Figure 2-8: (a) Marmousi P-wave velocity model, (b) Model of discontinuities produced by taking the differnce between the original slowness squared of (a) and its smoothed squared model.

2.4.2 Field micro-seismic data from the Hengill geothermal area, Iceland

The second example uses passive source, micro-seismic field data from a geothermal area in Iceland that has abundant natural and induced seismicity (see Figure 2-13(a)). We test SICP-ICs with four stations (SAN, IND, BIT and TRH) along a 2D line at a latitude of 64.06° and longitude ranging between -21.6° and -21.10°. In Figures 2-13(b) and 2-13(c), we show four representative traces sorted into a common shot gather (Z-component) from a single earthquake. Each trace is of a time record of $T = 12$ s and $\Delta t = 0.005$ s, and is band-pass filtered between 2 and 12 Hz. The relative position of the traces in the common shot gather corresponds to the relative locations of the stations at the surface, $\underline{x}_{obs} = (x, z_{surface} = 0 \text{ km})$. The computational grid is $N_z = 90$ and $N_x = 300$ and the spatial increments are $\Delta z = 0.2$ km and $\Delta x = 0.15$ km. To construct an image of the geothermal area that is located between longitudes -21.4° and -21.2°, we use 17 earthquakes of moment magnitude between 0.9 and 1.2. Initial P- and S-wave speeds were taken from the model of Tryggvason et al. (2002), obtained using regional-scale travel-time tomography. By applying the different forms of SICP-IC, given respectively in equations 2.13, 2.14, 2.15 and

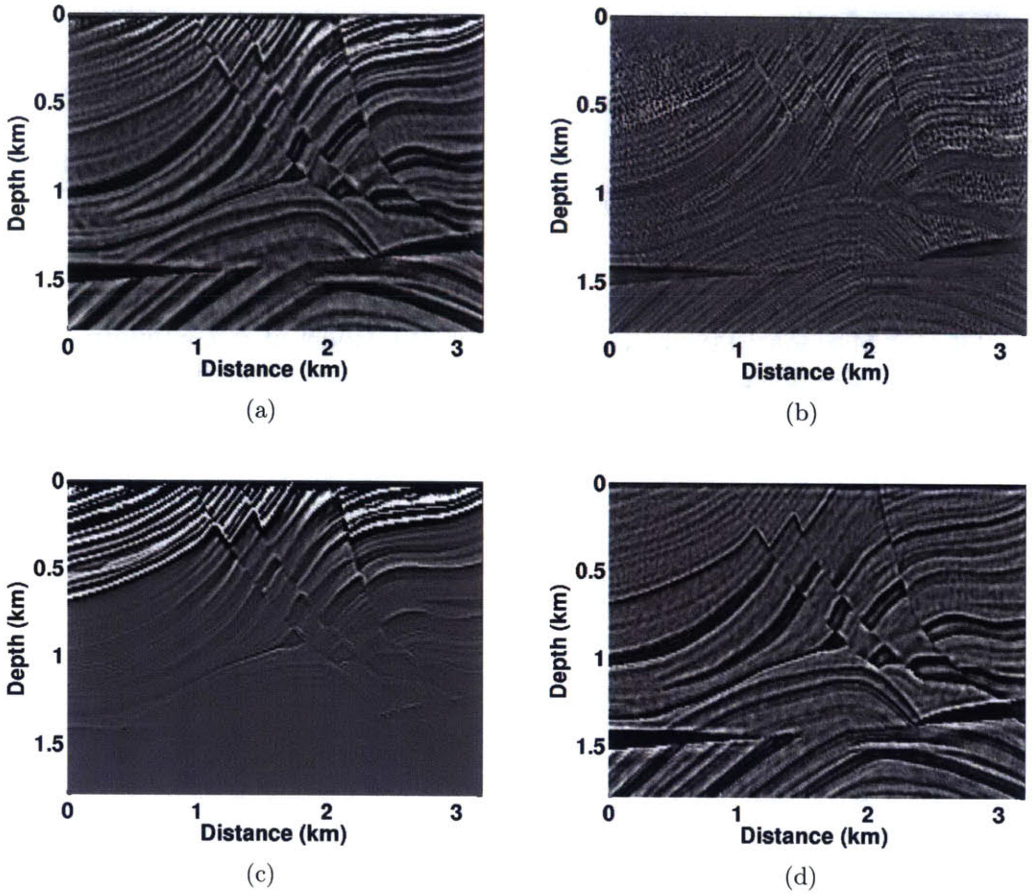

(a) (b) (c) (d)

Figure 2-9: Migrated images produced with 27 sources with 0.12 km horizontal interval at the surface and receivers at the surface using: (a) de-convolutional SICP-IC with P-wave illumination (equation 2.13), (b) de-convolutional SICP-IC with S-wave illumination (equation 2.14), (c) cross-correlational SICP-IC (equation 2.15) and (d) de-convolutional SICP-IC with normalized illumination (equation 2.20). The source mechanism of each source is a vertical point force and the V_p/V_s is 2. Note that amplitudes in (a) and (c) are attenuated with depth, in (b) the image is noisy, while in (d) the image amplitudes are most balanced, particularly at the shallow depths between 0 and 0.4 km and in the regions containing anticlines, compared to these in (a), (b) and (c).

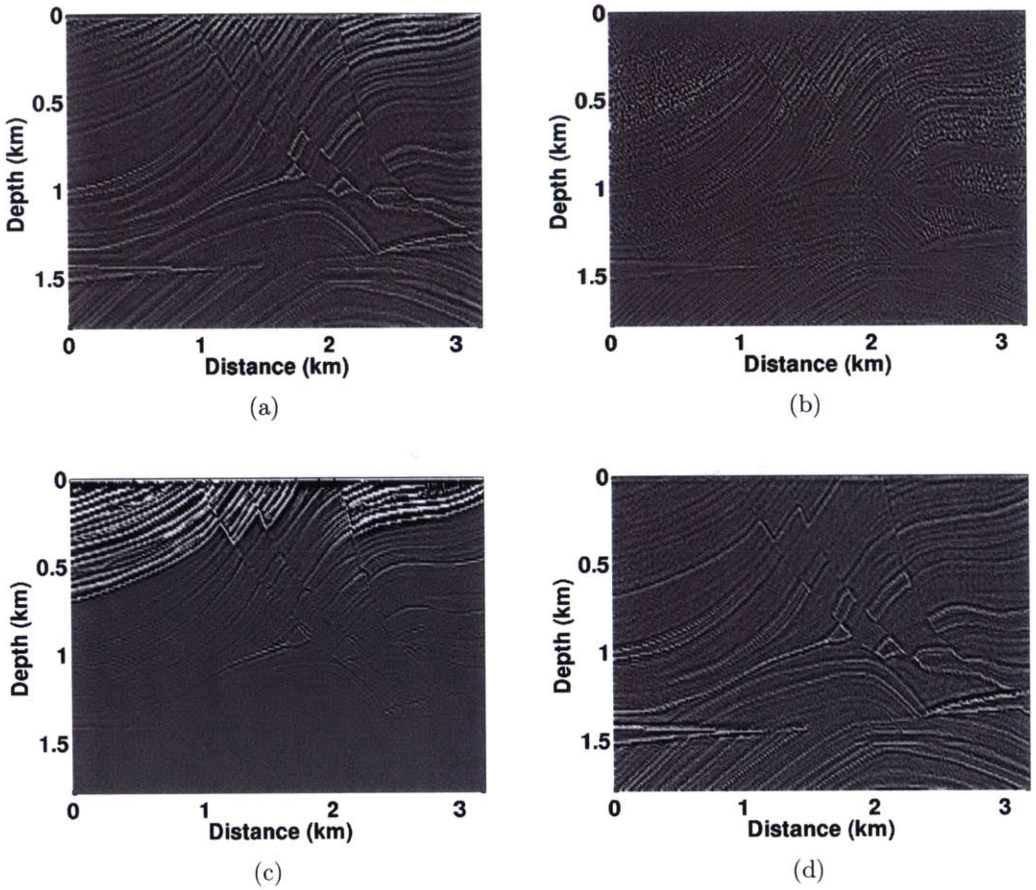

(a) (b)

(c) (d)

Figure 2-10: Migrated images shown in Figure 2-9 after applying the Laplacian filter.

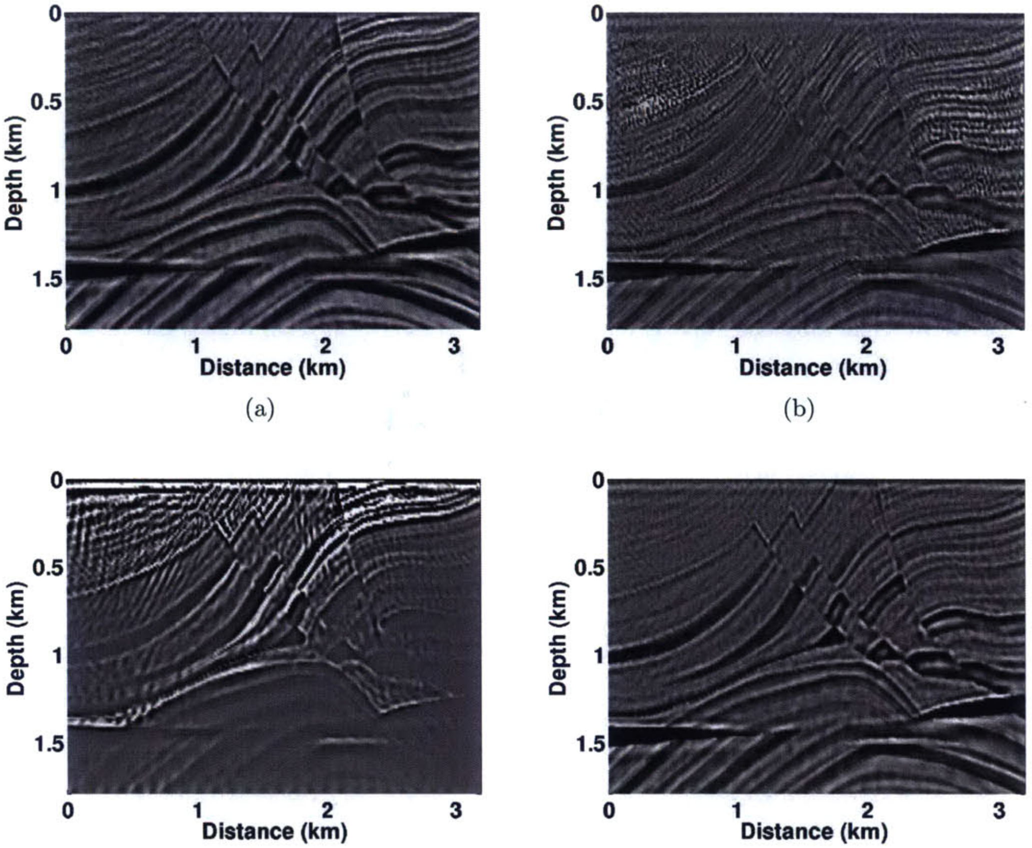

(a) (b)

(c) (d)

Figure 2-11: Migrated images produced with 27 sources with 0.12 km horizontal interval at the surface and receivers at the depth of 1.7 km using: (a) de-convolutional SICP-IC with P-wave illumination (equation 2.13), (b) de-convolutional SICP-IC with S-wave illumination (equation 2.14), (c) cross-correlational SICP-IC (equation 2.15) and (d) de-convolutional SICP-IC with normalized illumination (equation 2.20). The source mechanism of each source is a vertical point force and the V_p/V_s is 2.

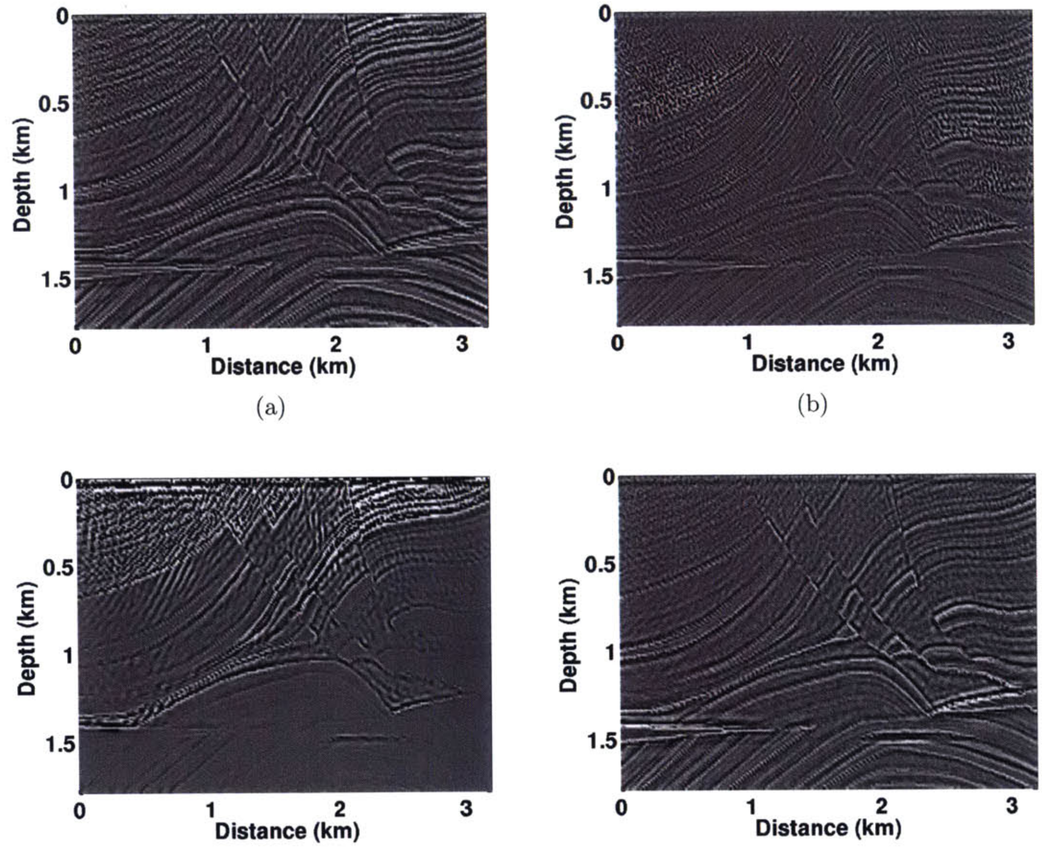

(a) (b)

(c) (d)

Figure 2-12: Migrated images shown in Figure 2-11 after applying the Laplacian filter.

2.20, and followed by a Laplacian filter, we obtain images in Figures 2-14. Note that the shallow part of the images is completely contaminated by aliasing caused by the sparse station distribution on the surface. In these images we observe that SICP-IC with P-wave and normalized illuminations produce images with balanced amplitudes (see particularly depths between 4 and 6.5 km). We also observe that the noise level in the shallow part of Figure 2-14(d) is considerably smaller than that in the other images. These results clearly suggest that different forms of SICP-IC give different amplitude balancing, and illustrate the importance of correctly normalizing the imaging condition.

2.5 Discussion

The examples and results presented in this work illustrate the properties and applicability of the SICP imaging conditions. Namely, we showed three very important properties: first, no source information (e.g., location, mechanism, time-function) was required to form an image; second the image can be constructed only in the vicinity of the receivers (i.e., far from the sources); and third, the image can be constructed during one elastic wave propagation backward in time and no wavefield storage is required to form an image. These properties reduce the computational cost and memory storage, and more importantly improve the image quality in comparison with standard (elastic) RTM. There are still several remaining questions, however. In this section we will address three of the most pressing.

The first question is how to choose seismic data (i.e., shot gathers) from different seismic sources/events such that they produce images from different illuminating angles. For passive-source surveys where we posses no direct source information, polarization analysis of particle motion of three component data (e.g. Vidale, 1986; Jackson et al., 1991) could provide information about the back-azimuth. This information can be used as an approximation to estimate illumination angles. For active-source acquisition, although source information is directly available, approaches of optimal acquisition design could be beneficial (e.g., Maurer et al., 2010; Guest & Curtis, 2011;

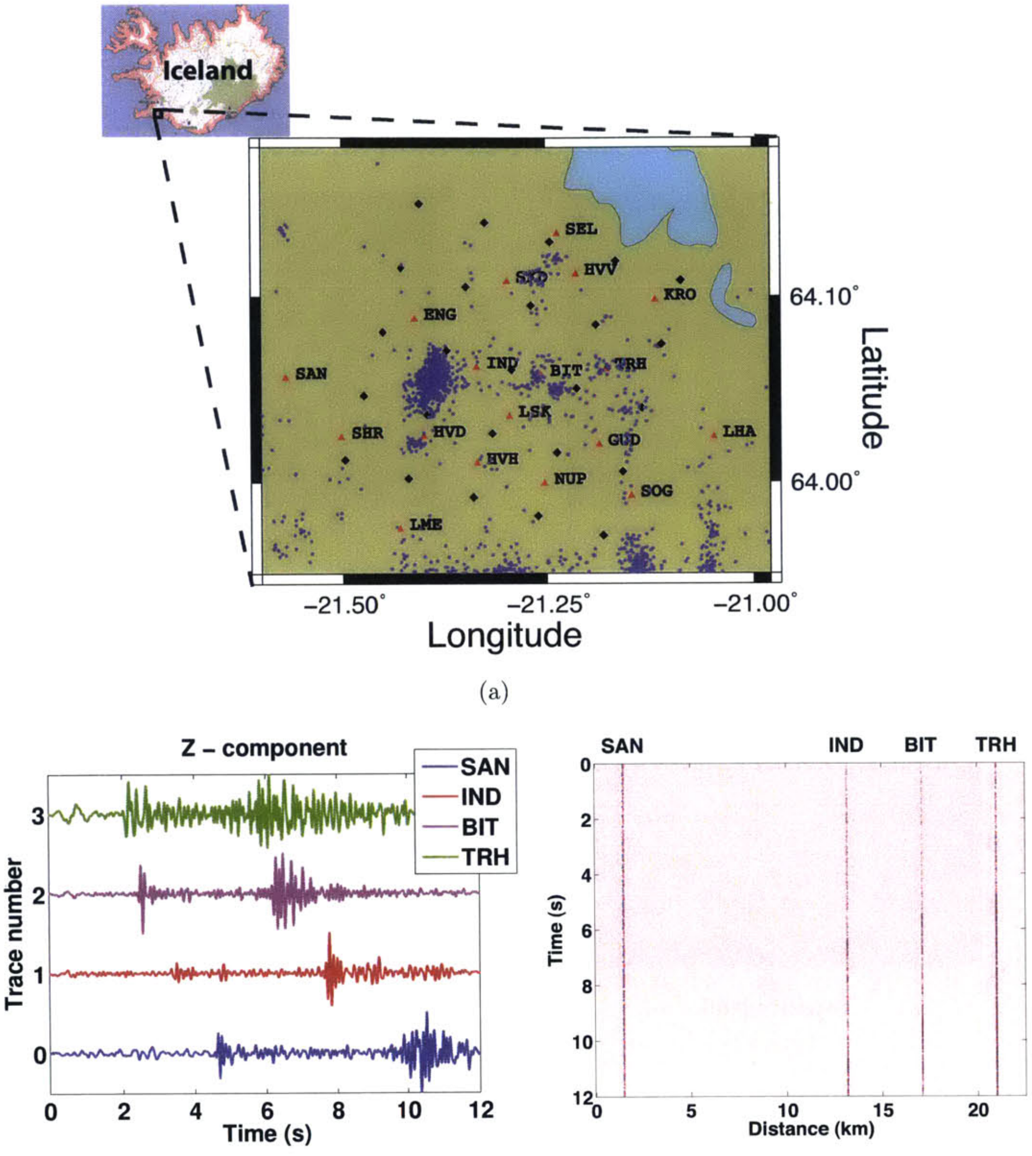

(a)

(b)

(c)

Figure 2-13: (a) Map of the investigated area in Iceland with micro-seismic field data. The blue dots mark the earthquake locations projected onto the surface, the red triangles refer to locations of the recording stations named with three letters, and the black diamonds denote the computational grid points of the regional travel time tomography done by Tryggvason et al. (2002). (b) Representative normalized and filtered Z-component traces that are recorded at the surface along a 2D line at the latitude of 64.06° and sorted into (c) a common shot gather. The relative position of the traces in the common shot gather corresponds to the relative position of their stations on the surface; the trace #0 from station SAN in (b) is the leftmost trace in (c).

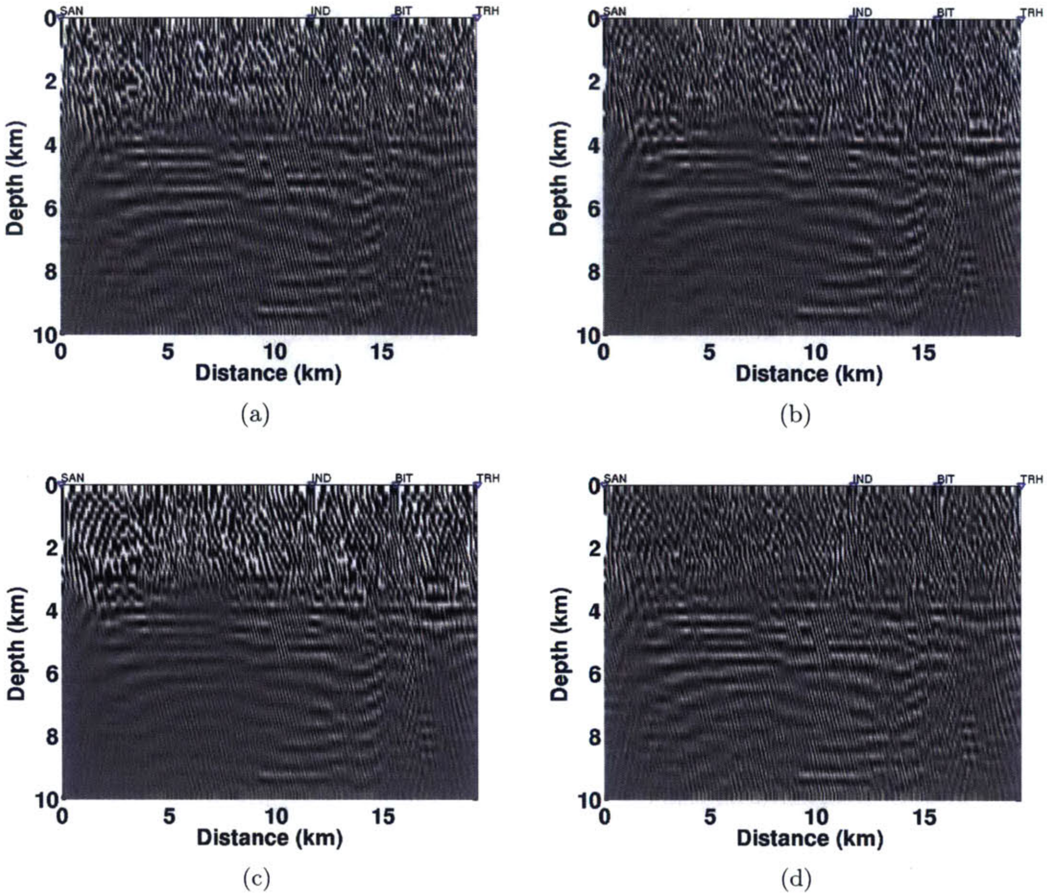

(a) (b) (c) (d)

Figure 2-14: Migrated images produced with 17 sources recorded at 4 receivers at the surface and after applying the Laplacian filter using: (a) de-convolutional SICP-IC with P-wave illumination (equation 2.13), (b) de-convolutional SICP-IC with S-wave illumination (equation 2.14) (c) cross-correlational SICP-IC (equation 2.15) and (d) de-convolutional SICP-IC with normalized illumination (equation 2.20). The seismic data, before migration, were band-pass filtered between 2 and 12 Hz and normalized based on their maximum amplitude. Note that the amplitudes in (d) are more balanced including the region at shallow depths as well as depths between 4 and 6 km.

Shabelansky et al., 2013b) particularly when the imaging target region is known.

The second question, which is related to the key component of deconvolutional amplitude-balancing ICs, given in equations 2.13, 2.14 and 2.20, is how to choose the stabilization factor, ϵ. This factor controls the stability and quality of the imaging process (i.e., ensuring that division by zero is not taking place) and is different for different ICs and data sets. To our knowledge, there is no good strategy to estimate this parameter before an image has been constructed. An approach from Marquardt (1963) may facilitate the procedure for estimating an appropriate stabilization factor for seismic imaging.

The third question is how sensitive the SICP imaging conditions to uncertainties in both P- and S-wave speeds, and how these uncertainties can be mitigated. The sensitivity of the SICP-IC to variations in both wave speeds can be high and the image can be completely degraded in some cases. However, when the Vp/Vs is preserved the image degradation is less severe. In chapter 4, I will present an approach based on the SICP-IC for both P- and S-wave speed reconstruction using the cross-correlational form. An approach for velocity updating based on the de-convolutional form is a subject of future research.

2.6 Conclusion

We have presented cross-correlational and de-convolutional forms of a data-driven source independent converted-phase wave imaging condition (SICP-IC), and investigated their relationship with reflection, transmission and conversion coefficients through a newly introduced concept of conversion ratio coefficients. We illustrated the properties of the conversion ratio coefficients and demonstrated their use through de-convolutional imaging conditions with different types of illumination compensation. We tested the imaging conditions with the synthetic Marmousi model and field micro-seismic data. The results showed clear advantages when appropriate illumination compensation is applied. This opens up the possibility of source-independent full-wavefield imaging with true amplitudes; a method which can considerably improve the quality and resolution of images.

2.7 Acknowledgement

We thank ConocoPhillips and the ERL founding members consortium at MIT for funding this work. We acknowledge Sudhish Kumar Bakku for helpful discussions. We also acknowledge Ari Tryggvason and Olafur Gudmundsson from Uppsala University for providing velocity models and for collaboration with collecting the micro-seismic data.

2.8 Appendix - Wavefield separation using acceleration decomposition

The wavefield separation is derived from the isotropic elastic wave equation for a smooth medium (Aki & Richards, 2002, page 64) as

$$\underline{\ddot{u}} = \alpha^2 \nabla\nabla \cdot \underline{u} - \beta^2 \nabla \times \nabla \times \underline{u}, \tag{2.21}$$

where $\underline{u}(\underline{x}, t)$ and $\underline{\ddot{u}}(\underline{x}, t)$ are displacement and acceleration vector wavefields, $\alpha(\underline{x})$ and $\beta(\underline{x})$ are the P- and S-wave speeds, and ∇, $\nabla\cdot$ and $\nabla\times$ are gradient, divergence and curl operators, respectively. Since the acceleration wavefield is decomposed from $\alpha^2\nabla\nabla \cdot \underline{u}$ and $-\beta^2\nabla \times \nabla \times \underline{u}$, we define $\underline{\ddot{u}} = \underline{\ddot{u}}_p + \underline{\ddot{u}}_s$ with

$$\underline{\ddot{u}}_p(\underline{x}, t) = \alpha^2(\underline{x}) \nabla\nabla \cdot \underline{u}(\underline{x}, t), \qquad \underline{\ddot{u}}_s(\underline{x}, t) = -\beta^2(\underline{x}) \nabla \times \nabla \times \underline{u}(\underline{x}, t), \tag{2.22}$$

where $\underline{\ddot{u}}_p$ and $\underline{\ddot{u}}_s$ are the P- and S-components of acceleration. Note that using this separation form, the images produced consistent amplitude polarity and do not require additional treatment. Since $\alpha(\underline{x})$ and $\beta(\underline{x})$ are in general smooth for imaging, we remove the effect of the P- and S-wave speeds on wavefield separation and obtain equation 2.6. Note that by removing the (squared) velocities from equation 2.22, we obtain units of inverse displacement (i.e., $1/m$). Thus for the sake of simplicity, we denote the separated wavefields $\underline{\ddot{u}}_p$ and $\underline{\ddot{u}}_s$ with the velocities removed in equation 2.6 as $\underline{u}_p$ and $\underline{u}_s$.

Chapter 3

Source-Independent Migration-based Seismic Trace Interpolation[1]

3.1 Summary

Multi-component elastic seismic data collected at large offsets have the potential to be used in micro seismic imaging and monitoring. However, the types of receiver surface deployments used for micro-seismic monitoring are generally very sparse, and thus the data used for imaging from these receivers cause receiver-migration-operator artifacts that severely contaminate the shallow part of the image. In this chapter, we present a data-driven method that alleviates these imaging artifacts. The method is based on converted-phase elastic seismic migration and de-migration. We show that despite the spatial aliasing of the recorded data, we are able to suppress the receiver migration-operator artifacts and reconstruct the shallow part of the image. The merit of this approach is that it is elastic, fully data-driven (i.e, independent of source parameters), and does not suffer from migration operator source aliasing, when a small number of shots or micro-seismic events are used. We present a derivation of

---

[1] Shabelansky, A.H., Malcolm, A.E., Fehler, M.C., and Rodi, W.L., SEG 84th Annual Meeting, Denver 2014

the method and test it with a synthetic model and a field data set from a geothermal reservoir with abundant natural and induced seismicity.

3.2 Introduction

Surface micro-seismic acquisitions often have sparse receiver geometries and thus challenge standard seismic imaging by introducing migration operator artifacts, particularly in the shallow subsurface. Conventional data interpolation methods (applied before the imaging step), which are based on the exploitation of structure in a predefined space (i.e, Fourier, wavelet, curvelet) (e.g., Spitz, 1991; Gülünay, 2003; Fomel, 2003; Abma & Kabir, 2006; Naghizadeh & Sacchi, 2007; Herrmann & Hennenfent, 2008; Curry, 2010, and others), cannot typically provide a solution as the data are extremely aliased and noisy. However, imaging using sparse seismic data is still possible for the deeper part of the earth where aliasing is less of a problem. It has also been shown that after the migration step, the image can be iteratively refined and migration artifacts can be suppressed using the so-called least-squares migration (LSM) approach (e.g., Nemeth et al., 1999; Duquet et al., 2000; Dong et al., 2012), similar to the data mapping approach of Bleistein & Jaramillo (2000). Key components of the LSM are migration and de-migration steps in which a migrated image is calculated from data and data are calculated from the previously computed image. Standard wave equation based migration and de-migration (the latter obtained by Born modeling) require source information (i.e., location, mechanism, time-function), which in an active source experiment is typically known or can be estimated with high precision. However, in passive-source monitoring the source properties are not directly available, and thus need to be estimated generally with high uncertainty. Thus, standard migration and de-migration from passive sources become cumbersome and uncertain.

To overcome the need to estimate source information, we propose to use the converted phase imaging approach (chapter 2) for migration, during which we store the back-propagated wavefield in time and then use it in the de-migration in reverse order (i.e., forward) in time as the incident wavefield for Born modeling. Note that for reflection acquisition, the subsurface medium is generally sampled only with the scattered wavefield (i.e., a very small portion of the total wavefield). In the transmission micro-seismic geometry, by contrast, the medium is also sampled with direct waves that contain a large portion of the total wavefield and are recorded at the receivers, despite sparse receiver deployment. Thus, to satisfy the Born approximation (i.e, incident wavefield is of the same order as the total wavefield), it is appropriate to use the back-propagated transmission wavefield (in reverse order in time) as an incident wavefield for Born modeling.

In this chapter, we outline a converted phase migration-based interpolation approach and test it with a synthetic model and a field micro-seismic data from a geothermal reservoir in Iceland. We show that despite a very limited number of stations, full waveform micro-seismic imaging can be a powerful tool.

3.3 The algorithm

The imaging/migration step is the source-independent converted-phase elastic reverse time migration (SICP-ERTM), which is given in equation 2.15 for a single source as

$$I(\underline{x}) = \int_T^0 \underline{u}_p(\underline{x}, t) \cdot \underline{u}_s(\underline{x}, t) dt, \tag{3.1}$$

where $\cdot$ is the dot product between vector components, $\underline{x}$ and t are the space (vector) and time coordinates, respectively, and T is the maximum recorded time; it is at the lower limit of the integral (i.e., the data are propagated backward in time). The wavefields $\underline{u}_p$ and $\underline{u}_s$ are the P- and S-components of the back-propagated vector wavefields decomposed from the isotropic, smooth, elastic wave equation as

$$\underline{u}_p = \nabla\nabla \cdot \underline{u} \qquad \underline{u}_s = -\nabla \times \nabla \times \underline{u}, \tag{3.2}$$

where ∇, $\nabla\cdot$ and $\nabla\times$ are the gradient, divergence and curl, respectively, $\underline{u}(\underline{x}, t)$ is the displacement vector wavefield (more details are given in appendix 2.8). The reason for using this imaging approach stems from two important advantages. First, it requires only one elastic propagation to form an image as oppose to the two propagations used in the standard imaging approach (one forward and one backward in time). The second, more important, advantage is that no source information is needed to form an image, which reduces the imaging uncertainty and computational cost. Note also that we decompose the P- and S-wavefields using equation 3.2 rather than using the more computationally efficient Helmholtz decomposition. The reason for this choice stems from the fact that the separated wavefields, using equation 3.2, have consistent amplitude polarity, unlike those obtained by the Helmholtz decomposition which require additional treatment for signal amplitude (e.g., Du et al., 2012).

The de-migration step (i.e, the Born modeling) is obtained using the Born approximation of the general form of the elastic wave equation as:

$$\rho_0 \delta \underline{\ddot{v}} - \nabla \cdot \mathbf{C_0} : \nabla \delta \underline{v} = \underline{f}, \tag{3.3}$$

with

$$\underline{f} = (\nabla \cdot \delta \mathbf{C} : \nabla - \delta \rho)\, \underline{v}_0, \tag{3.4}$$

where : is the double dot (dyadic) product, $\rho(\underline{x})$ is density, $\mathbf{C}(\underline{x})$ is the fourth order stiffness tensor and $\underline{v}(\underline{x}, t)$ is the forward propagating displacement vector wavefield, each of which are decomposed as $\rho(\underline{x}) = \rho_0(\underline{x}) + \delta\rho(\underline{x})$, $\mathbf{C}(\underline{x}) = \mathbf{C}_0(\underline{x}) + \delta\mathbf{C}(\underline{x})$ and $\underline{v}(\underline{x}, t) = \underline{v}_0(\underline{x}, t) + \delta\underline{v}(\underline{x}, t)$. The subscript 0 refers to a background quantity and δ denotes a perturbation. The perturbation term, $\nabla \cdot \delta\mathbf{C}(\underline{x}) : \nabla - \delta\rho(\underline{x})$, is non-zero at discontinuities in the medium and thus is related to the image; we denote this image as $I_{stack}(\underline{x})$. The relation between the displacement wavefields in equation 3.2 and 3.3 is $\underline{v}_0(\underline{x}, t) = \underline{u}(\underline{x}, T - t)$.

Once the wavefields $\delta\underline{v}(\underline{x}, t)$ are modeled, their time records at the receiver positions, $\underline{x}_{obs}$, are used for SICP-ERTM imaging along with the original time records, $\underline{d}^{orig}(\underline{x}_{obs}, t)$, as

$$\underline{d}^{new}(\underline{x}_{obs}, t) = \gamma \underline{d}^{orig}(\underline{x}_{obs}, t) + \delta\underline{v}(\underline{x}_{obs}, t), \tag{3.5}$$

where $\underline{d}^{new}(\underline{x}_{obs}, t)$ are new time records and γ is a pre-defined weight. The values for

γ depend primarily on the data illumination and the presence of the converted-phase waves in the data and vary between 0 for no weight to the original data and a very large number, which diminishes the effect of the interpolation.

3.3.1 Description of the algorithm

The proposed algorithm consists of the following steps:

1. Back propagate each elastic shot gather, $\underline{d}^{orig}(\underline{x}_{obs}, t)$, in time. During the back-propagation:
    (a) Decompose $\underline{u}(\underline{x}, t)$, into P-and S- wavefields using equation 3.2.
    (b) Construct an image, $I(\underline{x})$, using equation 3.1.
    (c) Store the displacement (or particle-velocity) vector wavefields, $\underline{u}(\underline{x}, t)$.
2. Stack over all images to obtain an image, $I_{stack}(\underline{x})$.
3. For each shot (or earthquake):
    (a) Forward propagate the stored wavefield, $\underline{v}_0(\underline{x}, t) = \underline{u}(\underline{x}, T - t)$, multiplied by the image, $I_{stack}(\underline{x})$, to obtain $\delta\underline{v}(\underline{x}, t)$.
    (b) Record the time history of the forward-propagated wavefield at the receiver depth, $\delta\underline{v}(\underline{x}_{obs}, t)$, and construct the new shot gather, $\underline{d}^{new}(\underline{x}_{obs}, t)$, using equation 3.5.
4. Repeat steps 1(a), 1(b) and 2 with the new shot gathers.

3.4 Results

To examine the proposed approach for interpolation-based SICP-ERTM, we test it with two data sets: a synthetic data set based on the field data and a field data set from the passive source micro-seismic monitoring of a geothermal area in Iceland. The acquisition geometry is transmission for both tests, i.e., the recording stations are placed on the surface and sources are located at depth (n.b., some earthquakes in the field data occurred outside of the imaging/computational region). All elastic wave solutions for migration and de-migration are modeled with a 2D finite-difference solver, using a second order in time staggered-grid pseudo-spectral method with perfectly matched layer (PML) absorbing boundary conditions (details are shown in appendix A).

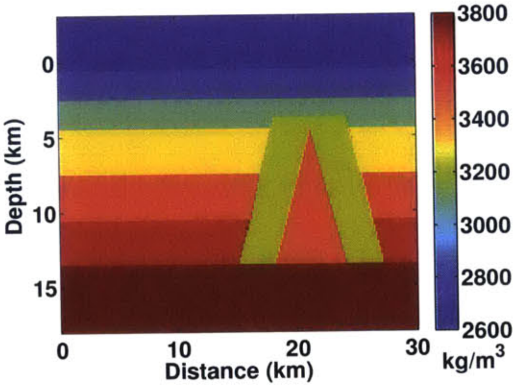

Figure 3-1: Density model used for the synthetic test.

3.4.1 Synthetic model

The synthetic model, shown in Figure 3-1, is the density model which defines the contrast of the medium. The P- and S-wave speeds are constant 4.5 km/s and 2.5 km/s, respectively. The number of grid points in the model is $N_z = 140$ and $N_x = 200$, and the spatial increments are $\Delta x = \Delta z = 0.15$ km. We generate 21 isotropic sources equally distributed at 15.0 km depth with a horizontal increment of 1.2 km using a Ricker wavelet with a peak frequency of 6 Hz and Δt of 0.006 s. The data are recorded with two-component receivers that are equally distributed on the surface, 0 m, and span the computational grid. A representative shot gather (Z-component) generated from $(x, z) = (7.8, 15)$ km is shown in Figure 3-2(a), and the SICP-ERTM imaging result using 21 shots is shown in Figure 3-2(b).

Having calculated the elastic seismic data records, we decimate them by about 97 % (see a representative shot gather in Figure 3-3(a)), leaving only 4 live traces.

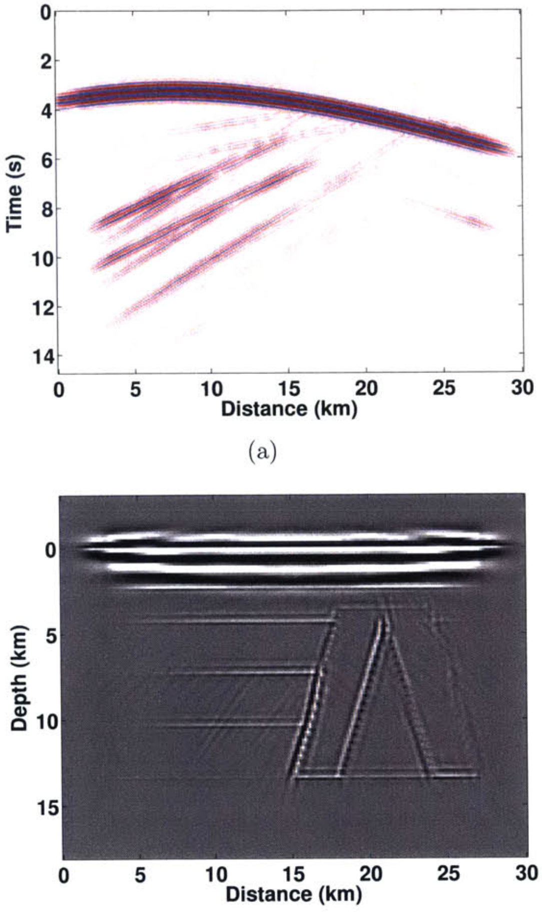

(a)

(b)

Figure 3-2: (a) A representative common shot gather recorded at the surface, 0 km, from a shot at depth $(x, z) = (7.8, 15.0)$ km. (b) SICP-ERTM imaging result obtained with all 21 shots. Although there are a few artifacts, the structures are well-imaged.

The reason for this small number is to mimic the field data example discussed below. Next, we construct an image using the 21 decimated shots (Figure 3-3(b)). We observe that the image is contaminated with noise due to the data sparsity. Using the obtained image and stored wavefield from back-propagations, $\underline{v}_0(\underline{x}, t)$, we apply Born modeling with a constant density of 3000 kg/m^3 for ρ_0 (see equation 3.3). In Figure 3-3(c) we show the modeled/reconstructed traces for the shot gather shown in Figure 3-3(a). We observe that although the direct P-wave is clearly absent and the data are somewhat noisy, the missing traces are reconstructed to some degree. To test the quality of the reconstructed data, we add the reconstructed data to the initial data (comprising 4 live traces) with $\gamma = 1.8$ (equation 3.5), and calculate the SICP-ERTM image with 21 shots (see Figure 3-3(d)). In Figure 3-3(d), we observe that although a number of artifacts remain, many are also removed and the noise level in the shallow part of the image is reduced, without affecting the image quality as compared to Figure 3-3(b). In this synthetic example the weight, γ, for the original decimated data is high because most converted waves here are highly dependent on the direct P-wave, which was clearly missing in the Born-modeled data. However, if the conversions are primarily generated by other (non-direct) waves, the weight for the original decimated data can be small or even set to zero. This is illustrated with the field data example.

3.4.2 A field data example from a micro-seismic monitoring

The second data example is field, passive source, micro-seismic data from a geothermal area in Iceland with abundant natural and induced seismicity. Only four stations along a 2D line are available for 2D imaging. In Figure 3-4(a), we show a representative common shot gather (Z-component) for these four traces from a single earthquake. The relative position of the traces in the common shot gather corresponds to the relative locations of the stations at the surface, $\underline{x}_{obs} = (x, z_{surface} = 0 \text{ km})$. The extracted time window record of $T = 12$ s and $\Delta t = 0.005$ s is band-pass filtered between 2 and 12 Hz. The computational grid is $N_z = 90$ and $N_x = 150$ and the spatial increments are $\Delta z = 0.2$ km and $\Delta x = 0.15$ km. To construct an image of the

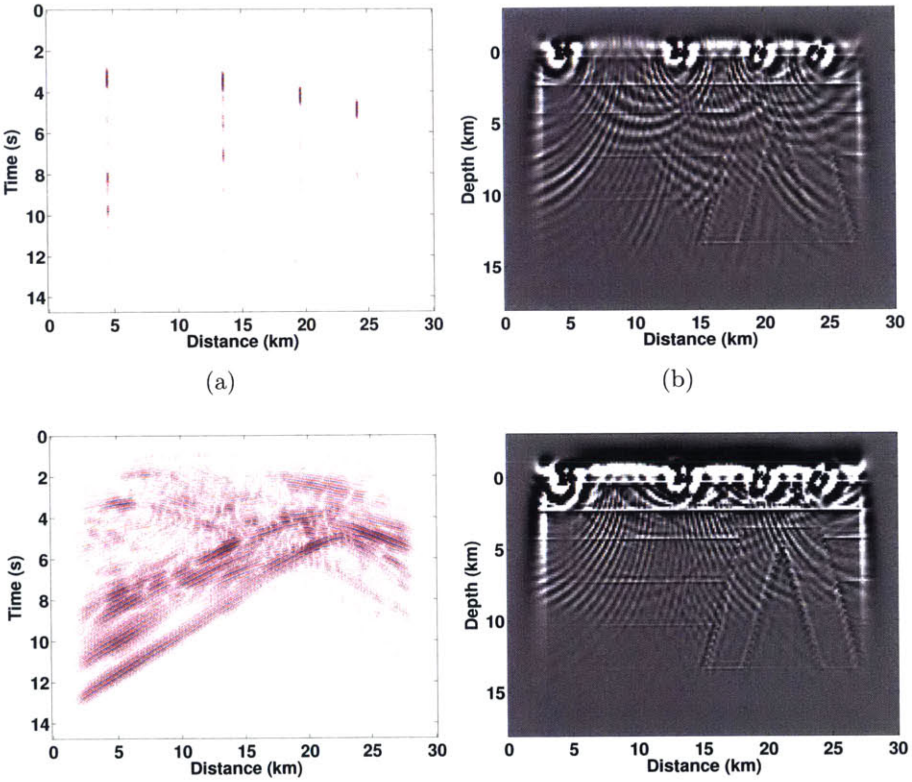

(a) (b)

(c) (d)

Figure 3-3: Same data as shown in Figure 3-2: (a) shot gather with only 4 live traces (i.e., about 97 percent of original traces were removed), (b) SICP image obtained with 21 shots using only 4 live traces, (c) modeled data using Born modeling, (d) SICP image obtained with 21 modeled shots using $\gamma = 1.8$.

geothermal area (using equation 3.1) we use 32 events (i.e., earthquakes) of moment magnitude between 0.9 and 1.2, and P- and S-wave speeds, previously estimated by conventional regional-scale travel-time tomography (Tryggvason et al., 2002). In Figure 3-4(b), we show the SICP-ERTM image stacked over all 32 events. We observe (in Figure 3-4(b)) that although the deeper part of the image is reasonable, the shallow part is completely contaminated.

Now, after having generated a stacked image, $I_{stack}(\underline{x})$, we use it along with the stored wavefield $\underline{v}_0(\underline{x}, t)$, for each event, as input for generating the forward propagating wavefield $\delta v(\underline{x}, t)$ (i.e, Born modeling using equations 3.3 and 3.4). The result in Figure 3-4(c) is the modeled seismic shot gather that corresponds to that shown in Figure 3-4(a). We observe that the relative amplitude of the traces shown in Figure 3-4(a) are preserved in Figure 3-4(c) and additional data are generated at previously empty traces. By migrating only these new 32 seismic shot gathers (without using the original data, $\gamma = 0$), we obtain the new migrated image that is shown in Figure 3-4(d). We observe that the deeper part (below 4.0 km) remains almost the same whereas the artifacts in the shallow part are considerably suppressed.

3.5 Conclusions

In this study, we presented a practical, data-driven, approach for migration-based seismic trace interpolation of sparse transmission, micro-seismic data using converted-phases. We demonstrated the approach with synthetic and field data using only an extremely small number of stations. We showed that, using this approach, it is possible to image not only the deeper part of the earth but also its shallow part, without any sort of source information. This opens up the possibility of imaging with sparsely recorded micro-seismic data without the artifacts such imaging usually generates in the shallow subsurface.

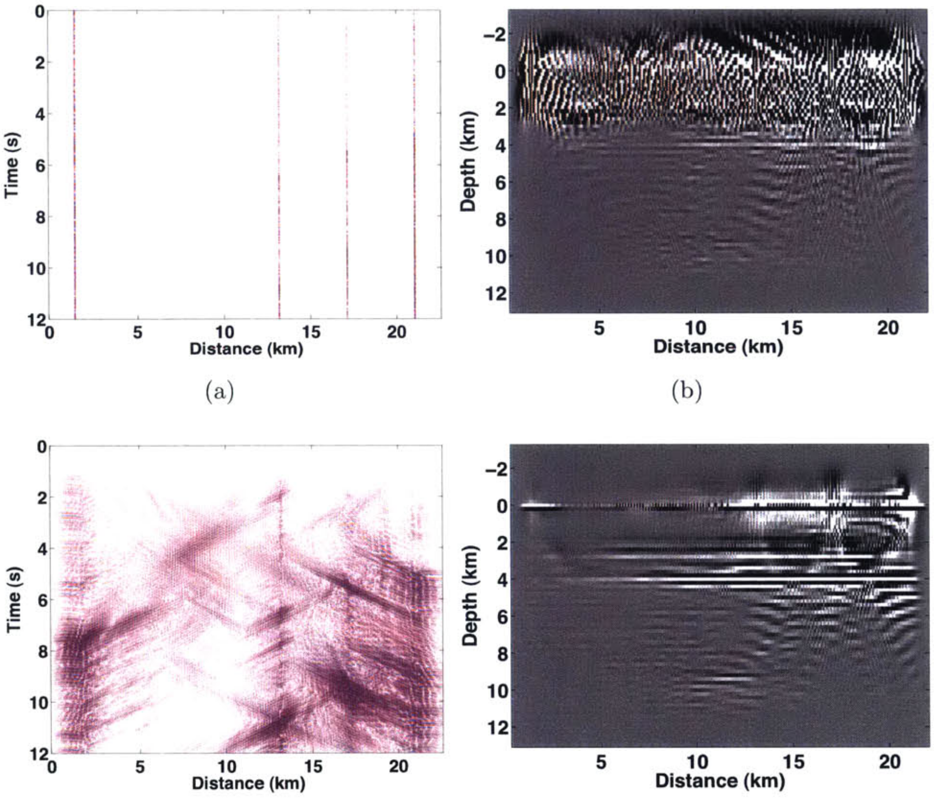

(a) (b) (c) (d)

Figure 3-4: (a) Seismic traces from four receivers sorted into a common shot gather (Z-component). The data are band-pass filtered with passband 2 and 12 Hz. (b) SICP-ERTM image obtained with 32 events (earthquakes). The structure on the right corresponds to the structure of a volcano. (c) Born-modeled common shot gather corresponding to that is shown in (a). (d) SICP-ERTM image obtained with the Born-modeled data and the same 32 events as in (b) (using $\gamma = 0$). The structure of the deeper part of the image is preserved and the artifacts from shallow part of the image are suppressed.

Chapter 4

Source-Independent Full Wavefield Converted-Phase Elastic Wave Equation Migration Velocity Analysis[1]

4.1 Summary

Converted phase elastic seismic signals are comparable in amplitude to the primary signals recorded at large offsets and have the potential to be used in seismic imaging and velocity analysis. We present an approach for converted-phase elastic wave equation velocity analysis that does not use source information and is applicable to surface-seismic, micro-seismic, tele-seismic and VSP studies. Our approach is based on the cross-correlation between reflected or transmitted PP and converted-phase PS (and/or SS and converted-phase SP) waves propagated backward in time, and is formulated as an optimization problem with a differential semblance criterion objective function for the simultaneous update of both P- and S-wave velocity models. The merit of this approach is that it is fully data-driven, uses full waveform information,

---

[1] Shabelansky, A.H., Malcolm, A.E., Fehler, M.C., Shang, X. and Rodi, W.L., 2015, Geophysical Journal International

and requires only one elastic backward propagation to form an image rather than the two (one forward and one backward) propagations needed for standard RTM. Moreover, as the method does not require forward propagation, it does not suffer from migration operator source aliasing when a small number of shots are used. We present a derivation of the method and test it with a synthetic model and field microseismic data.

4.2 Introduction

In recent years, full waveform seismic imaging and velocity analysis methods have become standard and the use of elastic waves is now drawing more attention. Converted phase (CP) waves are an integrated part of the recorded elastic seismic signal and are investigated in numerous studies in the research areas of VSP data (e.g., Esmersoy, 1990; Stewart, 1991; Xiao & Leaney, 2010), surface reflection (e.g., Purnell, 1992; Stewart et al., 2003; Hardage et al., 2011) and transmission seismic data (e.g., Vinnik, 1977; Vinnik et al., 1983; Bostock et al., 2001; Rondenay et al., 2001; Shang et al., 2012; Brytic et al., 2012; Shabelansky et al., 2013c). In particular, e.g., Xiao & Leaney (2010); Shang et al. (2012) showed that the converted phase seismic images can be calculated using one elastic propagation without using source information (i.e., location, mechanism, time-function). Source information is generally considered mandatory in standard seismic imaging and velocity analysis. However, in passive monitoring source information is generally not available and in active source surveys seismic data require special treatment for frequency matching due to coupling differences between soil and vibro-seis or dynamite casing. These factors affect the accuracy of the imaging and velocity estimation and add computational and processing cost. Moreover, converted-phase elastic seismic imaging is shown to have higher resolution in Xiao & Leaney (2010) and fewer artifacts than reflection type imaging in Shabelansky et al. (2012b).

In this chapter we present a source independent converted phase velocity analysis method that is formulated based on the framework of cross-correlational converted-phase imaging (chapter 2) and wave equation migration velocity analysis (WEMVA) (e.g., Biondi & Sava, 1999; Sava & Biondi, 2004; Albertin et al., 2006; Shen, 2004, 2012). We refer to this method as source independent converted phase WEMVA (SICP-WEMVA). Like WEMVA, SICP-WEMVA depends strongly on starting (initial) velocity models (P- and S-wave speeds) and optimization algorithms with their parameters. SICP-WEMVA is typically less sensitive to the cycle skipping that is a problem for full waveform inversion, but it has lower resolution than full waveform inversion. The objective functional for converted P to S phases in source-dependent WEMVA (i.e., CP-WEMVA using forward/source propagation for P-wave and backward propagation for S-wave) appears to be convex (Yan & Sava, 2010), and thus we expect SICP-WEMVA to also exhibit favorable properties for estimating large-scale velocity models. Unlike WEMVA, SICP-WEMVA (and CP-WEMVA) uses interference between different wave types (i.e., P- and S-waves), and thus the resolution and stability of the two methods are not the same. Also, since SICP-WEMVA backpropagates data solely from receivers and does not depend on source information, it can be performed locally in the vicinity of the receivers only. This reduces the computational cost of iterative velocity analysis.

This chapter is divided into three parts. In the first part, we present a source-independent converted phase imaging condition in an extended domain. We use this to formulate an objective functional for gradient-based optimization. In the second part we present the derivation of the SICP-WEMVA velocity model optimization scheme. In the third part we show results of applying SICP-WEMVA to a synthetic model and its application to field data from a geothermal reservoir with abundant natural and induced seismicity.

4.3 Theory of SICP-WEMVA

Source-Independent Converted-Phase WEMVA (SICP-WEMVA) is a gradient-based iterative optimization scheme whose residuals are calculated from extended-domain migrated images. The gradients are formed from the backward and forward propagating in time seismic data and image residuals. We present below the derivation of the method, a summary of the algorithm and its practical implementations.

4.3.1 Extended source-independent converted-phase imaging condition (ESICP-IC)

We start our derivation using the isotropic elastic wave equation

$$\underline{\ddot{u}} = \frac{\lambda + 2\mu}{\rho}\nabla\nabla\cdot\underline{u} - \frac{\mu}{\rho}\nabla\times\nabla\times\underline{u} + \frac{1}{\rho}\nabla\lambda(\nabla\cdot\underline{u}) + \frac{1}{\rho}\nabla\mu\cdot\left[(\nabla\underline{u}) + (\nabla\underline{u})^T\right], \quad (4.1)$$

where $\underline{u}(\underline{x}, t)$ and $\underline{\ddot{u}}(\underline{x}, t)$ are the displacement and acceleration vector wavefields, $\lambda(\underline{x})$, $\mu(\underline{x})$, and $\rho(\underline{x})$ are the two Lamé parameters and density, ∇, $\nabla\cdot$, and $\nabla\times$ are the gradient, divergence and curl, and $\underline{x} = (x, y, z)$, and t are the spatial and time variables, respectively. The right hand side of equation 4.1 consists of four terms: two with Lamé parameters and two with their gradients. The terms with the gradients are significant only at interfaces/discontinuities in subsurface medium and they are responsible for generation of reflected, transmitted and converted-phase seismic data.

For the purpose of imaging, we assume smooth Lamé parameters (i.e., taking only the first two terms on the right hand side of equation 4.1), and obtain (Aki & Richards, 2002, page 64)

$$\underline{\ddot{u}} = \hat{\alpha}\nabla\nabla\cdot\underline{u} - \hat{\beta}\nabla\times\nabla\times\underline{u}, \quad (4.2)$$

where the parameters $\hat{\alpha}(\underline{x})$ and $\hat{\beta}(\underline{x})$ are defined through the P- and S-wave velocities, $\alpha(\underline{x})$ and $\beta(\underline{x})$, as

$$\hat{\alpha} = \alpha^2 = \frac{\lambda + 2\mu}{\rho}, \qquad \hat{\beta} = \beta^2 = \frac{\mu}{\rho}. \quad (4.3)$$

Since we use the isotropic elastic wave equation, the acceleration wavefield can be decomposed as $\underline{\ddot{u}} = \underline{\ddot{u}}_p + \underline{\ddot{u}}_s$, where

$$\underline{\ddot{u}}_p(\underline{x}, t) = \hat{\alpha}(\underline{x})\nabla\nabla \cdot \underline{u}(\underline{x}, t), \qquad \underline{\ddot{u}}_s(\underline{x}, t) = -\hat{\beta}(\underline{x})\nabla \times \nabla \times \underline{u}(\underline{x}, t). \tag{4.4}$$

Then, the source independent converted phase imaging condition (SICP-IC) for N_e sources (i.e., explosions or earthquakes) is given as the zero lag in time cross-correlation between the back-propagated P- and S-acceleration vector-wavefields, $\underline{\ddot{u}}_p$ and $\underline{\ddot{u}}_s$,

$$I(\underline{x}) = \sum_{j}^{N_e} \int_{T}^{0} \underline{\ddot{u}}_p^j(\underline{x}, t) \cdot \underline{\ddot{u}}_s^j(\underline{x}, t) dt, \tag{4.5}$$

where $\cdot$ is the dot product between vector components (e.g., vertical, radial and transverse), the superscript j refers to the source index, and T is the maximum recording time; it is at the lower limit of the integral (i.e., the data are propagated backward in time).

This imaging condition has three very important properties: first, no source information (i.e., location, mechanism, time-function) is required; second the image can be constructed only in the vicinity of the receivers (i.e., far from the sources); and third, the image can be constructed during the backward propagation and no wavefield storage is required. These properties reduce the computational cost and memory storage, and more importantly improve the image quality in comparison with standard reverse-time migration (RTM). Note also that we decompose the P- and S-wavefields using equation 4.4 rather than using the more computationally efficient Helmholtz decomposition. The reason for this choice stems from the fact that the separated wavefields, using equation 4.4, have consistent amplitude polarity for imaging, unlike those obtained by Helmholtz decomposition, which require additional treatment for signal amplitude (e.g., Du et al., 2012).

To provide intuition for the imaging condition in equation 4.5, we show in Figure 4-1(a) a snapshot of an elastic wave propagation from a single point source, through a horizontal interface. Figure 4-1(b) illustrates the wavefields schematically above the interface. The red dots in Figure 4-1(b) correspond to constructively interfering image

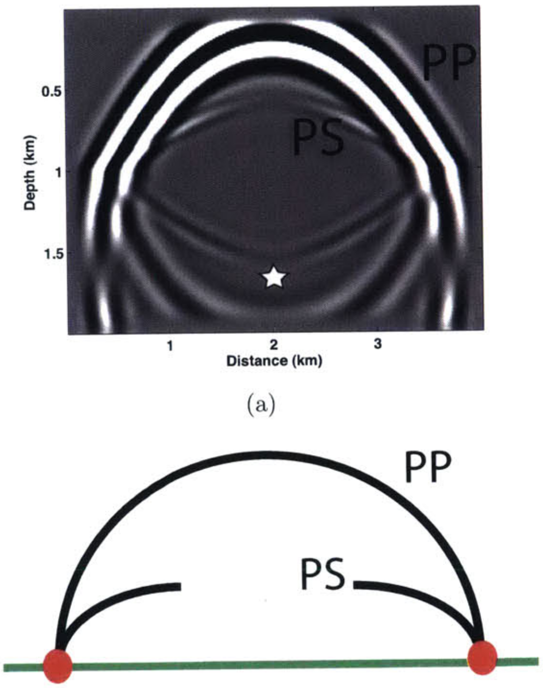

(a)

(b)

Figure 4-1: (a) A snapshot of the Z-component elastic wavefield generated from an isotropic point source at the position $(x, z) = (2.0, 1.7)$ km, marked with a star, and propagating through a horizontal interface at a depth of 1 km. (b) Schematic illustration of the wavefields shown in (a) above the horizontal interface. The black curves refer to the transmitted P and S wavefields (PP and PS) through the interface, marked by horizontal green line. The big red dots mark the points where the two wavefields interfere constructively and an image is formed.

points at which the energy of the zero-lag in time cross correlation between P- and S-wavefields is maximized. When we sum over multiple sources, N_e, in equation 4.5, the signal to noise ratio (S/N) of the interfering image points increases.

This concept is valid when the P- and S-wave speed models are correct. However, when the velocities have error, the interference between P- and S-waves does not occur at the correct image points and energy leaks to adjacent points. To quantify the leak and interference mis-positioning, we introduce an extended source-independent converted-phase imaging condition (ESICP-IC) in the so-called subsurface space lag, $\underline{h} = (h_x, h_y, h_z)$, as

$$I(\underline{x}, \underline{h}) = \sum_{j}^{N_e} \int_{T}^{0} \underline{\ddot{u}}_p^j(\underline{x} - \underline{h}, t) \cdot \underline{\ddot{u}}_s^j(\underline{x} + \underline{h}, t) dt. \tag{4.6}$$

The concept of extension is adopted from acoustic reflection imaging where the extended image is typically called a common image gather (CIG), and the subsurface space lag, $\underline{h}$, is called the subsurface offset (e.g., Rickett & Sava, 2002). However, as source information is not involved in SICP-IC and ESICP-IC, the notion of offset is not well defined.

In Figure 4-2 we show schematically the construction of these image gathers, given by equation 4.6, in 2D for a single source and horizontal space lag, h_x, (i.e., we show $I(x = x_f, z; h_x, h_z = 0)$ where x_f is a fixed horizontal image point) that are obtained by continuously shifting the P-wavefield (marked PP) to the right and S-wavefield (marked PS) to the left, as marked with the arrows in Figure 4-2(a). The waves interfere at new points during the shift (i.e., space-lag); these interference points are marked with a blue line and are called the moveout. The small red dot in Figure 4-2(a) corresponds to the initial interference point, marked in Figure 4-1(b) by the big red dot, and the big red dot in Figure 4-2(a) marks the current point of interference along the moveout. Figure 4-2(b) shows the same schematic for negative horizontal space lags, when the P-wavefield is shifted to the left and S-wave to the right. Note that the curved moveout can appear linear for small lags.

To illustrate numerically the construction of the moveout in the space lag gathers

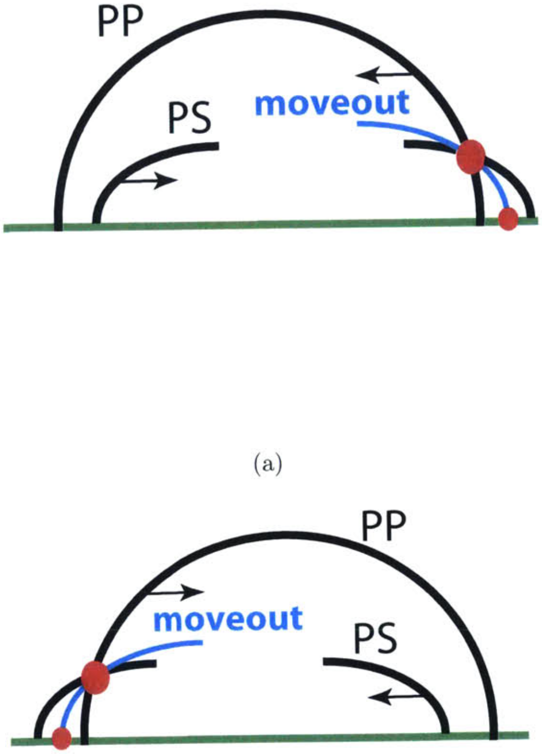

(a)

(b)

Figure 4-2: Schematic illustration of the construction of the space-lag CIG along x direction, h_x, using ESICP-IC (equation 4.6). The black curves are as in Figure 4-1(b) and the big red dots in (a) and (b) mark the current points of interference between the wavefields while the small red dots show the $h_x = 0$ position. The blue curve connecting the big and small red dots follows the points of interference and thus is called the moveout curve. This moveout is obtained by shifting the wavefields in opposite directions; these directions are marked with arrows in (a) and (b), and the length of the shift is called the space-lag.

for the same horizontal interface model, discussed for Figures 4-1 and 4-2, we generate a set of isotropic P-sources from below the horizontal layer at a depth of 1.7 km. We construct the gathers using forward propagated P- and S-wavefields. In Figures 4-3(a) and 4-3(b), we show moveouts for an image point at $x_f = 2$ km obtained from sources generated at $(x, z) = (1.5, 1.7)$ km and $(x, z) = (2.5, 1.7)$ km, below the interface, respectively. These moveouts verify the behavior presented in Figures 4-2(a) and 4-2(b) for correct P- and S-wave velocity models. The summation of the two gathers (Figures 4-3(a) and 4-3(b)) is shown in Figure 4-3(c), where we observe that only the energy around $h_x = 0$ at the depth of the layer interferes constructively. By adding more sources, generated from different horizontal positions below the interface, we obtain more focusing of the energy around $h_x = 0$ (see result in Figure 4-3(d) obtained with 14 sources).

As mentioned above, this focusing is achieved only when the P- and S-wave velocities are correct. When the velocities have error, the energy is no longer focused. To demonstrate this, we add to the correct S-wave model an elliptical lens (i.e., anomaly) with a maximum perturbation of 15% of the background model and perform the same numerical experiment. Figure 4-4(a) shows a result obtained with the same 14 sources as that shown in Figure 4-3(d) with the incorrect S-wave velocity. The idea behind the SICP-WEMVA is to design an optimization procedure that will minimize the energy outside of $\underline{h} = 0$ (see the residual gather for h_x in Figure 4-4(b)) by updating the P and S velocity models. This optimization procedure is discussed in the next section.

4.3.2 Derivation of the SICP-WEMVA optimization

To relate the deviation of energy from $\underline{h} = 0$ in the extended subsurface space lag image gather (shown in Figure 4-4) to the error in velocity, we formalize a gradient-based optimization problem by minimizing the energy at $\underline{h} \neq 0$. We use the differential semblance criterion (Symes & Carazzone, 1991; Shen, 2004, 2012) for the objective

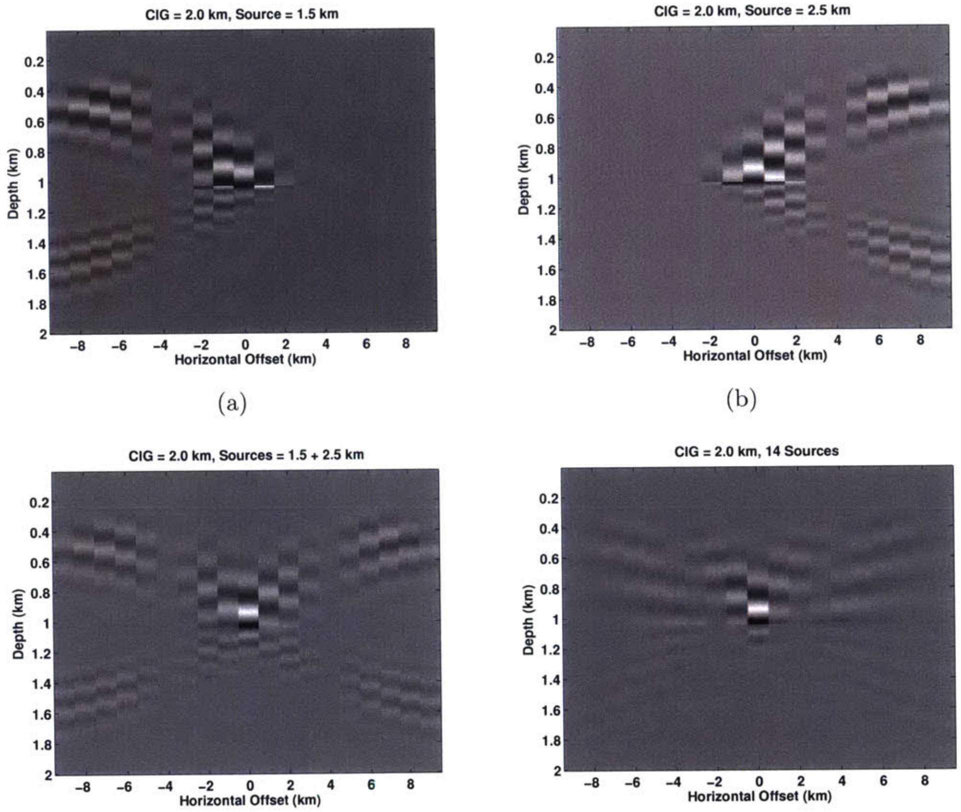

(a) (b)

(c) (d)

Figure 4-3: Converted phase subsurface space lag CIGs at $x_f = 2$ km, $I(x = x_f, z, h_x, h_z = 0)$, obtained with the correct velocity models from a source at position (a) $(x, z) = (1.5, 1.7)$ km, and (b) $(x, z) = (2.5, 1.7)$ km. (c) The summation of the two subsurface space lag CIGs from (a) and (b). (d) The summation over 14 sources generated at the depth of $z = 1.7$ km with a horizontal increment of 0.25 km.

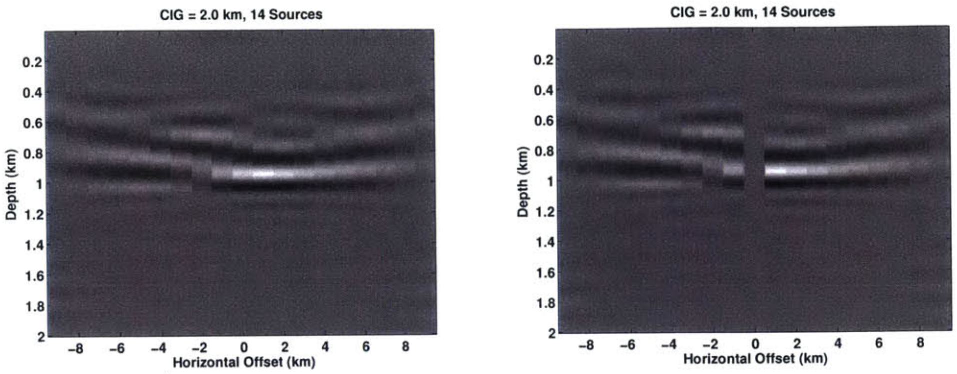

(a) (b)

Figure 4-4: (a) Converted phase subsurface space lag CIGs at $x_f = 2$ km, $I(x = x_f, z, h_x, h_z = 0)$, obtained with the incorrect S-wave velocity with the same shots that are shown in Figure 4-3(d). (b) The residual gather used for the SICP-WEMVA (i.e., signal at $h_x = 0$ was removed).

functional, J, given as

$$J = \frac{1}{2} \int \int_{-\underline{H}}^{\underline{H}} \underline{h}^2 I^2(\underline{x}, \underline{h}) d\underline{h} d\underline{x}, \tag{4.7}$$

where $\underline{H} = (H_x, H_y, H_z)$ is the maximum subsurface space-lag, and $\underline{h} I(\underline{x}, \underline{h})$ is the residual subsurface space-lag CIG; Figure 4-4(b) shows a 2D CIG along the horizontal x direction, h_x, with $H_x = 9.5$ km. The choice of maximum space lag is addressed in appendix B.1. In general we add additional regularization terms to equation 4.7 as discussed in e.g., Shen & Symes (2008); Shen (2012). These terms do not affect the understanding of the derivation and so will not be further discussed.

To formulate our problem as a gradient-based optimization, we use perturbation theory to calculate the gradients of the objective function with respect to the model parameters. We seek to obtain

$$\delta J = \int \left(K_{\hat{\alpha}}(\underline{x}) \delta\hat{\alpha}(\underline{x}) + K_{\hat{\beta}}(\underline{x}) \delta\hat{\beta}(\underline{x}) \right) d\underline{x}, \tag{4.8}$$

where $K_{\hat{\alpha}}$ and $K_{\hat{\beta}}$ are the sensitivity kernels, associated with gradients of the objective function, J, that is perturbed with respect to model parameters, $\hat{\alpha}$ and $\hat{\beta}$, respectively.

The model parameters $\hat{\alpha}$ and $\hat{\beta}$ are defined in equation 4.3.

The sensitivity kernels (gradients) of equation 4.8 are derived in detail in appendix B.2, and have the following convolutional forms

$$K_{\hat{\alpha}}(\underline{x}) = \frac{-1}{\hat{\alpha}(\underline{x})}\sum_{j}^{N_e}\int_{T}^{0}\ddot{\underline{u}}_p^j(\underline{x},t)\cdot\underline{v}_p^j(\underline{x},T-t)dt \tag{4.9}$$

and

$$K_{\hat{\beta}}(\underline{x}) = \frac{1}{\hat{\beta}(\underline{x})}\sum_{j}^{N_e}\int_{T}^{0}\ddot{\underline{u}}_s^j(\underline{x},t)\cdot\underline{v}_s^j(\underline{x},T-t)dt, \tag{4.10}$$

where the vector wavefields $\underline{v}_p$ and $\underline{v}_s$ are calculated by forward propagation using adjoint sources

$$\underline{v}_p^j(\underline{x},T-t) = \left(L^{-1}\right)^{*}\nabla\nabla\cdot\int_{-\underline{H}}^{\underline{H}}\hat{\alpha}(\underline{x})\ddot{\underline{u}}_s^j(\underline{x}+2\underline{h},t)R(\underline{x}+\underline{h},\underline{h})d\underline{h} \tag{4.11}$$

and

$$\underline{v}_s^j(\underline{x},T-t) = \left(L^{-1}\right)^{*}\nabla\times\nabla\times\int_{-\underline{H}}^{\underline{H}}\hat{\beta}(\underline{x})\ddot{\underline{u}}_p^j(\underline{x}-2\underline{h},t)R(\underline{x}-\underline{h},\underline{h})d\underline{h}, \tag{4.12}$$

where $\left(L^{-1}\right)^{*}$ is the adjoint of the inverse of the isotropic elastic wave equation operator (here L^{*} is defined as forward propagation) and $R(\underline{x},\underline{h}) = \underline{h}^2 I(\underline{x},\underline{h})$ (see appendix B.2 for more details).

To reduce computational burden, we replace $\nabla\nabla\cdot$ in equation 4.11 and $\nabla\times\nabla\times$ in equation 4.12 by respective weights a and b (that are obtained from analytic derivation of spatial derivatives), and calculate the adjoint sources as

$$\underline{v}_p^j(\underline{x},T-t) = \left(L^{-1}\right)^{*}a\int_{-\underline{H}}^{\underline{H}}\hat{\alpha}(\underline{x})\ddot{\underline{u}}_s^j(\underline{x}+2\underline{h},t)R(\underline{x}+\underline{h},\underline{h})d\underline{h} \tag{4.13}$$

and

$$\underline{v}_s^j(\underline{x},T-t) = \left(L^{-1}\right)^{*}b\int_{-\underline{H}}^{\underline{H}}\hat{\beta}(\underline{x})\ddot{\underline{u}}_p^j(\underline{x}-2\underline{h},t)R(\underline{x}-\underline{h},\underline{h})d\underline{h}. \tag{4.14}$$

With these gradients of the objective function, we set up the standard gradient-based optimization scheme as

$$\underline{m}_{i+1} = \underline{m}_i + \nu_{i_k}\underline{p}_i, \tag{4.15}$$

where the model parameter $\underline{m} = (\hat{\alpha}\ \hat{\beta})^T$ with $\hat{\alpha}$ and $\hat{\beta}$ sorted into row vectors, $\underline{p}$ is the line search direction column vector and ν is the step length scalar. The superscript T denotes transpose and subscripts i and k refer to the indices of the iteration of the search direction and that of the step length, respectively. The efficient calculation of the step length, ν, for SICP-WEMVA is given in appendix B.3.

The search direction is given by the conjugate gradient method (Hestenes & Stiefel, 1952) as

$$\begin{aligned} \underline{p}_0 &= -C_0\underline{g}_0; \qquad (4.16) \\ \underline{p}_i &= -C_i\underline{g}_i + \eta_i\underline{p}_{i-1}, \qquad (4.17) \end{aligned}$$

where $\underline{g} = (K_{\hat{\alpha}}\ K_{\hat{\beta}})^T$, $K_{\hat{\alpha}}$ and $K_{\hat{\beta}}$ are the gradients found in equations 4.9 and 4.10 and sorted into row vectors, C is a preconditioner (here we use it as a smoothing operator), and scalar η_i is defined as in e.g., Rodi & Mackie (2001) as

$$\eta_i = \frac{\underline{g}_i^T C_i \underline{g}_i}{\underline{g}_{i-1}^T C_{i-1} \underline{g}_{i-1}}. \tag{4.18}$$

4.3.3 Algorithm

Each iteration of the proposed algorithm consists of the following steps:

- Propagate each elastic shot gather, j, backward in time, and store the acceleration wave fields $\underline{\ddot{u}}_p^j(\underline{x}, t)$ and $\underline{\ddot{u}}_s^j(\underline{x}, t)$.
- Construct extended image gathers $I(\underline{x}, \underline{h})$ from all shots using equation 4.6.
- Construct residual extended image gathers: $R(\underline{x}, \underline{h}) = \underline{h}^2 I(\underline{x}, \underline{h})$.
- Calculate $\underline{v}_p^j(\underline{x}, T - t)$ and $\underline{v}_s^j(\underline{x}, T - t)$ for each shot from the stored $\underline{\ddot{u}}_p^j(\underline{x}, t)$, $\underline{\ddot{u}}_s^j(\underline{x}, t)$ and constructed $R(\underline{x}, \underline{h})$.

- Construct the sensitivity kernels $K_{\hat{\alpha}}(\underline{x})$ and $K_{\hat{\beta}}(\underline{x})$ (gradients).

- Update model parameters $\hat{\alpha}(\underline{x})$ and $\hat{\beta}(\underline{x})$ using the gradients (sensitivity kernels).

4.3.4 Practical considerations and implementation

There are three important practical considerations that need to be addressed during the SICP-WEMVA calculation. The first consideration is the smoothing and regularization of the gradients, $K_{\hat{\alpha}}$ and $K_{\hat{\beta}}$. Many studies address the problems associated with the construction and smoothing of the WEMVA gradient (e.g., Shen & Symes, 2008; Fei & Williamson, 2010; Vyas & Tang, 2010; Shen & Simes, 2013). In our study, we regularize the gradients in the so-called vertical time domain (e.g., Alkhalifah et al., 2001; Shabelansky, 2007), which stabilizes and speeds up the convergence. The transformation for vertical time is given by

$$\begin{aligned} K_{\hat{\alpha}}(\underline{x}) &\longrightarrow K_{\hat{\alpha}}(\underline{\tau}^{\alpha}) \\ K_{\hat{\beta}}(\underline{x}) &\longrightarrow K_{\hat{\beta}}(\underline{\tau}^{\beta}), \end{aligned} \tag{4.19}$$

where the vertical times $\underline{\tau}^{\alpha}$ and $\underline{\tau}^{\beta}$ are defined as

$$\underline{\tau}^{\alpha} = (\tau_x^{\alpha}, \tau_y^{\alpha}, \tau_z^{\alpha}) = \int_0^{\underline{x}} \frac{d\underline{\xi}}{\alpha} \quad \text{and} \quad \underline{\tau}^{\beta} = (\tau_x^{\beta}, \tau_y^{\beta}, \tau_z^{\beta}) = \int_0^{\underline{x}} \frac{d\underline{\xi}}{\beta}.$$

The second consideration is the presence of the surface waves in the data and the excitation of false body-wave modes during the back propagation. The back-propagation of the surface waves may contaminate the image in the shallow part, as they cannot be separated into purely P and S waves. The false modes are generated due to the imperfect acquisition geometry, and become less severe with dense receiver coverage. Nevertheless, this effect is observable and will be addressed and illustrated below. To alleviate both of these effects and stabilize the optimization procedure, we apply muting in the space-lag domain. However, more sophisticated approaches may be beneficial.

The third practical consideration is related to the propagation of the adjoint P- and S-wave sources (equations 4.13 and 4.14). In the 2D examples below we propagate both sources simultaneously using only one propagation where the P-wavefield propagates in the P-SV plane and the S-wavefield propagates in the SH plane. This propagation is possible in 2D as the wavefields are completely decoupled in 2D. In 3D, however, each adjoint source wavefield needs to be propagated separately.

4.4 Numerical tests

To examine the proposed algorithm we test it with two data sets: a synthetic data set and a field data set from the passive source micro-seismic monitoring of a geothermal area in Iceland. The acquisition geometry is transmission for both tests, i.e., the recording stations are placed on the surface and sources are located at depth (some earthquakes in the field data occurred outside of the imaging/computational region). All elastic wave solutions are modeled with a 2D finite-difference solver, using a second order in time staggered-grid pseudo-spectral method with perfectly matched layer (PML) absorbing boundary conditions (details are shown in appendix A).

4.4.1 Synthetic test

We test SICP-WEMVA with a synthetic S-wave speed model, shown in Figure 4-5, and constant P-wave speed and density of 4500 m/s and 2500 kg/m^3, respectively. The number of grid points in the model is $N_z = 150$ and $N_x = 200$, and the spatial increments are $\Delta x = \Delta z = 20$ m. We generate 35 isotropic (explosive) sources equally distributed at 1.8 km depth with horizontal increment of 100 m using a Ricker wavelet with a peak frequency of 45 Hz and Δt of 0.001 s. The data are recorded with two-component receivers that are equally distributed and span the same computational grid at a depth of 0 km (i.e., $\underline{x}_{obs} = (x, 0)$ km). Figures 4-6(a) and 4-6(b) show representative common shot gathers for Z and X components, $u_z(\underline{x}_{obs}, t)$ and $u_x(\underline{x}_{obs}, t)$, from a source at $(x, z) = (2.0, 1.8)$ km. In Figure 4-6(c), we also present the (scalar) P-component of the seismic shot gather, calculated by

$\nabla \cdot \underline{u}(\underline{x}_{obs}, t)$, to support the assumption made in equation B.19 (appendix B.2) that the P-wavefield is barely affected by a contrast in the S-wave speed, evidenced by the lack of energy arriving after the direct P arrival.

Having calculated the elastic seismic data (Figure 4-6), we test SICP-WEMVA with the smoothed background S-wave speed model, shown in Figure 4-7(a) (i.e., elliptical velocity inclusions were omitted). In Figure 4-7(b) we show the S wave model after five iterations. We observe that the smooth part of the true velocity model is reconstructed. To compare the effect of the inverted velocity model on imaging, we calculate the converted-phase images using the true, initial and inverted S-wave speeds, along with the smoothed true S-wave speed. In Figure 4-8(c) we observe that the migrated image obtained using the inverted model shows significant improvement and gradual convergence toward the true image compared to that obtained with the initial model (Figure 4-8(b)). We show the space-lag image gathers for the image point at $x_f = 2$ km in Figures 4-9 and 4-10. The strong energy extending linearly in depth (marked with green arrows in Figure 4-9) corresponds to the energy introduced by the false wave-modes. In Figure 4-10, we show the same gathers after zooming in and muting the false wave-modes. Note that SICP-WEMVA was applied to the muted gathers. We observe that although some energy remains at the non zero-lags, the energy is more focused around zero lags in the gather calculated with the inverted model compared to that obtained with the initial S-wave speed.

The resolution of the velocity reconstruction depends on the sufficient sampling of the medium by both P and converted-phase S (or/and S and converted-phase P) back propagated wavefields (i.e., illumination) and is directly related to the imaging resolution through data frequency content and receiver aperture. An analytic imaging resolution analysis for comparison between the PP and PS imaging was conducted in Xiao & Leaney (2010). This comparison highlighted the superiority of the spatial resolution for PS over the PP imaging.

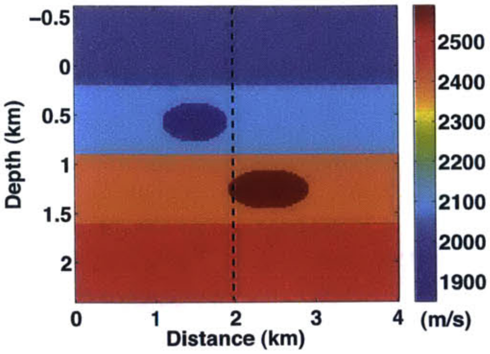

Figure 4-5: True S-wave speed used in the synthetic test. The dashed vertical line refers to the location of the CIG gathers, x_f, shown in Figures 4-6, 4-9 and 4-10.

4.4.2 Field data example

The second example uses passive source, micro-seismic field data from a geothermal area in a region of Iceland that has abundant natural and induced seismicity (see Figure 4-11(a)). We test SICP-WEMVA with four stations (SAN, IND, BIT and TRH) along a 2D line at the latitude of 64.06° and longitudes between -21.6° and -21.10°. In Figures 4-11(b) and 4-11(c), we show four representative traces sorted into a common shot gather (Z-component) from a single earthquake. Each trace is of a time record of $T = 12$ s and $\Delta t = 0.005$ s that was band-pass filtered between 2 and 12 Hz. The relative position of the traces in the common shot gather corresponds to the relative locations of the stations at the surface, $\underline{x}_{obs} = (x, z_{surface} = 0 \text{ km})$. The computational grid is $N_z = 90$ and $N_x = 300$ and the spatial increments are $\Delta z = 0.2$ km and $\Delta x = 0.15$ km. To construct an image (using equation 4.5) of the geothermal area that is located between longitudes -21.4° and -21.2°, we use 32 events (i.e., earthquakes) of moment magnitude between 0.9 and 1.2. Initial P- and S-wave speeds were taken from the model of Tryggvason et al. (2002) obtained using regional-scale travel-time tomography. These velocity models are shown in Figures 4-12(a) and 4-12(b), along with the SICP image in Figure 4-12(c). Note that the shallow part of the SICP image is completely contaminated by aliasing caused by the sparse station distribution on the surface and thus is muted out. By applying the SICP-WEMVA optimization for the deep part of the earth (between 2.5 and 10 km),

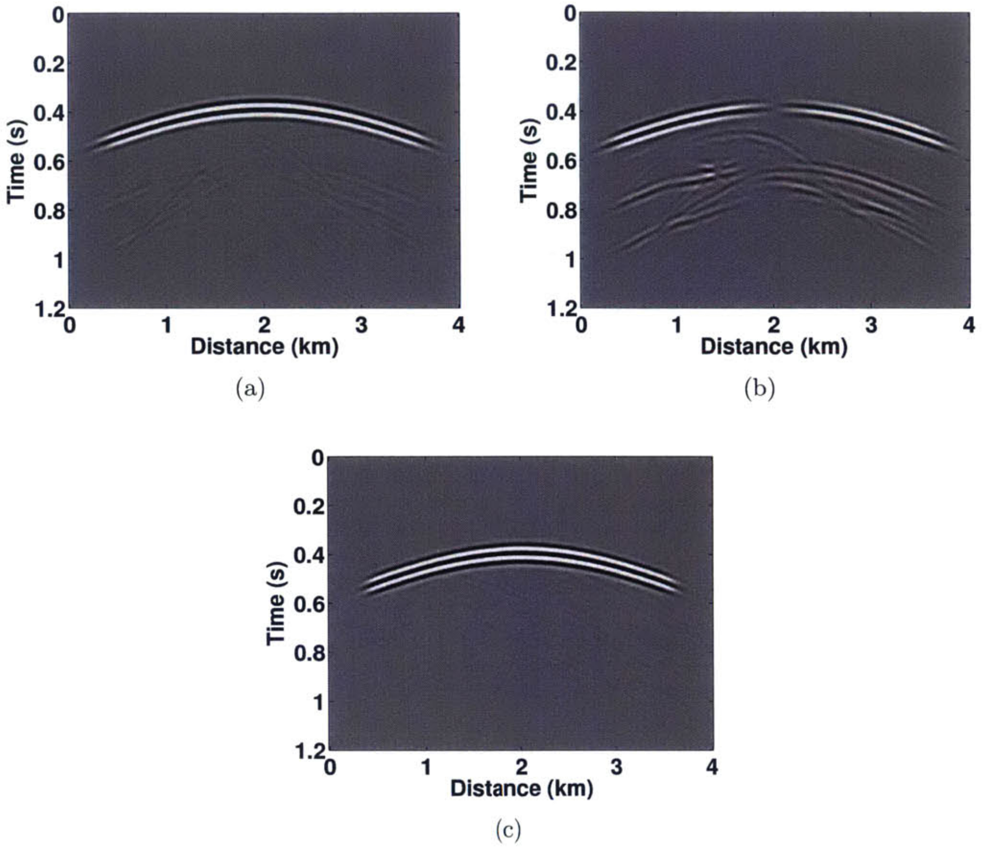

(a) (b) (c)

Figure 4-6: Common shot gathers calculated at the depth of 0 km due to an isotropic source from (x, z) = (2.0,1.8) km: (a) Z-component, $u_z(x, t)$; (b) X-component, $u_x(x, t)$; (c) P-component calculated during the propagation as $\nabla \cdot u$, shown to support the assumption made in equation B.19 (appendix B.2) that the P-wavefield is barely affected by a contrast in the S-wave speed, evidenced by the weak energy arriving at the times after the direct P-wave arrivals.

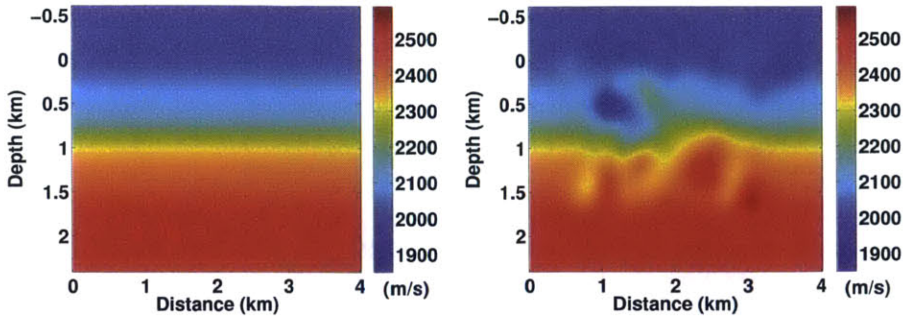

(a) (b)

Figure 4-7: S-wave speed models: (a) initial, and (b) after 5 iterations of SICP-WEMVA. The smooth part of the true velocity model (Figure 4-5) is reconstructed in the inferred model.

we update the P- and S-velocity models (Figures 4-12(d) and 4-12(e)) and the SICP image (Figure 4-12(f)). We use 27 iterations of conjugate gradient for updating the velocity models (see the convergence curve in Figure 4-13(a)). We observe that in the area of the reservoir (longitudes between -21.38° and -21.22°) the P-wave velocity has slightly increased while the S-wave velocity decreased along vertical trends. Although this result indicates a high Vp/Vs and may suggest magma conduits, more study is needed to understand the geologic implications of this result. The image produced with the updated velocities (in Figure 4-12(f)) shows more focused structure and reveals previously obscured structure (e.g., the region within the marked red ellipse). We also show in Figure 4-13(b) the subsurface space-lag gather along the x-direction, h_x, at longitude of -21.34°, where we observe that the energy in the updated gather is more focused around zero space-lag than that obtained with the initial models. These gathers, along with the convergence curve, suggest that the SICP-WEMVA optimization converges toward a reasonable solution.

4.5 Discussion

In this section we address the most pressing assumptions underlying SICP-WEMVA and discuss their implications for the accuracy, stability, robustness and applicability

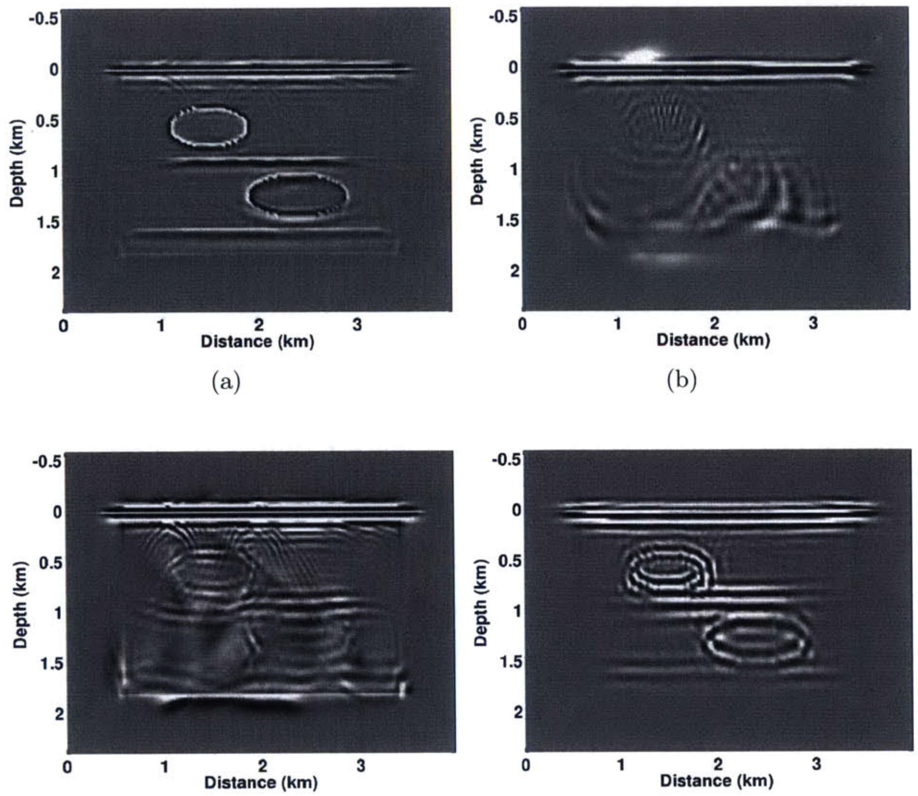

(a) (b)

(c) (d)

Figure 4-8: Results of the source-independent converted-phase elastic seismic imaging (SICP-IC) obtained with: (a) true, (b) initial, and (c) inferred S-wave speeds that are shown in Figures 4-5 and 4-7. (d) SICP image obtained with the smoothed true S-wave velocity model to show the resolution of the expected image reconstruction with SICP-WEMVA. P-wave speed and density are constant, 4500 m/s and 2500 kg/m^3, respectively.

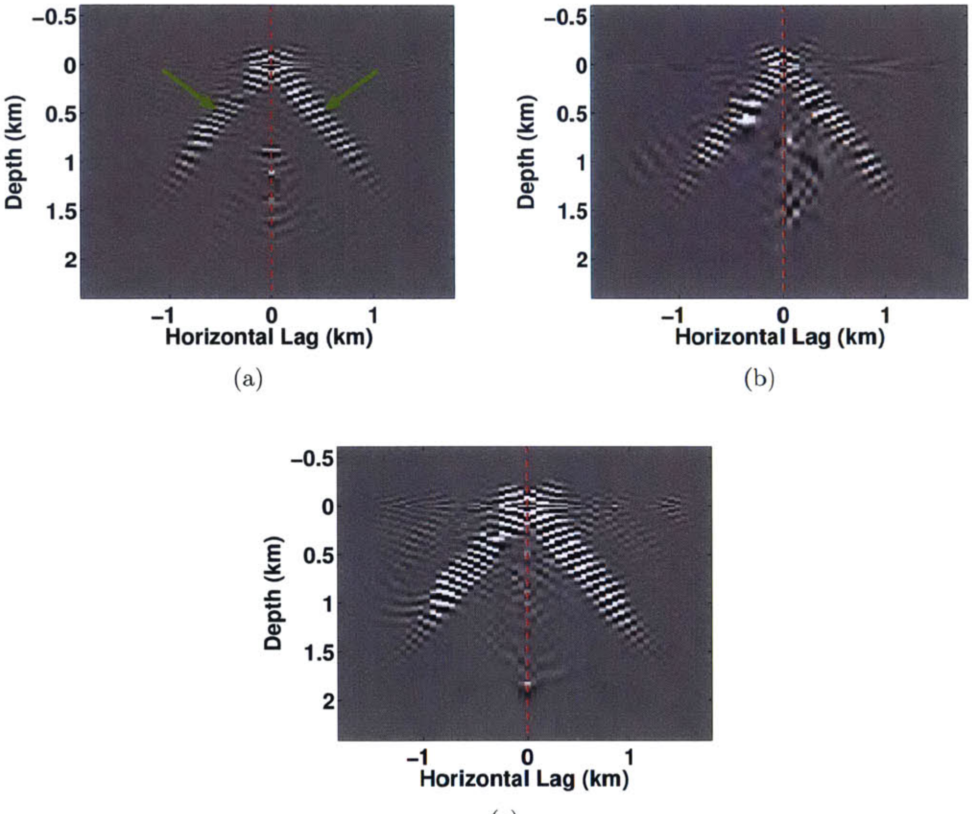

(a)

(b)

(c)

Figure 4-9: Converted-phase space-lag common image gathers with the (a) true, (b) initial, and (c) inverted S-wave speed model. The strong energy linearly extended in depth, marked with green arrows in (a), corresponds to the false wave-mode oscillation.

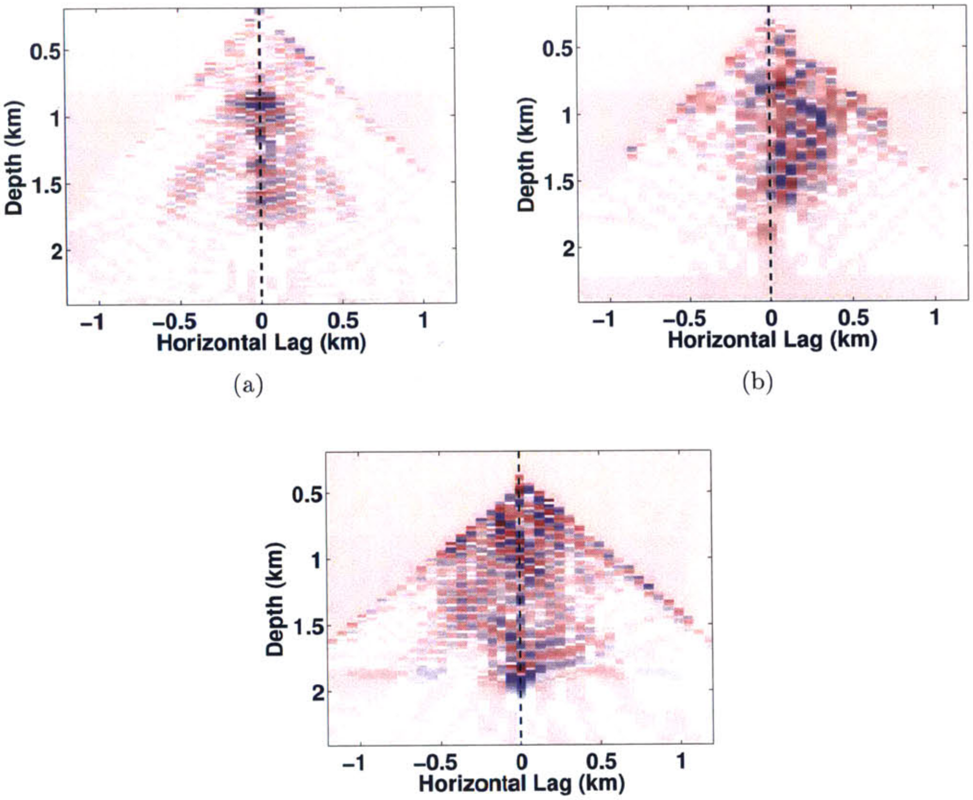

(a) (b) (c)

Figure 4-10: Converted-phase space-lag common image gathers (CIGs) from Figure 4-9 shown in different color after the false wave mode energy was muted out and the horizontal axis was zoomed in. The CIGs are obtained with (a) true, (b) initial, and (c) inverted S-wave speed model after five iterations of SICP-WEMVA. The input for SICP-WEMVA is the residual image gathers after the false wave-mode energy has been muted out. Note that although some energy remains at the non zero-lags, the energy is more focused around the zero lags (black vertical dashed line) in the gather after the five iterations of SICP-WEMVA.

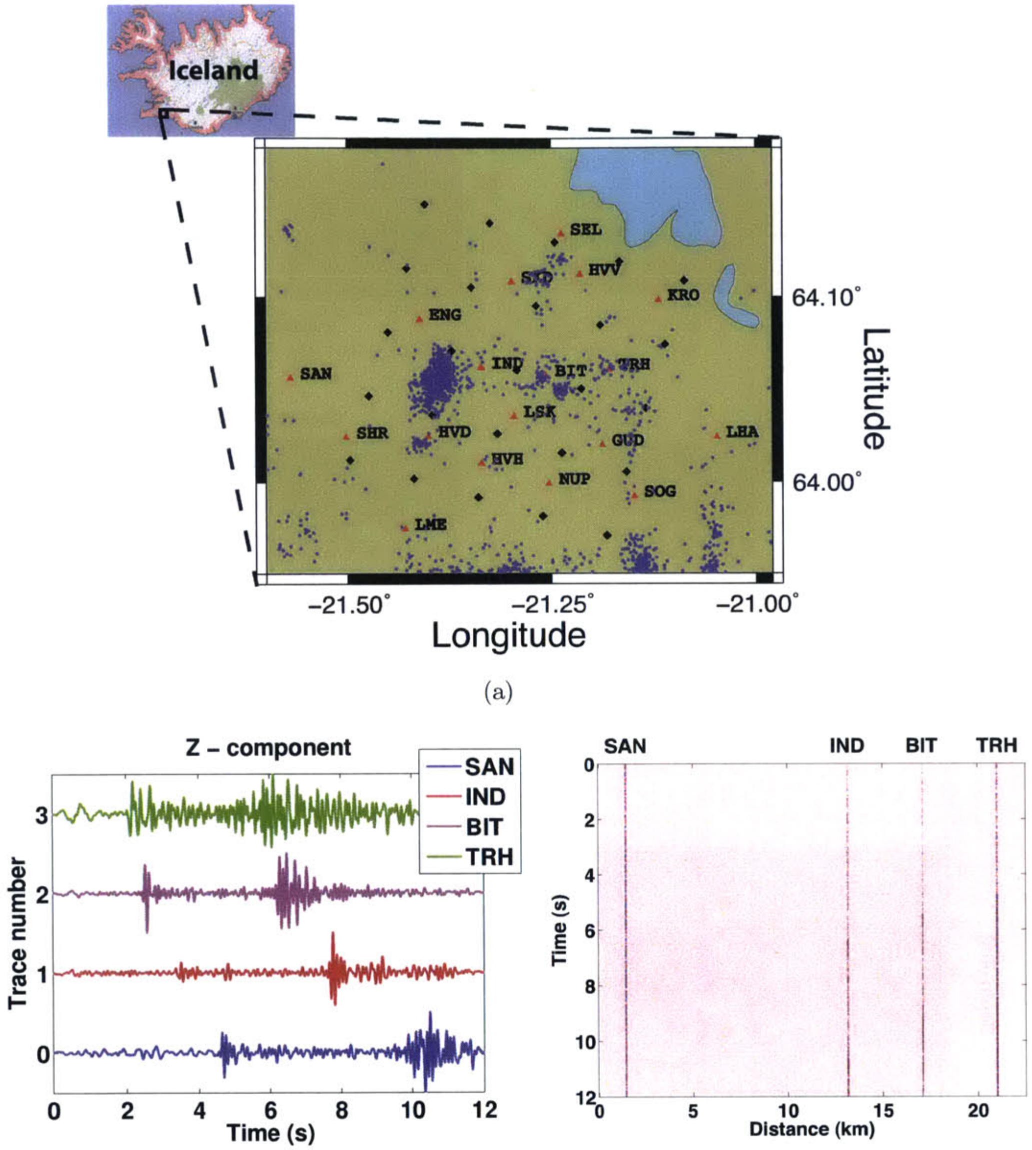

(a)

(b)

(c)

Figure 4-11: (a) Map of the investigated area in Iceland with micro-seismic field data. The blue dots mark the earthquake locations projected onto the surface, the red triangles refer to locations of the recording stations named with three letters, and the black diamonds denote the computational grid points of the regional travel time tomography done by Tryggvason et al. (2002). (b) Representative normalized and filtered Z-component traces that are recorded at the surface along a 2D line at the latitude of 64.06° and sorted into (c) a common shot gather. The relative position of the traces in the common shot gather corresponds to the relative position of their stations on the surface; the trace #0 from station SAN in (b) is the leftmost trace in (c).

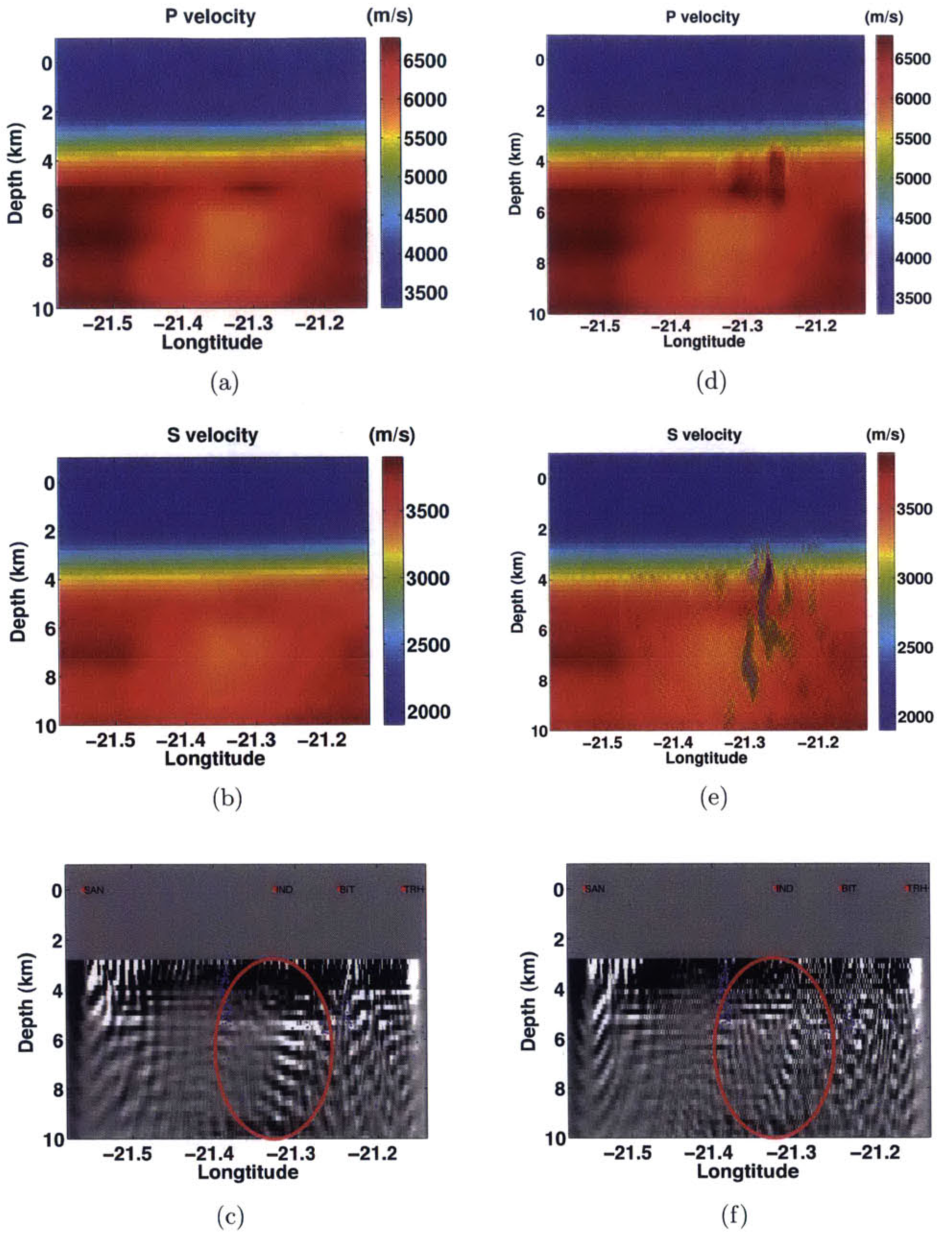

(a) (d)

(b) (e)

(c) (f)

Figure 4-12: Left: the initial (a) P-wave speed, (b) S-wave speed and (c) SICP image obtained with the P- and S-wave speeds from (a) and (b). Right: the results of SICP-WEMVA after 27 iterations (d) P-wave speed, (e) S-wave speed and (f) SICP image obtained with the P- and S-wave speeds from (d) and (e). The blue dots in (c) and (f) mark the location of natural and induced micro-seismic events and the red ellipse highlights the region where the structure has improved. The shallow part of the images are contaminated due to sparse station distribution and thus were muted. The horizontal axis corresponds to distance of 22 km (i.e., exaggerated by 2.2 times in comparison to the vertical depth axis).

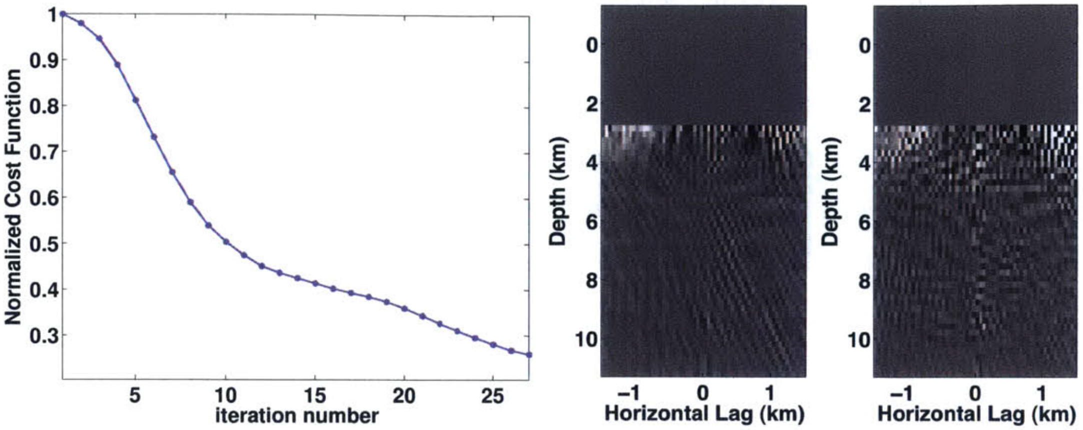

(a)

(b)

Figure 4-13: (a) Convergence curve for SICP-WEMVA. (b) Converted phase subsurface space-lag CIG with initial and updated velocity models shown in Figure 4-12.

of the method.

First, SICP-WEMVA is derived based on the assumption of an isotropic medium in which the total acceleration wavefield is decomposed into the P- and S-wavefield components. Although the wavefield separation can be achieved in certain anisotropic cases (e.g., Yan, 2010; Zhang & McMechan, 2010; Yan & Sava, 2011) for imaging purposes, additional mathematic effort is needed to derive the sensitivity kernel to update the velocity model for the anisotropic medium. Note however, that there are studies for reflection type source-dependent anisotropic WEMVA (e.g., Li et al., 2012; Li, 2013; Weibull & Arntsen, 2013) that could potentially be applied to the source-independent converted-wave case constructed here.

The second assumption is related to the differential semblance operator (equation 4.7) for the residual image, which is defined as a multiplication of the extended image by $\underline{h}$. Although this operator is very intuitive and was derived in Shen & Symes (2008) from the derivative operator that measures the flatness of the seismic energy in the angle domain CIG, it has been recognized that a more sophisticated operator is required for better focusing of the energy at zero subsurface space-lag and reducing noise at large lags (e.g., Shan & Wang, 2013; Weibull & Arntsen, 2013).

The third consideration addresses the source illumination or number of sources required to focus the energy around zero space-lag, even with the true velocity model. It is known that for reflection type WEMVA (and CP-WEMVA), many sources are required to obtain focusing. For transmission SICP-WEMVA, in contrast, the number of sources could be smaller (see Figure 4-3(d)) because of the low frequency content in the data due to the presence of the direct waves. The comparison between WEMVA/CP-WEMVA and SICP-WEMVA will be discussed elsewhere.

The fourth and last issue is the applicability of the SICP-WEMVA to different types of seismic data: active source surface-seismic and VSP, and passive tele-seismic data. For surface-seismic data, where the converted-phase signal in the data is generally of a reflection type for both P- and (converted) S-waves, reflection SICP-WEMVA may have similar limitations with source illumination and frequency content as the standard reflection WEMVA/CP-WEMVA, as discussed above. For VSP studies, SICP-WEMVA may have limitations with the illumination due to the geometry of the monitoring wells, and it depends on the wave types that are recorded: reflection, transmission or both types simultaneously. The use of both wave types simultaneously might produce images and velocity models with improved resolution from SICP-WEMVA but may also introduce additional complexities. For tele-seismic data, the separation of different body-wave phases should be clearer than with micro-seismic data, shown in this study, and should produce clear large-scale images and velocity models, but may be restricted by the high amplitude surface waves in the record and thus would require procedures for windowing out the surface-waves before using body-wave information in the SICP-WEMVA. However, SICP-WEMVA does not require source information, thus it does not distinguish between different types of data and acquisitions, and can be applied similarly to each data set as long as converted-phase waves are present in the signal. Nevertheless, more research needs to be conducted to better understand the method's performance on each individual data type.

4.6 Conclusion

We have developed a fully automatic, data-driven optimization method for velocity update using converted phase waves. We presented a converted-phase imaging condition in the extended space-lag domain for the objective functional. We derived a gradient-based iterative optimization method based on this objective functional and tested the method using a synthetic model and field micro-seismic data. The results show the applicability of the method in particular to micro-seismic applications where source information is not directly available. This opens up the possibility for source-independent full-wavefield velocity analysis, a methodology that previously was not available, thus considerably improving the quality of velocity analysis and reducing the computational and processing cost.

4.7 Acknowledgments

We thank ConocoPhillips and the ERL founding members consortium at MIT for funding this work. We acknowledge Xinding Fang, Yingcai Zheng and Sudhish Kumar Bakku for helpful discussions. We also acknowledge Ari Tryggvason and Olafur Gudmundsson from Uppsala University for providing velocity models and for collaboration with collecting the micro-seismic data.

Chapter 5

Source Independent Converted-Phase Full Wavefield 2D and 3D Seismic Imaging of the Hengill Geothermal Area, Southwest Iceland[1]

5.1 Summary

The abundance of seismic activity in the Hengill geothermal area in Iceland is a valuable source of information. In this chapter, we use this seismic information to construct 2D and 3D images of medium discontinues with the so-called full wavefield source-independent converted-phase reverse time migration method. This method is based on three simultaneous steps: propagation of the full waveform recordings from stations backward in time using a fully elastic wave simulator; separation of the P and converted-phase S (and/or S- and converted phase P) waves; and applying an imaging condition by cross-correlation. This method requires no source information

---

[1] Shabelansky, A.H., Fehler, M.C., and Malcolm, A.E., AGU 46th Fall Meeting, San Francisco 2013.

so a large source of uncertainty is removed. Although the sparse station distribution produces aliased images at shallow depths, the deeper parts are well-imaged. The application of the method to seismic data produces images that are well correlated with previous seismic and resistivity studies. In particular, the amplitudes of the images are well correlated with a low resistivity region of the geothermal area. The reason for this correlation is not fully understood, but may provide an additional tool for the Hengill site investigation.

5.2 Introduction

The Hengill geothermal region is one of the biggest geothermal areas in Iceland with a size of over 100 km^2 that has been exploited for last several decades for hot water production and electricity generation at Nesjavellir and (since 2006 at) Hellisheidi geothermal power plants (Hardarson et al., 2010). The region lies at the triple junction formed by the Reykjanes peninsula (RP), South Iceland Seismic Zone (SISZ) and the Western Volcanic Zone (WVZ), and has three main volcanic centers: Hengill (He), Hromundartindur (Hr) and Grensdalur (Gr)(see Figures 5-1 and 5-2(a)) (e.g., Miller et al., 1998; Árnason et al., 2010). The area connecting these three centers is characterized by high temperature (300°-310°C) with a large number of hot springs and is known as Olkelduhals (Foulger & Toomey, 1989). The Hengill region was extensively studied using surface and borehole acquisitions with active and passive seismic along with GPS, InSAR, TEM, MT, DC resistivity methods over the past five decades (e.g., Foulger, 1988a,b; Foulger & Julian, 1993; Menke et al., 1994; Evans et al., 1996; Julian & Foulger, 1996; Tryggvason et al., 2002; Wanjohi, 2007; Gunnlaugsson & Gíslason, 2005; Árnason et al., 2010; Franzson et al., 2010; Jousset et al., 2011; Batir et al., 2012; Haraldsdóttir et al., 2012; Zakharova & Spichak, 2012). Different physical characteristics of the Hengill volcano system have been discussed including permeability, temperature, pressure, seismic anisotropy, and stress orientation. Seismic activity in the Hengill area is abundant (see Figure 5-2(b) for earthquakes for a period between 1991 and 2001 and Figure 5-3 between July 2009 and October 2011), and many studies have been conducted to investigate the existence of magma chambers and supercritical fluids, and to delineate the brittle-ductile zones and elastic wave-speed structure (e.g., Foulger & Julian, 1993; Miller et al., 1998; Tryggvason et al., 2002). To our knowledge, all seismic studies of the Hengill region rely on first-arrival travel times and their picking (i.e. acoustic emission, travel time tomography) (e.g., Menke et al., 1994; Tryggvason et al., 2002; Jousset et al., 2011). Non of these works use the full seismic waveform and thus produce results of a limited spatial resolution. Using the entire waveform should improve the resolution of these studies by utilizing more information from each recorded signal.

In this chapter, we investigate the subsurface structure of the Hengill region by producing seismic images using the source-independent converted-phase (SICP) full waveform seismic imaging method (discussed in detail in chapter 2). We compare our results with those obtained by resistivity studies (Árnason et al., 2010) and the interpretation from Miller et al. (1998). The chapter is divided into three parts. In the first part, we review the data acquisition, processing and SICP imaging method. In the second and third parts, we present results of 2D and 3D SICP imaging, correlate them with those obtained from DC resistivity measurements, and discuss the interpretation of the Hengill structure as compared with previous seismic studies.

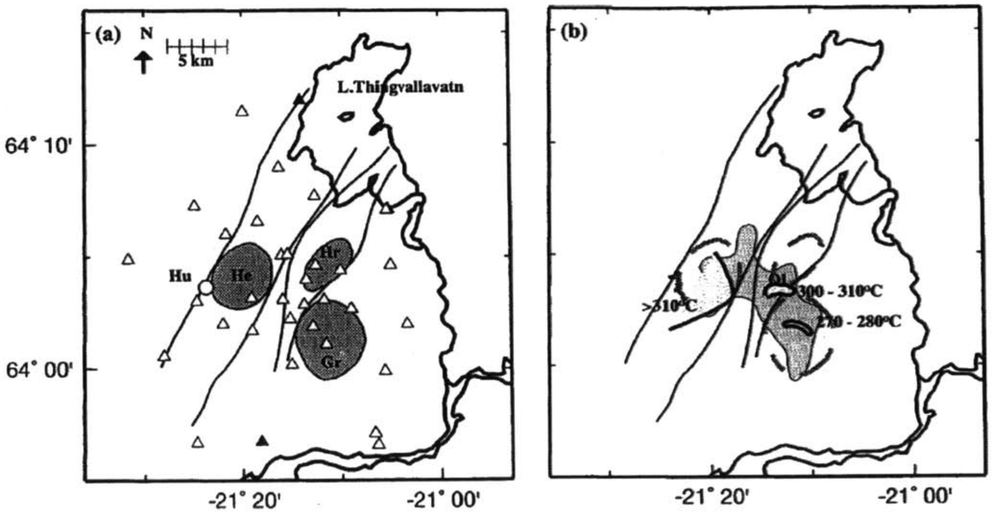

Figure 5-1: Reproduced from Miller et al. (1998): Map of the Hengill geothermal area. (a) Grey shading: the Hengill (He), Hromundartindur (Hr) and Grensdalur (Gr) volcanic centres; thin lines: outlines of the Hengill and Hromundartindur fissure swarms; Hu: the Husmuli basalt shield; open triangles: temporary stations deployed in 1991; filled triangles: stations of the permanent South Iceland Lowland seismic network. (b) Grey shading: Olkelduhals geothermal area. Also indicated are areas where reservoir temperature highs have been determined using fumarole geochemistry.

5.3 Seismic data acquisition and processing

The seismic activity at the Hengill region was monitored between July 2009 and October 2011 with a network of 15 three-component Guralp broadband seismometers with sampling rate of 100 Hz ($\Delta t = 0.01$ s). The stations were distributed about 4 km apart, covering total area of 25x25 km^2 (see Figure 5-3). The earthquake information (i.e, location, GMT time, moment magnitude) was obtained from the Icelandic Meteorological Office for Earthquakes. We identified 32 earthquakes of magnitude between 0.9 and 1.2 (from the extended Hengill area) and extracted 12 s of the signal. The data then were band pass filtered between 2 and 12 Hz (see the representative traces from a single earthquake in Figures 5-4 and 5-5). To satisfy the stability condition of imaging/modeling, we subsample the data to $\Delta t = 0.005$ s (using Sync interpolation). Next, each seismogram was normalized based on its maximum

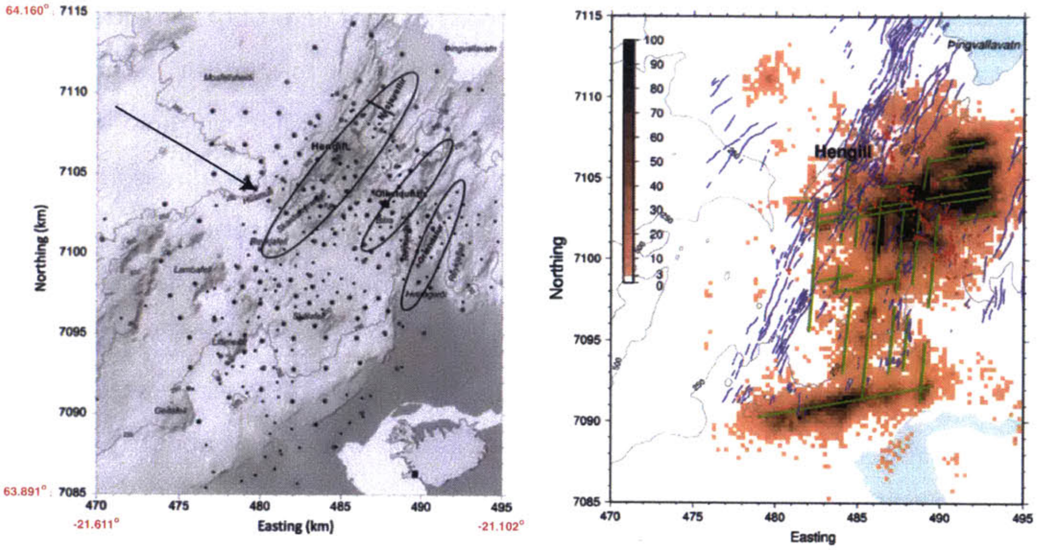

(a) (b)

Figure 5-2: Reproduced from Árnason et al. (2010): (a) Three main volcano centers of the Hengill geothermal area roughly outlined with bold black lines. The Husmuli basalt shield is marked with a black arrow for reference with Figure 5-1. See also the coordinate conversion from UTM to geographic (Longitude-Latitude) system, marked with red color. Locations of TEM and MT soundings marked with small black and big grey dots, respectively. (b) Density of seismic epicenters from 1991 to 2001 and inferred transform tectonic lineaments (green lines).

amplitude (often S-wave) and sorted by source into common shot gathers. The relative position of the traces in the common shot gather corresponds to the relative locations of the stations at the surface, $\underline{x}_{obs} = (x, z_{surface})$ (see Figure 5-6).

The P- and S-wave speed models for imaging were obtained from a previous study by Tryggvason et al. (2002), which span the Hengill region with a 20x20 km^2 horizontal grid extending to 10 km depth with spatial increments of $\Delta x = \Delta y = 5$ km and $\Delta z = 1$ km (see black diamonds in Figure 5-3(a) and yellow dots in Figure 5-7). We mapped the Tryggvason et al. (2002) wave speed models onto our desired computational grid by interpolating these models and fitting them to a grid with increments of $(\Delta x, \Delta y, \Delta z)$ = (0.121,0.144,0.2) km. In Figures 5-8 and 5-9, we show the depth slices of the P-wave speed, α, and the P- to S-wave speed ratio, α/β, used for imaging. In addition to these models, we also extracted a single vertical depth stencil, chosen at (Lon.,Lat.) = (-21.48°,64.06°) and extrapolated it to construct regional-scale layered models for α and α/β. The reason for such a construction stems from the need to verify the sensitivity of the imaging to changes in the wave speed models, particularly to regions of low α and α/β such as that centered at about (Lon.,Lat.) = (-21.26°,64.06°).

5.4 Methodology for source-independent converted-phase seismic imaging

For the seismic imaging of the Hengill geothermal area, we use the source-independent converted phase imaging methodology given in detail in chapter 2. The main idea behind this imaging method is to take an entire seismic record and propagate it backward in time using an elastic wave simulator. During the back-propagation, we decompose the (vector) wavefield into P- and S-components and apply the zero lag in time cross-correlation imaging condition between these two wavefields. The formal form is:

$$I(\underline{x}) = \sum_{j}^{N_e} \int_{T}^{0} \ddot{\underline{u}}_p^j(\underline{x}, t) \cdot \ddot{\underline{u}}_s^j(\underline{x}, t) dt, \qquad (5.1)$$

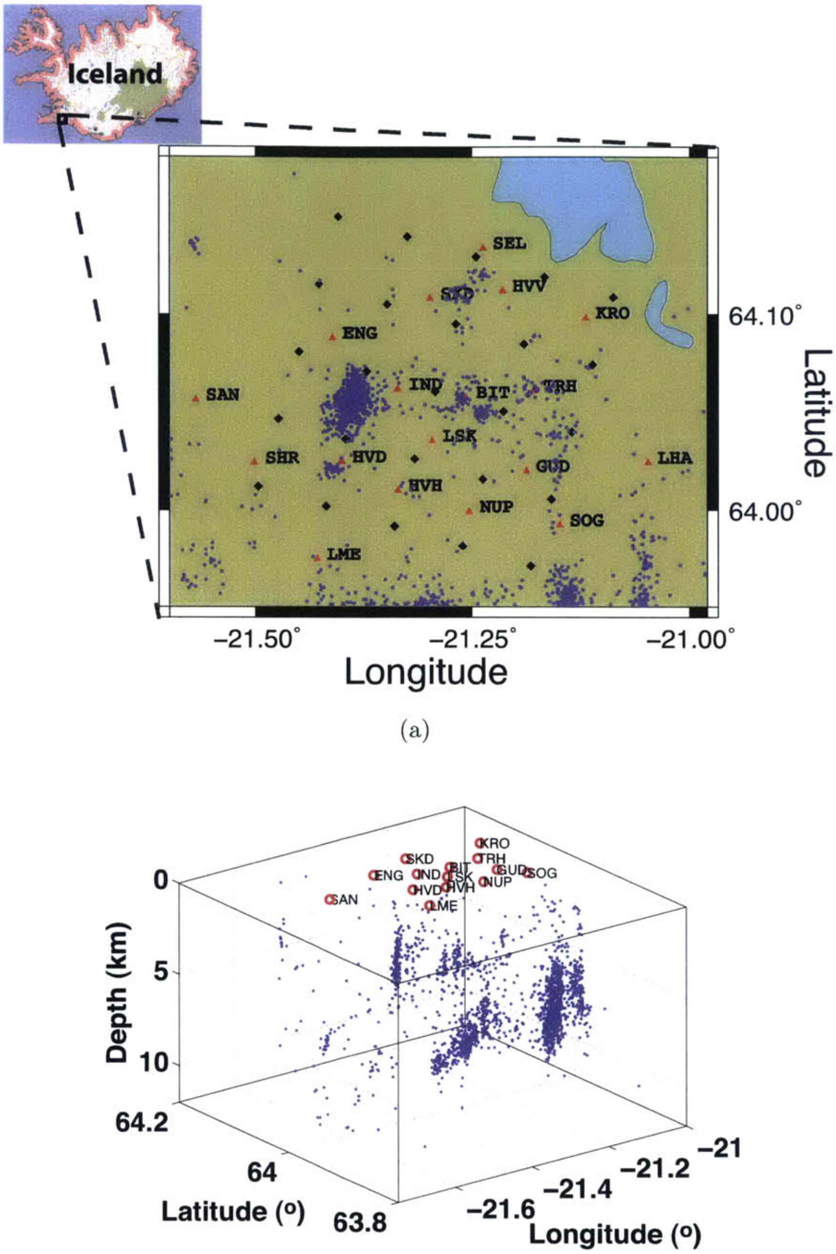

(a)

(b)

Figure 5-3: (a) The geography of the Hengill geothermal area. The red triangles mark the station locations, marked by three letters, the blue dots mark the seismic events (between July 2009 and October 2011), and the black diamonds the points where the P- and S-wave speed models were estimated by the travel time tomography study of Tryggvason et al. (2002). (b) 3D cube showing micro-seismic event relocations (blue dots). The red circles on the surface mark the location of the stations.

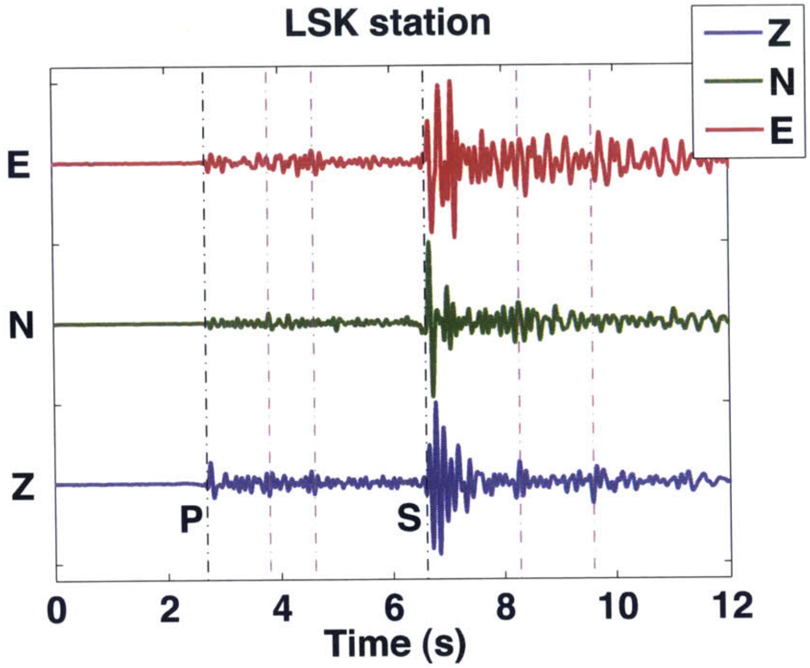

Figure 5-4: Representative particle-velocity three-component (Z-depth, N-north, E-east) seismograms (for the station LSK) showing direct P- and S-wave arrivals (black dot-dashed vertical lines) and those for potential converted-phase waves (blue dot-dashed vertical lines). The traces were band-pass filtered between 2 and 12 Hz.

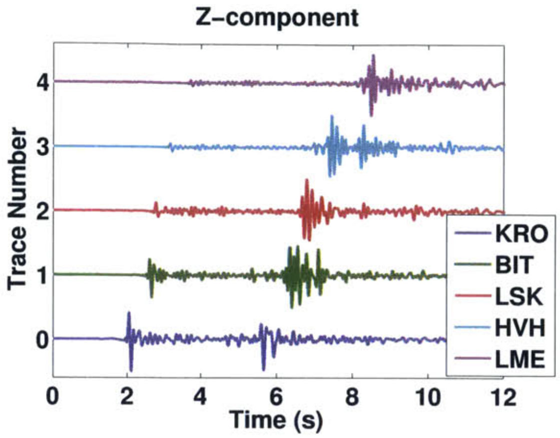

(a)

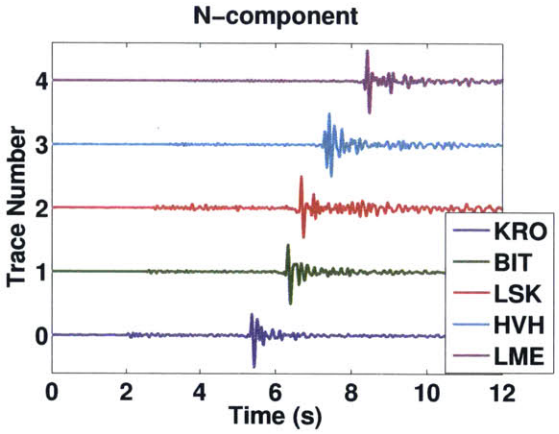

(b)

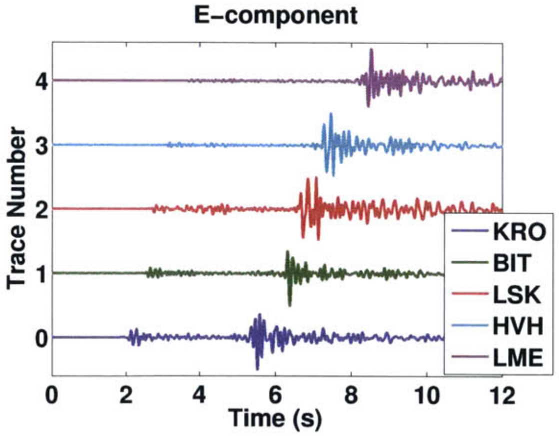

(c)

Figure 5-5: Representative traces of particle velocity from an earthquake of moment magnitude 1.1 recorded along 2D line with stations LME, HVH, LSK, BIT, and KRO. Traces were band-pass filtered between 2 and 12 Hz.

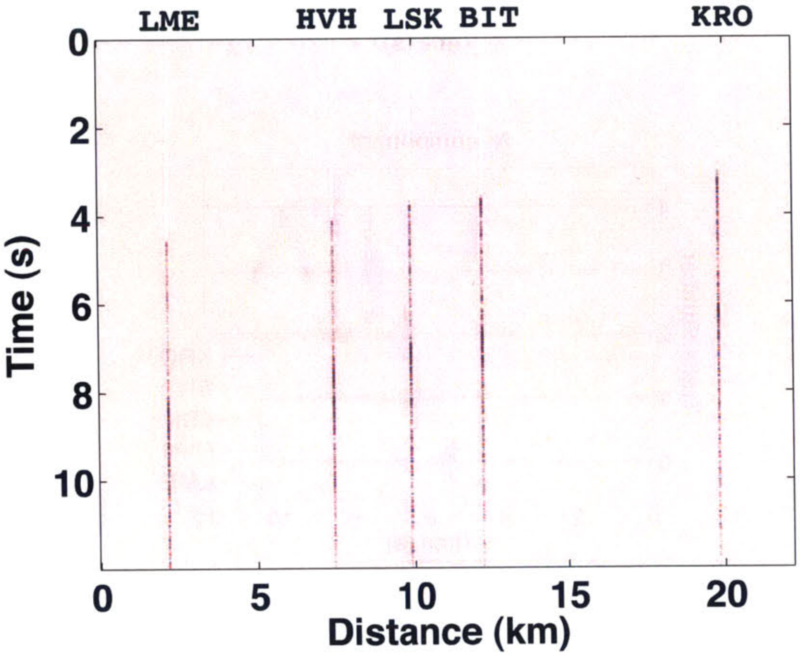

Figure 5-6: Representative Z-component traces from Figure 5-5(a) sorted into a common shot gather along a 2D line containing stations LME, HVH, LSK, BIT and KRO. The relative position of the traces in the gather corresponds to the relative location of the stations at the surface (see Figure 5-3(a)).

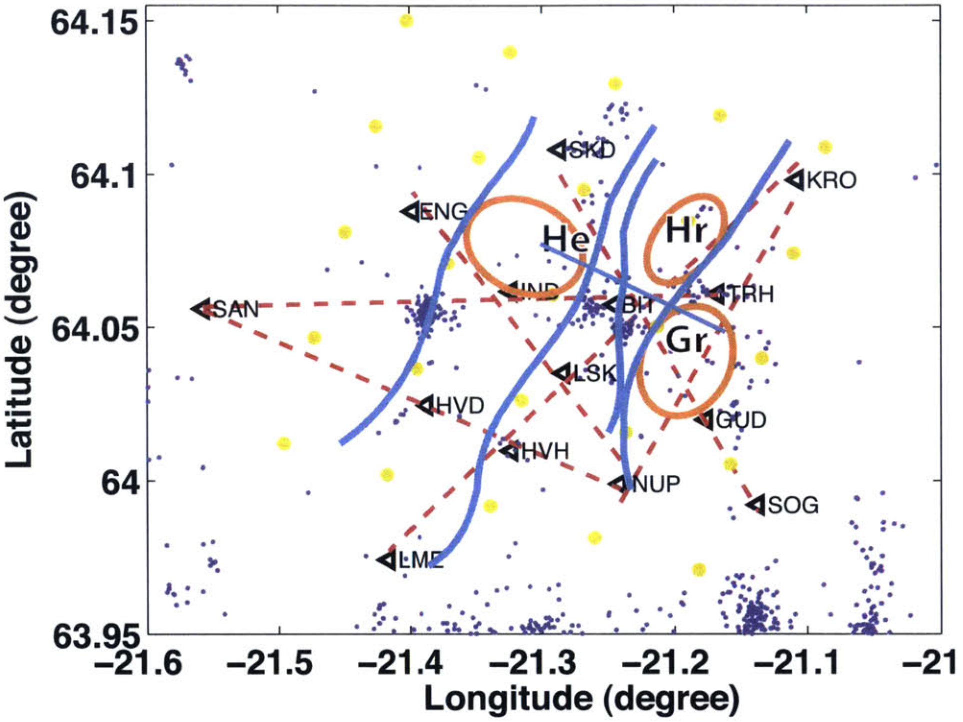

Figure 5-7: Geographic map of seismic stations (black triangles) monitoring seismic activity (blue dots) of the Hengill geothermal area. The orange ellipses mark the volcano centers: Hengill (He), Hromundartindur (Hr) and Grensdalur (Gr), and the cyan lines mark the orientation and patterns of fissure swarms, all placed here based on the study of Miller et al. (1998). The dashed red lines mark projections of the 2D SICP images formed in this study using the P- and S-wave speed models that were interpolated and extracted from a previous 3D study (Tryggvason et al., 2002) at the computational grid points on the surface denoted by yellow dots.

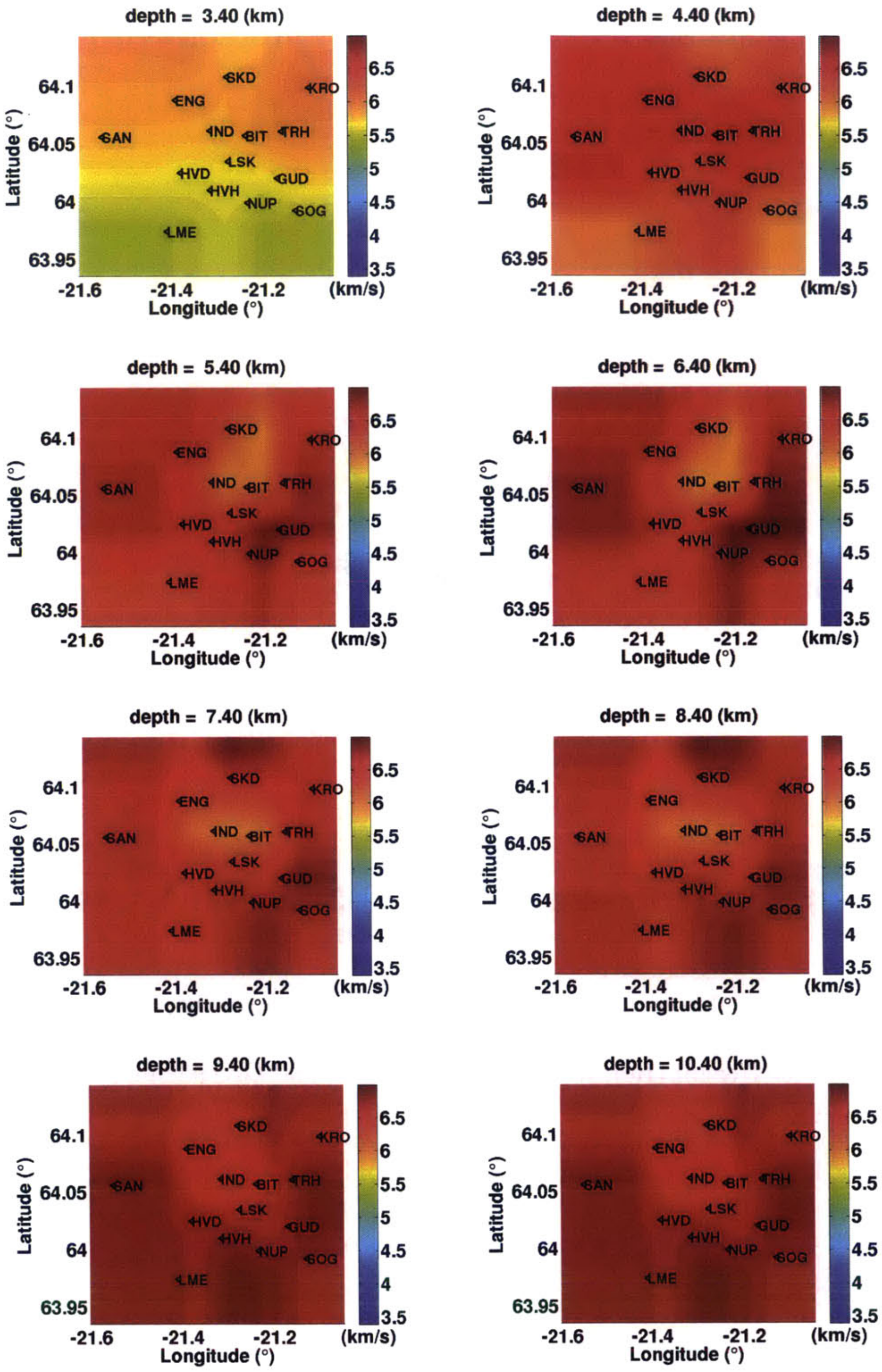

Figure 5-8: Depth slices of 3D P-wave speed, α, from Tryggvason et al. (2002) adapted to the computational grid used for SICP imaging.

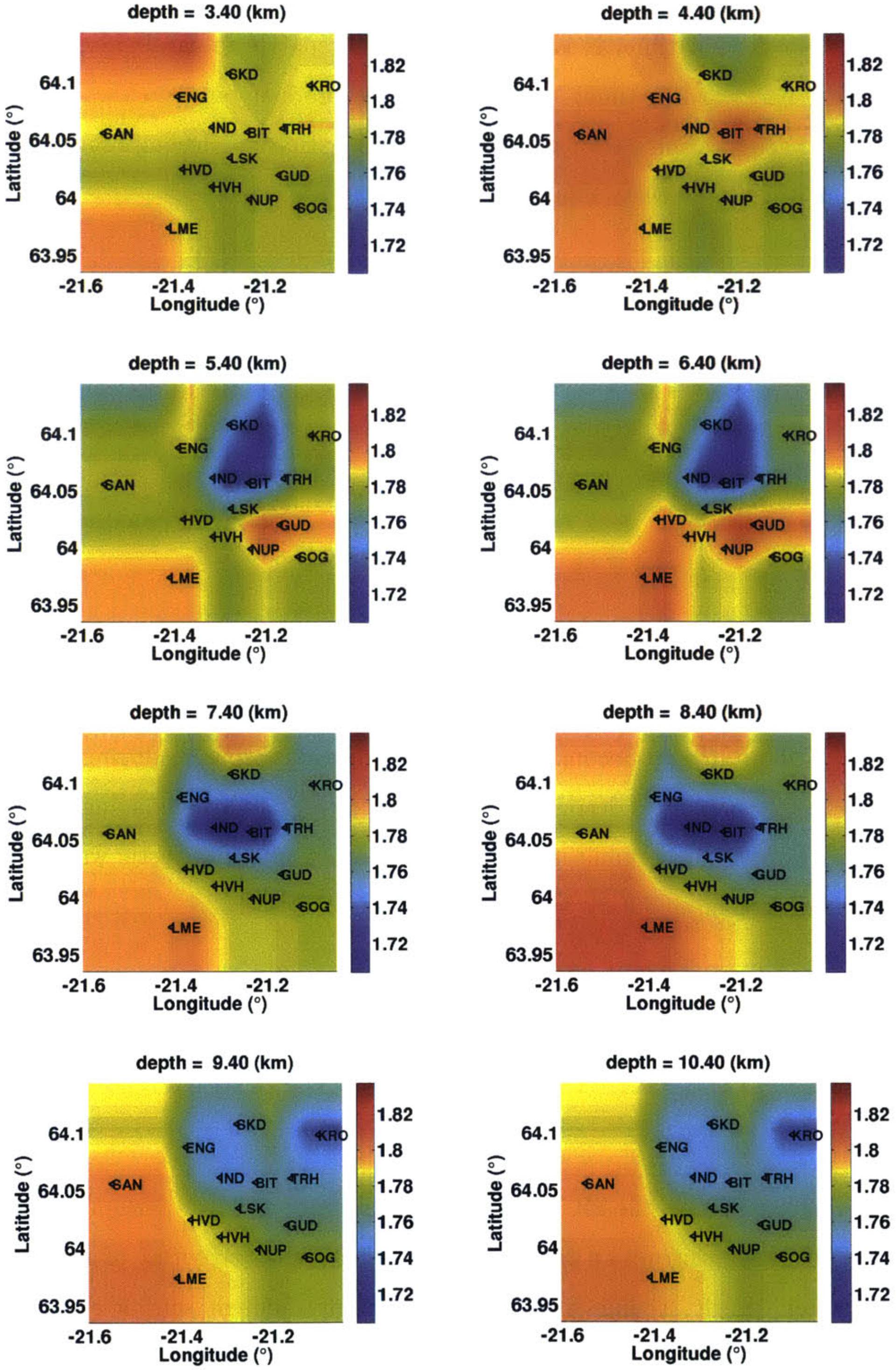

Figure 5-9: Depth slices of 3D α/β from Tryggvason et al. (2002) adapted to the computational grid used for SICP imaging.

where $\underline{x}$ and t are the space (vector) and time coordinates, respectively, and T is the maximum recorded time; it is at the lower limit of the integral (i.e., the data is propagated backward in time). The $\cdot$ is the dot product between the P- and S- components of acceleration vector wavefields $\underline{\ddot{u}}_p$ and $\underline{\ddot{u}}_s$ that are decomposed from the isotropic, smooth, elastic wave equation as

$$\underline{\ddot{u}}_p = \alpha^2 \nabla\nabla \cdot \underline{u} \qquad\qquad \underline{\ddot{u}}_s = -\beta^2 \nabla \times \nabla \times \underline{u},$$

where ∇, $\nabla\cdot$ and $\nabla\times$ are the gradient, divergence and curl, respectively, $\underline{u}(\underline{x}, t)$ is the displacement vector wavefield and $\alpha(\underline{x})$ and $\beta(\underline{x})$ are the P- and S- wave speeds. To remove the effect of velocity on imaging, we use:

$$\underline{\ddot{u}}_p = \nabla\nabla \cdot \underline{u} \qquad\qquad \underline{\ddot{u}}_s = -\nabla \times \nabla \times \underline{u}. \tag{5.2}$$

The reason for using this imaging condition stems from three important advantages. First, no source information (e.g., location, mechanism, time-function, rise-time) is required to form an image. Second, no wavefield storage is required during the back-propagation as the wavefield decomposition (equation 5.2) and the imaging condition (equation 5.1) are applied simultaneously. Third, it uses the full elastic waveform to form an image. For more details see chapter 2.

5.5 Migrated SICP images

5.5.1 Results in 2D

In this section, we present the SICP images along 2D lines that are shown in Figure 5-7. The idea behind constructing 2D images is to delineate the structure of a particular volcanic center. Each 2D line was constructed using different sets of earthquakes because we choose events that fall as closely as possible on the 2D image plane (depth-distance). In Figure 5-10(a), we present 2D SICP image along latitude 64.06° obtained using four stations (SAN, IND, BIT and TRH) and 32 seismic events. This

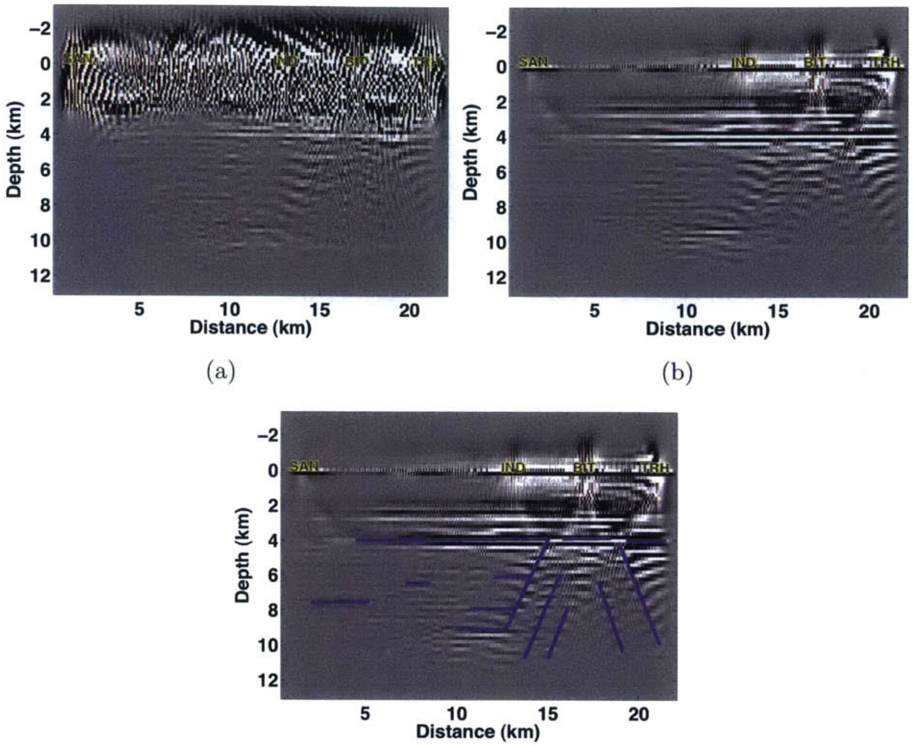

(a) (b)

(c)

Figure 5-10: Migrated 2D SICP image along line with stations: SAN, IND, BIT and TRH with 32 events using P- and S-wave speed models from travel time tomography (Tryggvason et al., 2002): (a) without and (b) with interpolation between the input seismic traces, a procedure described in chapter 3. (c) Structure interpretation of the result (b). Note that the region of BIT station corresponds to Olkelduhals geothermal area.

line crosses the area connecting the volcano centers, Olkelduhals (Foulger & Toomey, 1989) (between longitudes -21.32° and -21.12°). We observe that although the shallow part is completely contaminated by spatial aliasing, the deeper part is reasonably well-imaged. In Figure 5-10(b), we show an image after applying the trace interpolation scheme that is described in chapter 3, to remove the aliasing noise and reconstruct the flat near-surface structure. In Figure 5-10(c), we provide our interpretation, marked with purple lines. We observe that although it is difficult to extrapolate the lines to the surface, we can clearly tie the vertically inclined lines with the fissure swarms (cyan lines) in Figure 5-7 as suggested in Miller et al. (1998).

In Figures 5-11(a) and 5-11(b), we show the migrated images along ENG, IND,

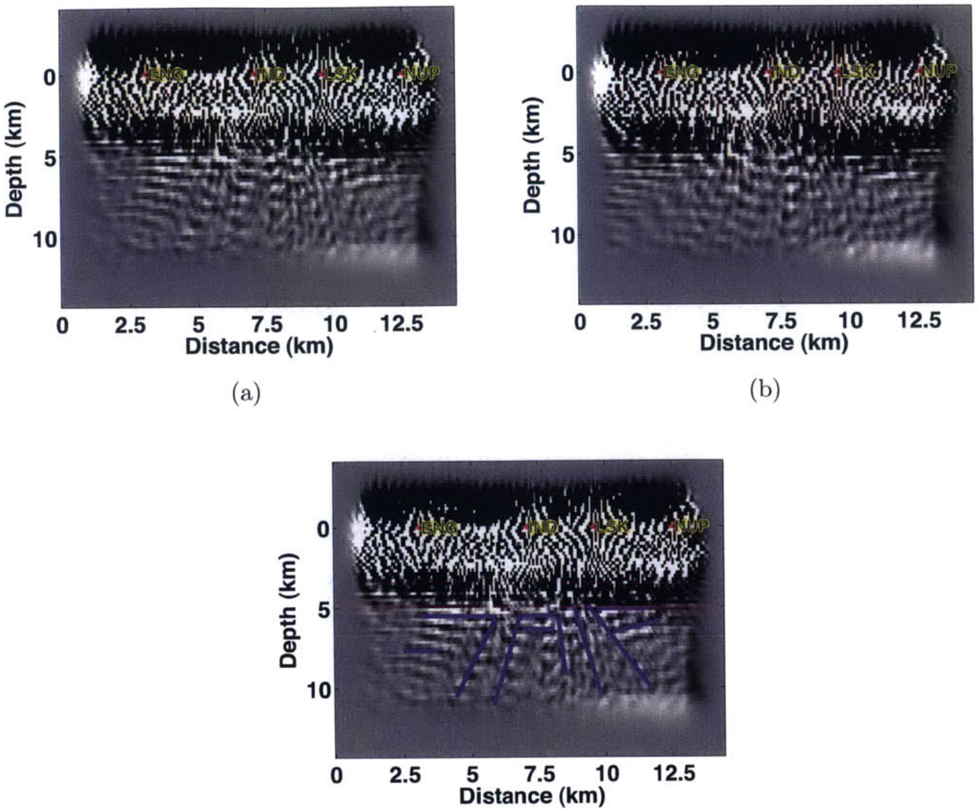

(a)

(b)

(c)

Figure 5-11: Migrated 2D SICP image along line with stations: ENG, IND, LSK and NUP with 22 events and with P- and S-wave speeds from (a) Tryggvason et al. (2002), and (b) regional-scale model. (c) The interpretation based on the SICP image from (a).

LSK and NUP stations obtained with 22 earthquakes using two sets of P- and S-wave speed models: one from Tryggvason et al. (2002) and the extrapolated layered (i.e., regional scale) model. In Figure 5-11(a), we observe that although there is one lineament/fissure swarm at the surface in Figure 5-7 between stations IND and LSK, in Figure 5-11 this feature appears to develop into a series of lineaments at depth between 5 and 10 km (see interpretation in Figure 5-11(c)).

The images constructed with 11 earthquakes along the stations SAN, HVD, HVH and NUP, shown in Figure 5-12 with both sets of velocity models (from Tryggvason et al. (2002) and the regional scale), also show the split of these lineaments at depth (see the interpretation lines in Figure 5-12(c)).

By crossing from south-west to north-east along the (Hr) volcanic center, we form a SICP image along stations LME, HVH, LSK, BIT, KRO using 13 earthquakes (Figure 5-13). We observe again the vertical features associated with fissure swarms from Miller et al. (1998) (cyan lines in Figure 5-7). However, it is difficult to identify the (Hr) volcanic center between BIT and KRO stations (at about 14 and 18 km on the horizontal distance axis); the shallow depths are aliased due to sparse station distribution. By comparing our result with the result of resistivity from Árnason et al. (2010) shown in Figure 5-13(c) along with the interpretation lines from Figure 5-13(b), we find good agreement for depths between 4.5 and 10 km. Note that although Árnason et al. (2000) considered that low resistivity structure corresponds to high temperatures, Árnason et al. (2010) subsequently argued that resistivity structure from the geothermal systems also strongly depends on rock alteration (i.e., presence of different minerals at different temperatures) in the Hengill-Nesjavellir area, and that resistivity might thus increase with increasing temperature. Thus, it is difficult to directly associate high/low resistivity with low/high temperatures (Árnason et al., 2010).

SICP images over the (Gr) volcanic center along the NUP, GUD, TRH and KRO stations are shown in Figure 5-14, where the volcanic center is presumably between GUD and TRH stations. We observe that beneath these stations, vertically inclined features appear and they may correspond to the (Gr) volcanic center. In Figure 5-15, we form another SICP image over (Gr) volcanic center along the stations SKD, BIT, GUD and SOG. Here, we also observe the vertically-inclined lineaments that were suggested by Miller et al. (1998) (cyan lines in Figure 5-7) that are in good correlation with those from Figure 5-14.

5.5.2 Results in 3D

To investigate the 3D structure of the Hengill geothermal area, we also construct 3D SICP images with 32 earthquakes using the P-wave speed and the P- to S-wave speed ratio shown in Figures 5-8 and 5-9. In Figure 5-16, we show depth slices of the 3D SICP images, where we observe the effect of spatial aliasing at shallow depths

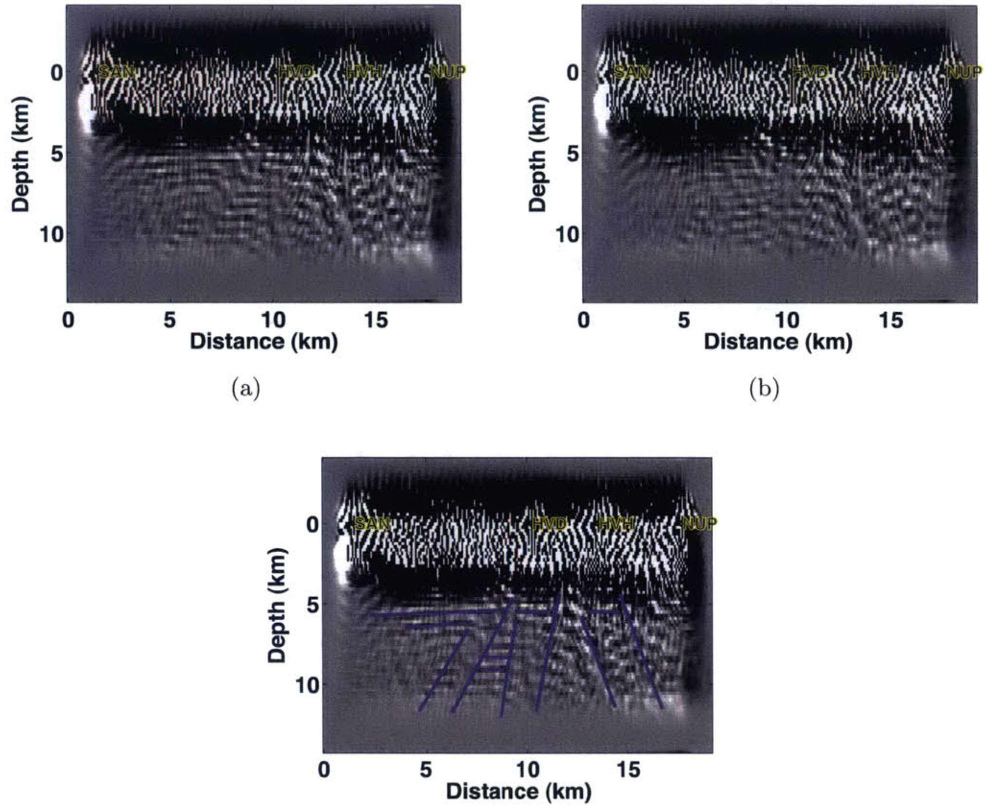

(a)

(b)

(c)

Figure 5-12: Migrated 2D SICP image along line with stations: SAN, HVD, HVH and NUP using 11 events with P- and S-wave speeds from (a) Tryggvason et al. (2002), and (b) regional-scale model. (c) The interpretation based on the SICP image from (a).

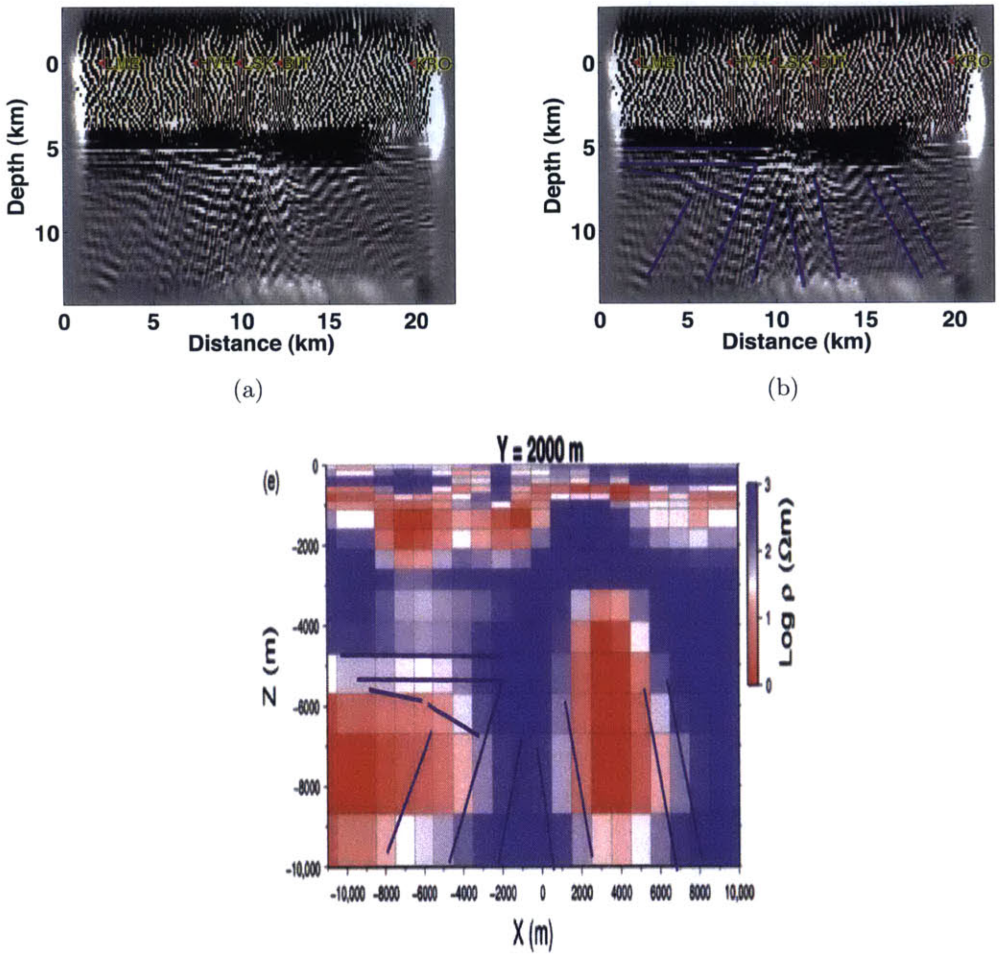

(a)

(b)

(c)

Figure 5-13: (a) Migrated 2D SICP image along LME, HVH, LSK, BIT and KRO stations in Figure 5-7 using 13 events with the P- and S-wave speed models from travel time tomography (Tryggvason et al., 2002), (b) with interpretation, and (c) 2D section of the 3D DC resistivity structure approximately along the same line, reproduced from Árnason et al. (2010), with added interpretation lines from (b). See the structure between 5 and 10 km in both results and in particular vertical alteration in resistivity supported by appearance of vertically inclined lineaments in the SICP image. Note also that high amplitudes in (a) and (b) correspond to the high resistivity (blue color) in (c), and vice versa.

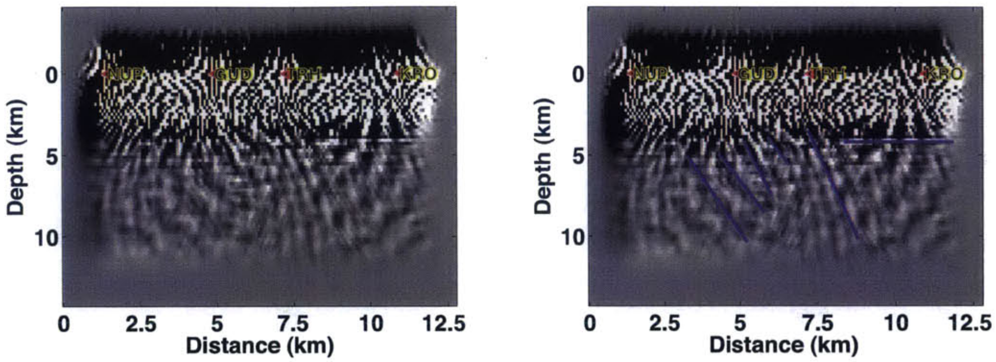

(a) (b)

Figure 5-14: Migrated 2D SICP image along line with stations: NUP, GUD, TRH and KRO using 9 events with the wave speed models from travel time tomography (Tryggvason et al., 2002): (a) without and (b) with interpretation.

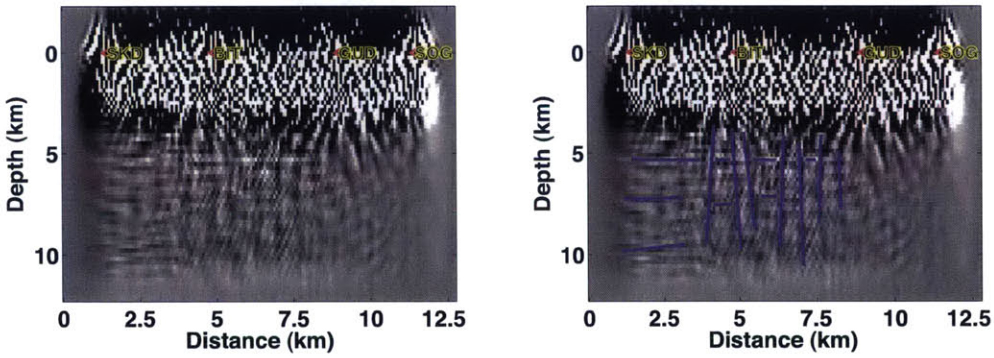

(a) (b)

Figure 5-15: Migrated 2D SICP image along line with stations: SKD, BIT, GUD and SOG with 6 events from using regional wave speed models: (a) without and (b) with interpretation.

(down to about 5.0 km). At greater depths, we start observing the amplitude pattern (marked with blue color) confined by the fissure swarms (see the interpretation of the depth slice at 6.5 km in Figure 5-17(a) placed based on the study of Miller et al. (1998)). This pattern can also be tracked in the deeper depth slices. By comparing these images with the slices of resistivity structure from Árnason et al. (2010) we observe that regions with (blue) amplitudes in Figure 5-17(a) (depth of 6.5 km) have good agreement with the low resistivity (reddish color) region in Figure 5-17(b), and might indicate a link between resistivity and the seismic images produced by SICP imaging.

In Figures 5-18, 5-19 and 5-20, we show 2D west-east sections of the 3D image at different latitudes without (left column) and with our interpretation (right column). The shallow aliased region has been muted. Although it is difficult to extrapolate our interpretation lines to the surface and connect them with the fissure swarms, as was the case for the 2D SICP images, it has clear vertically-inclined lineaments on all images that can be tracked at different latitudes. Of particular interest, in Figure 5-19(e) (Figure 5-19(f) with interpretation), is the image of the Olkelduhals region at the latitude of 64.065° and longitudes between about -21.32° and -21.12°. First, the area characterized by blue color amplitudes is confined (longitudes between about -21.4° and -21.15°); this area corresponds to the high temperature region indicated in many studies (e.g., Miller et al., 1998) and suggests potential existence of the magma body. However, by comparing this line with the 2D SICP image for approximately the same line (shown in Figure 5-10), we find a large discrepancy. Nevertheless, the 2D SICP image has good correlation with the 2D section taken from the 3D image at slightly shifted latitudes to the south at 64.033° (shown in Figures 5-19(a) and 5-19(b)). This mis-positioning effect might be caused by difference between 2D and 3D imaging process. By comparing the 2D and the sections of the 3D SICP images with the section of the resistivity structure (Árnason et al., 2010) from approximately the same region (see the map on the right of Figure 5-21), we observe the dome-like structure, and even more interestingly again the low resistivity (reddish color) corresponds to the seismic amplitudes of the same sign (having the blue color).

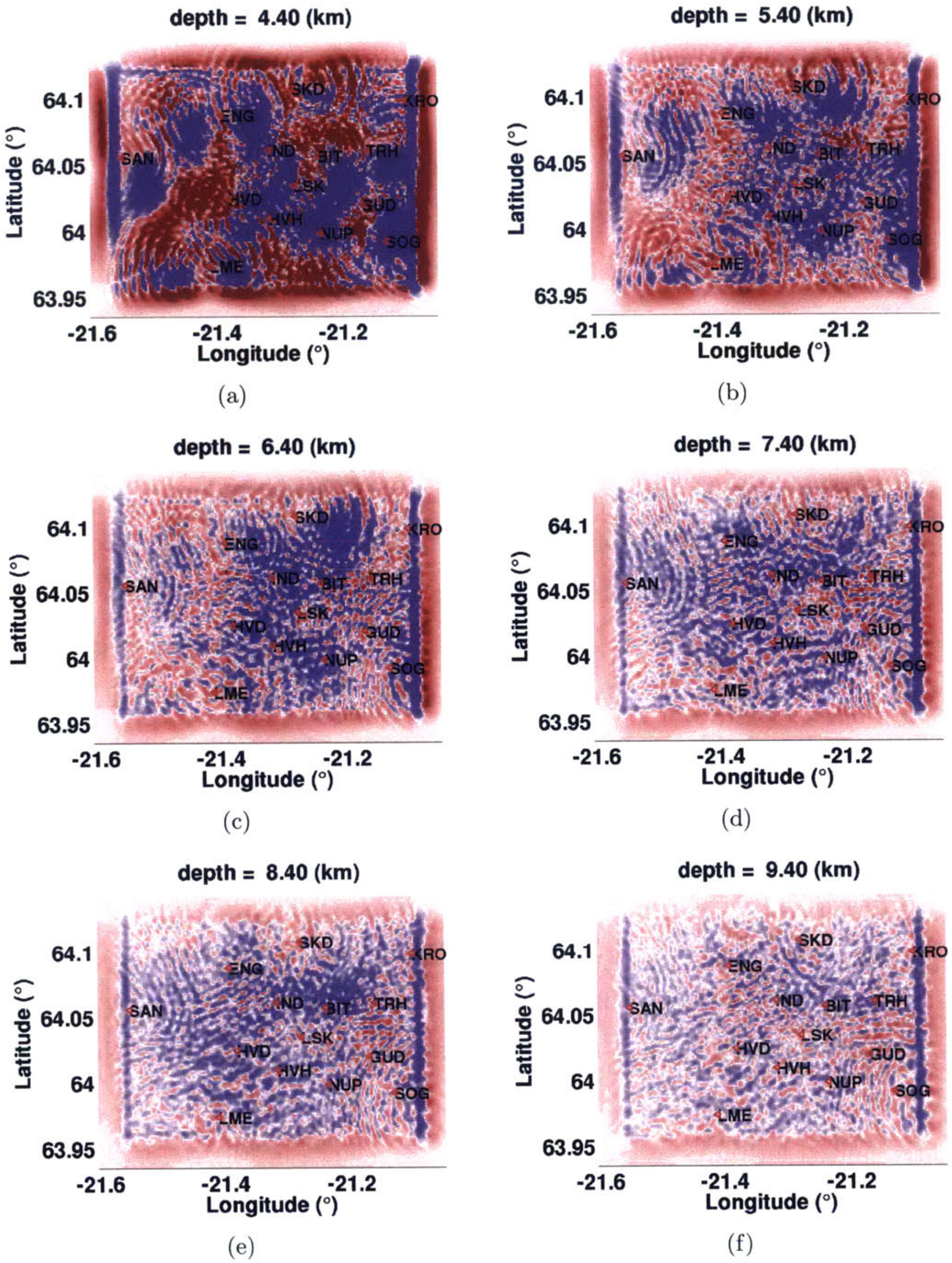

(a) (b) (c) (d) (e) (f)

Figure 5-16: Depth slices of three-dimensional SICP image obtained with 32 earthquakes, shown at depths: (a) 4.4 km, (b) 5.4 km, (c) 6.4 km, (d) 7.4 km, (e) 8.4 km and (f) 9.4 km.

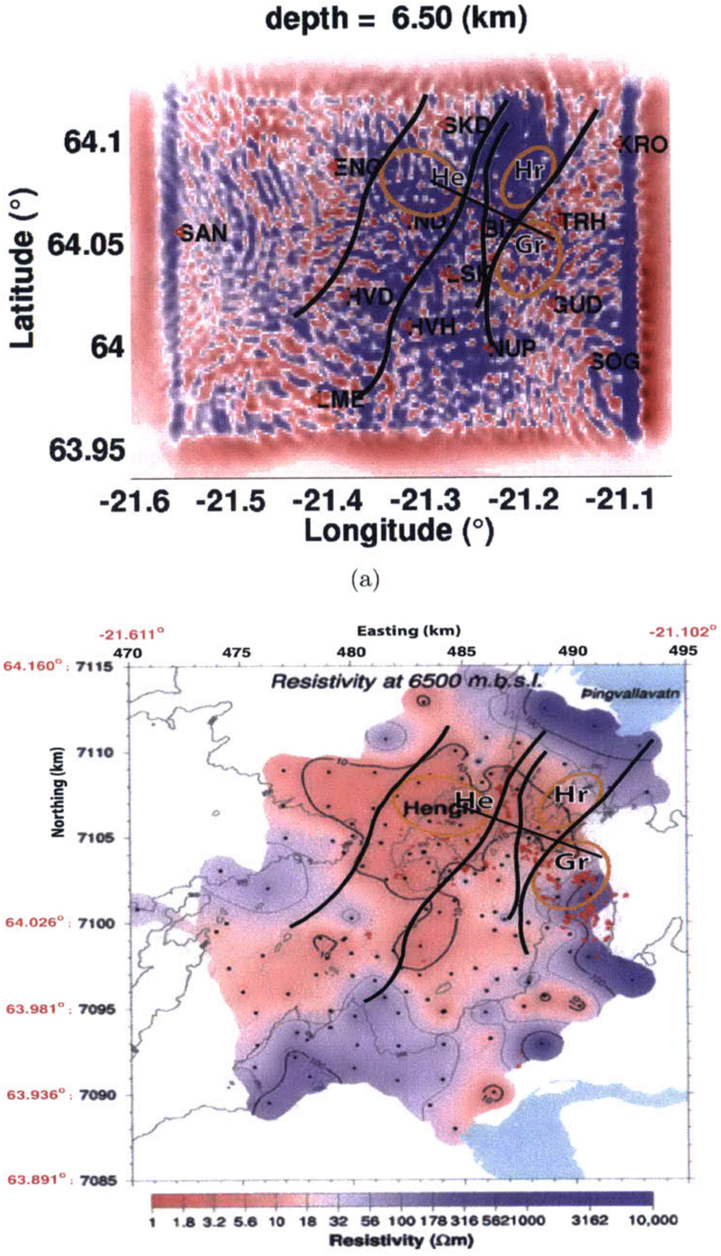

(a)

(b)

Figure 5-17: (a) Projected interpretation from Miller et al. (1998) on the 3D SICP image slieced at the depth of 6.5 km, marking the volcanic centers He, Hr, and Gr (orange lines) and the fissure swarms (black lines). (b) Reproduced from Árnason et al. (2010) for comparison with (a): Resistivity in the Hengill area at the depth of 6.5 km according to joint 1D inversions of TEM and MT data. Red dots: geothermal surface manifestations; black dots: MT soundings; thick black lines: resistivity contour lines; thin black lines: topographic contour lines in meters above sea level. Note the good agreement between high amplitudes (blue color) in 3D SICP migrated image in (a) and the low resistivity (red color) in (b).

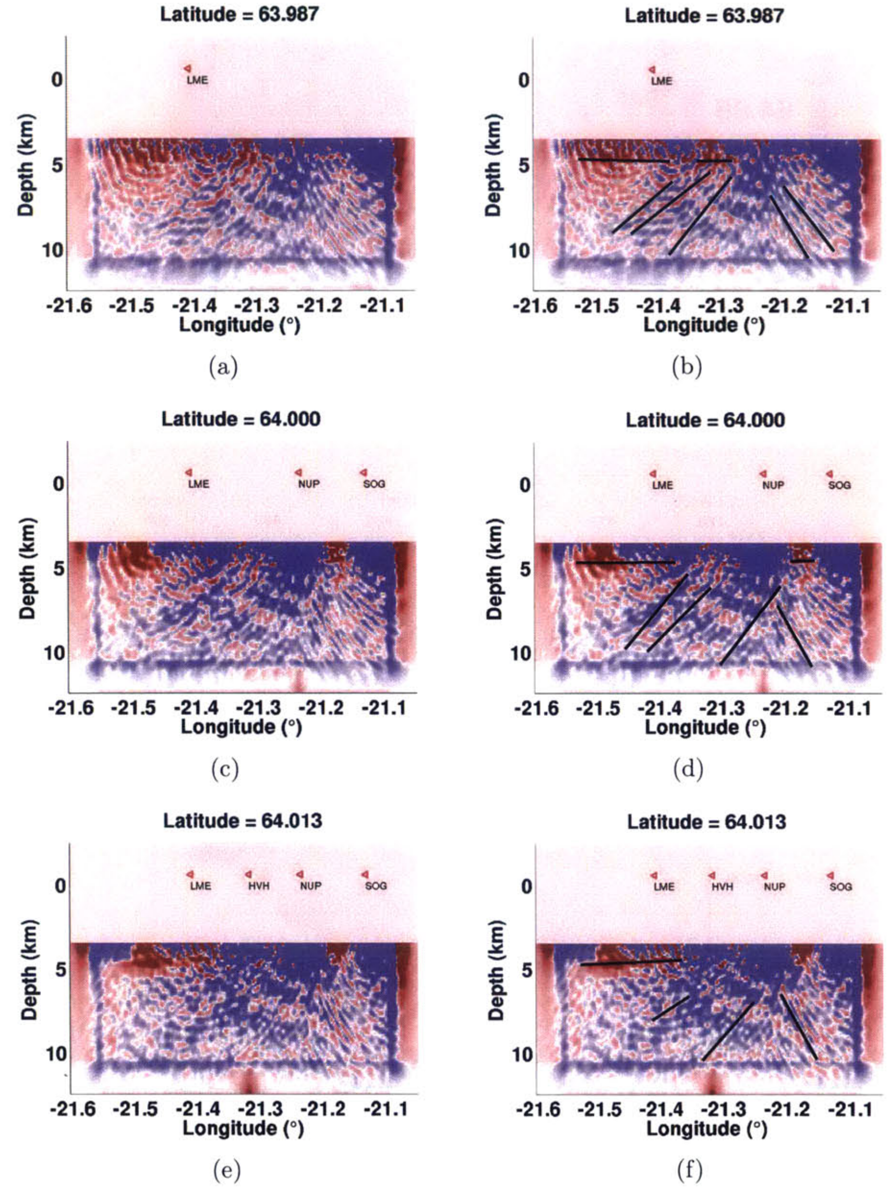

(a) (b)

(c) (d)

(e) (f)

Figure 5-18: Three-dimensional SICP image obtained with 32 earthquakes, shown with and without interpretation at latitude sections: (a-b) 63.987°, (c-d) 64.00°, and (e-f) 64.013°.

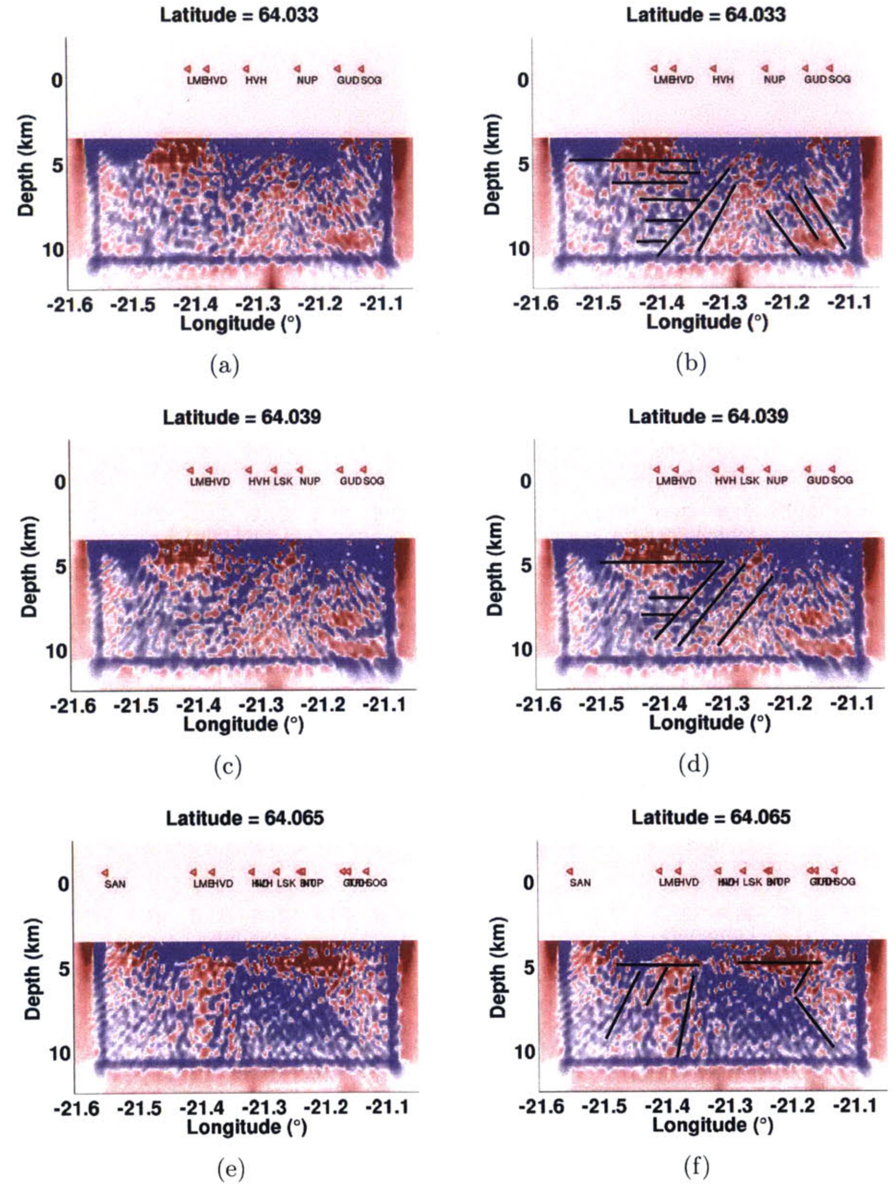

(a) (b)

(c) (d)

(e) (f)

Figure 5-19: Three-dimensional SICP image obtained with 32 earthquakes, shown with and without interpretation at latitude sections: (a-b) 64.033°, (c-d) 64.039°, and (e-f) 64.065°.

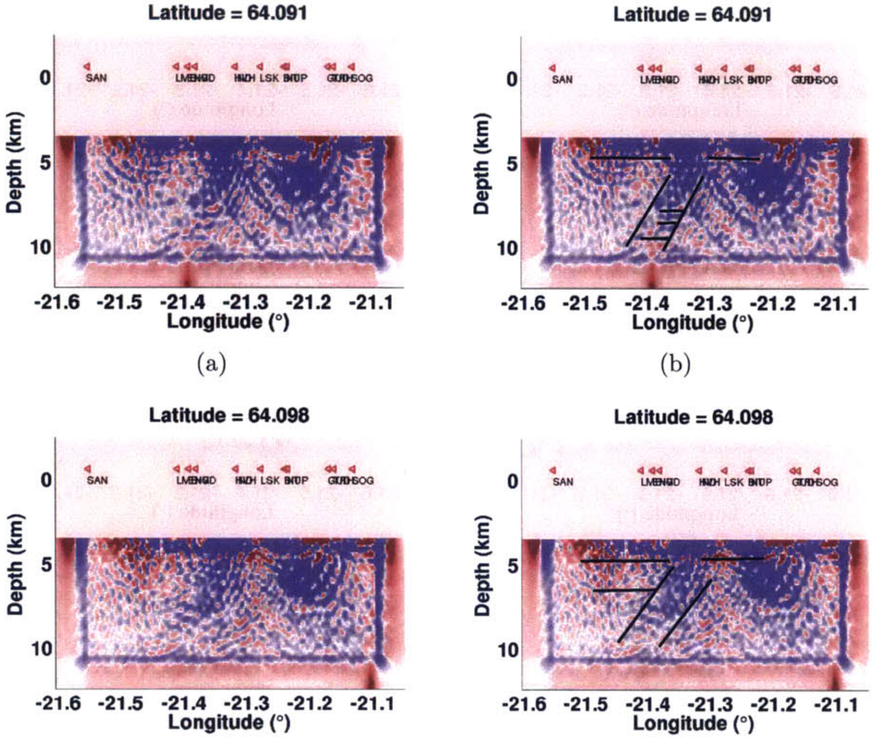

(a) (b)

(c) (d)

Figure 5-20: Three-dimensional SICP image obtained with 32 earthquakes, shown with and without interpretation at latitude sections: (a-b) 64.091° and (c-d) 64.098°.

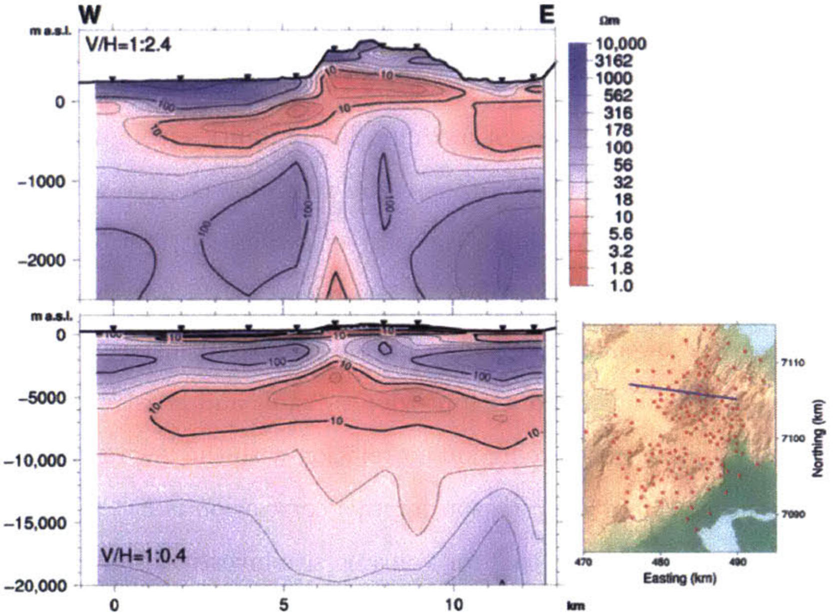

Figure 5-21: Reproduced from Árnason et al. (2010): west-east resistivity sections across the Hengill area for two different depth ranges obtained from stitched joint 1D inversions of TEM and MT data. Inverted triangles: MT stations; V/H: ratio between vertical and horizontal axes. Section location is shown as a blue line in the map to the right. Red dots in that map: MT stations. See the similarity with Figure 5-19(e) (and Figure 5-19(f)) in the dome-like shape and high (blue color) amplitude with the low (red color) DC resistivity at the depths between 5 and 10 km.

In Figures 5-22 and 5-23, we present 2D north-south sections at different longitudes. We make two main observations. First, the lines in general are characterized more with horizontal flat layers. Second, there is a large vertically inclined feature that is not predicted in Miller et al. (1998); see the vertically inclined lineament that is between latitudes 64.00° and 64.05° at longitude -21.49° and is present in all other sections.

5.6 Conclusion

We constructed 2D and 3D images of medium discontinuities using the full wavefield source-independent converted-phase reverse time migration method without using any type of source information. Although the sparse station distribution on the surface produced aliased images at shallow depths, the deeper parts were well-imaged. The constructed images showed detailed information about subsurface structure of the Hengill area that is well correlated with previous seismic and resistivity studies. Also, the amplitude of the images showed good correlation with the low resistivity region of the Hengill geothermal area. The reason for this correlation is not fully understood, but might provide an additional tool for volcanic site investigation.

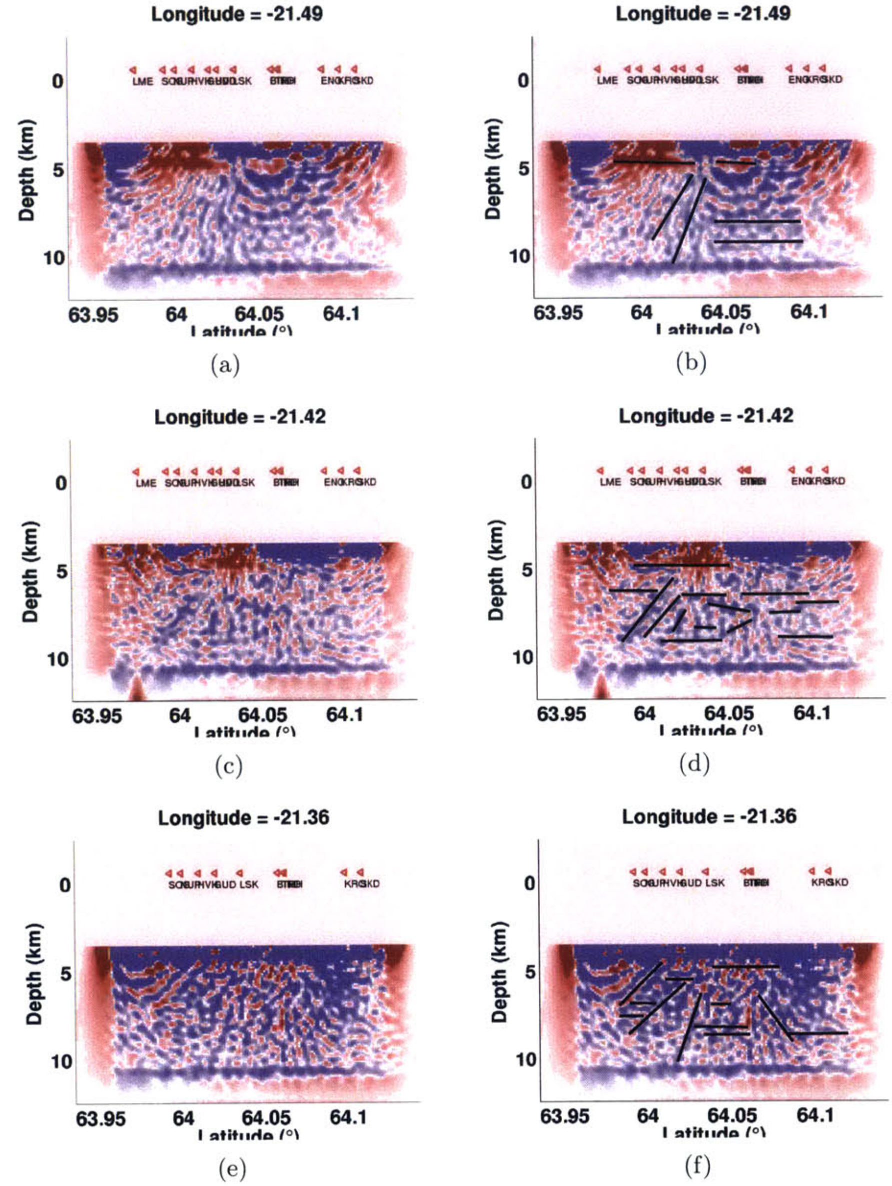

Figure 5-22: Three-dimensional SICP image obtained with 32 earthquakes, shown with and without interpretation at longitude sections: (a-b) -21.49°, (c-d) -21.42°, and (e-f) -21.36°.

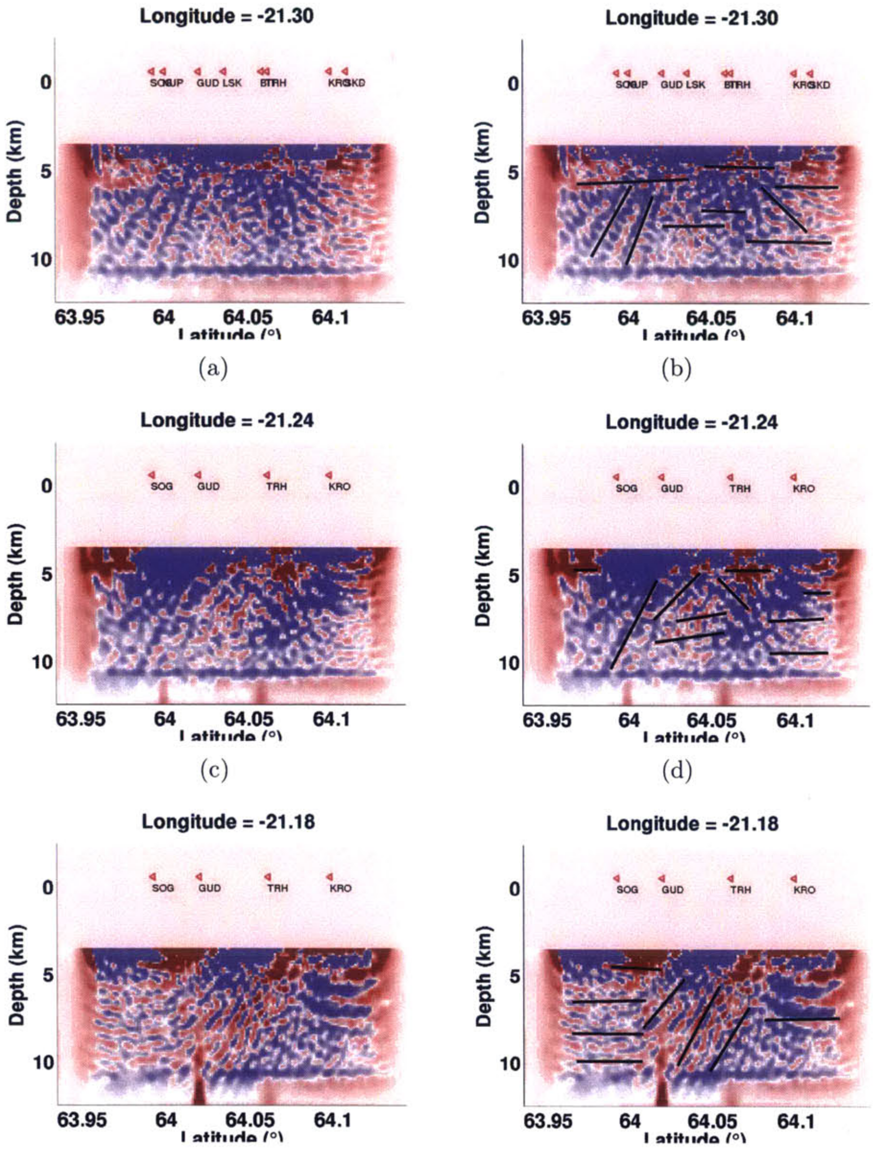

(a) (b)

(c) (d)

(e) (f)

Figure 5-23: Three-dimensional SICP image obtained with 32 earthquakes, shown with and without interpretationat longitude sections: (a-b) -21.30°, (c-d) -21.24° and (e-f) -21.18°.

Chapter 6

Conclusions and Future Work

6.1 Summary of conclusions

In this thesis, I developed and investigated source-independent methodologies for seismic imaging, seismic-trace interpolation and velocity analysis, and applied them to micro-seismic field data from the Hengill geothermal (volcanic) area. I presented mathematical derivations, numerical verifications, and field data examples. I discussed strengths and weaknesses of these methodologies, and highlighted the main goal of this study: the ability to conduct seismic imaging and velocity analysis without using any sort of source information. I found that the source-independent approach for imaging and velocity analysis is possible and beneficial as it facilitates the imaging process by improving the quality of the results and reducing computational and processing effort. This is the main general contribution of my thesis. Here, I am giving the summary of the conclusions for each chapter.

In chapter 2, I presented cross-correlational and de-convolutional forms of a data-driven source independent converted-phase wave imaging condition (SICP-IC), and investigated their relationship with reflection, transmission and conversion coefficients through a newly introduced concept of conversion ratio coefficients. I illustrated the properties of the conversion ratio coefficients and demonstrated their use through de-convolutional imaging conditions with different types of illumination compensation. The results on both the synthetic Marmousi model and field micro-seismic data showed clear advantages of each imaging condition when an appropriate illumination compensation is applied.

In chapter 3, I presented a practical, data-driven, approach for migration-based seismic trace interpolation of sparse micro-seismic data using converted-phases. I demonstrated the approach with synthetic and field data using only an extremely small number of stations. I showed that, using this approach, it is possible to image not only the deeper part of the earth but also its shallow part, without any sort of source information.

In chapter 4, I developed a fully automatic, data-driven optimization method for velocity updating using converted phase waves. I presented a converted-phase imaging condition in the extended space-lag domain for the objective functional. I derived a gradient-based iterative optimization method based on this objective functional and tested the method using a synthetic model and field micro-seismic data. The results show the applicability of the method in particular to micro-seismic applications where source information is not directly available.

In chapter 5, I investigated the Hengill geothermal (volcanic) area by constructing 2D and 3D seismic images of medium discontinuities using the full wavefield source-independent converted-phase reverse time migration method. Although the sparse station distribution on the surface produces aliased images at shallow depths, the deeper parts are well imaged. The application of the method to seismic data produced detailed images of subsurface structure of the Hengill area that are well correlated with previous seismic and resistivity studies. Also, the amplitude of the images showed good correlation with the low resistivity region of the Hengill geothermal area found in Árnason et al. (2010).

6.2 Future directions

This thesis is composed of four main components for source-independent theory and application: seismic-imaging, seismic-trace interpolation, velocity analysis, and study of the Hengill geothermal area. Although, the initial purpose of these four components was to provide tools for the geothermal site investigation, each component evolved into a stand-alone research area that can be further investigated. Here, I list several potential directions for future research for each of these components.

Extension of SICP methodology to an anisotropic medium

To extend the SICP methodology to an anisotropic media, two research directions need to be considered. First, the ability to separate the propagating waves into quasi P and S-waves. Second the derivation of the sensitivity kernels of the SICP-WEMVA for anisotropic model parameters needs to be considered. The first direction has solutions for VTI media (e.g., Dellinger & Etgen, 1990; Yan & Sava, 2009; Yan, 2010; Zhang & McMechan, 2010), but needs further extension to apply more general anisotropy. The second direction requires theoretical investigation using techniques from anisotropic studies for source-dependent WEMVA (Li et al., 2011, 2014).

Further investigation of the conversion ratio coefficients

Although the conversion ratio coefficients were presented in this thesis in the context of the deconvolutional SICP imaging conditions, these coefficients are a stand alone physical quantity that need to be treated as complementary to reflection, transmission and conversion coefficients. In particular, the conversion ratio coefficients may be of great interest in studies of Amplitude Versus Offset (AVO) or Amplitude Versus Azimuth (AVA).

Stabilization factor for amplitude-balancing SICP imaging conditions

The key component of deconvolutional amplitude-balancing ICs is the stabilization factor, ϵ. This factor controls the stability and quality of the imaging process (i.e., ensuring that division by zero is not taking place) and is different for different ICs and data sets. To my knowledge, there is no good strategy to estimate this parameter before an image had been constructed. An approach from Marquardt (1963) may facilitate the procedure for estimating an appropriate stabilization factor for seismic imaging.

SICP Seismic trace interpolation in the framework of Least Square Migration

The seismic trace interpolation scheme shown in chapter 3 is based on the concept that the observed seismic data are used to produce an image, and then this image is de-migrated to reconstruct the missing data. This loop can be formulated into the iterative framework of the least squares migration approach, and thus produce a more balanced interpolated seismic data set along with the migrated seismic image.

Extension of SICP-WEMVA with amplitude-balancing ICs

The SICP-WEMVA method presented in this thesis was based on the cross-correlational imaging condition. The shown merit of the amplitude-balancing deconvolutional imaging conditions should be integrated into SICP-WEMVA to facilitate a better convergence of the SICP-WEMVA optimization scheme, and to suppress the artifacts generated by false waves, shown in Figure 4-9.

Removal of the false waves from wave propagation

The effect of the false waves in the extended-domain space-lag gathers may be significant and thus should also be investigated on the level of the wave propagation. Combining different initial and boundary conditions during the back-propagation might eliminate the generation of these false waves.

Integration of the Hessian into SICP-WEMVA optimization

Adding the Hessian information to the optimization scheme should considerably speed up the convergence of conjugate gradient as well as helping with estimation of an appropriate step length scalar.

SICP-WEMVA for P- and S-wave attenuation

Extension of SICP-WEMVA for constant (in frequency) P- and S-wave attenuation should be considered. This can be easily achieved if the solutions of the elastic wave equation are calculated in the frequency domain.

Interference between other types of waves

In this thesis, I used interference just between P and converted-phase S- (or/and S and converted-phase P-) waves propagating through the isotropic elastic medium. However, if the medium is more complicated, more waves interfere with each other. One example is the shear wave splitting in the anisotropic medium between S-fast and S-slow waves that can be used for the SICP methodology. Also interference can be used between fast and slow Biot waves in poro-elastic medium, or even between seismic and electro-magnetic waves. All these waves can be of a great interest for source-independent imaging.

Application of full 3D SICP-WEMVA and trace interpolation to Hengill data

The 3D amplitude-balancing seismic imaging accompanied with 3D SICP-WEMVA and SICP seismic trace interpolation should improve the quality and resolution of the 3D SICP images and shed additional light on the subsurface structure of the Hengill geothermal area.

Quantitative analysis of the amplitudes of the SICP seismic images

The amplitudes of the SICP seismic images carry important information about the subsurface medium, and thus should be further investigated, particularly in the context of the evaluation of the presence of fluids. Methods based on principal component analysis may be beneficial for this investigation.

Appendix A

Elastic Wave Equation Modeling

A.1 Three-dimensional elastic wave equation modeling with PML boundary conditions.

The engine behind the applications described in this thesis is elastic wave propagation, and the ability to accurately propagate elastic waves is essential for their success. In this appendix, we review the scheme for solution of the isotropic elastic wave equation calculated as a second order in time staggered grid pseudo-spectral method with perfectly matched layers (PML) absorbing boundary conditions.

We will start with the equation for conservation of momentum that is given in the particle velocity $\underline{v} = (v_x, v_y, v_z)$ and stress $\underline{\sigma} = (\sigma_{xx}, \sigma_{yy}, \sigma_{zz}, \sigma_{xy}, \sigma_{xz}, \sigma_{yz})$ representation as

$$\begin{aligned}
\frac{\partial v_x}{\partial t} &= \frac{1}{\rho}\left(\frac{\partial \sigma_{xx}}{\partial x} + \frac{\partial \sigma_{xy}}{\partial y} + \frac{\partial \sigma_{xz}}{\partial z} + f_x\right), \\
\frac{\partial v_y}{\partial t} &= \frac{1}{\rho}\left(\frac{\partial \sigma_{xy}}{\partial x} + \frac{\partial \sigma_{yy}}{\partial y} + \frac{\partial \sigma_{yz}}{\partial z} + f_y\right), \\
\frac{\partial v_z}{\partial t} &= \frac{1}{\rho}\left(\frac{\partial \sigma_{xz}}{\partial x} + \frac{\partial \sigma_{yz}}{\partial y} + \frac{\partial \sigma_{zz}}{\partial z} + f_z\right),
\end{aligned} \tag{A.1}$$

where ρ and $\underline{f} = (f_x, f_y, f_z)$ denote the density and body force, respectively.

Hooke's law for an isotropic body is given with Lamé parameter λ and shear modulus μ as

$$\begin{aligned}
\frac{\partial \sigma_{xx}}{\partial t} &= (\lambda + 2\mu)\frac{\partial v_x}{\partial x} + \lambda\frac{\partial v_y}{\partial y} + \lambda\frac{\partial v_z}{\partial z}, \\
\frac{\partial \sigma_{yy}}{\partial t} &= \lambda\frac{\partial v_x}{\partial x} + (\lambda + 2\mu)\frac{\partial v_y}{\partial y} + \lambda\frac{\partial v_z}{\partial z}, \\
\frac{\partial \sigma_{zz}}{\partial t} &= \lambda\frac{\partial v_x}{\partial x} + \lambda\frac{\partial v_y}{\partial y} + (\lambda + 2\mu)\frac{\partial v_z}{\partial z}, \\
\frac{\partial \sigma_{xy}}{\partial t} &= \mu\left(\frac{\partial v_x}{\partial y} + \frac{\partial v_y}{\partial x}\right), \\
\frac{\partial \sigma_{xz}}{\partial t} &= \mu\left(\frac{\partial v_x}{\partial z} + \frac{\partial v_z}{\partial x}\right), \\
\frac{\partial \sigma_{yz}}{\partial t} &= \mu\left(\frac{\partial v_y}{\partial z} + \frac{\partial v_z}{\partial y}\right).
\end{aligned} \tag{A.2}$$

The Lamé parameters, λ and μ, and density, ρ, define the P- and S-wave speeds by

$$\alpha = \sqrt{\frac{\lambda + 2\mu}{\rho}}, \tag{A.3}$$

and

$$\beta = \sqrt{\frac{\mu}{\rho}}. \tag{A.4}$$

There are many absorbing boundary conditions/layers schemes (e.g., Clayton & Engquist, 1977; Cerjan et al., 1985; Berenger, 1994; Fichtner et al., 2011). Although many simlple schemes exist the Perfectly Matched Layer (PML) scheme requires a very small number of grid points and thus is very attractive. We follow the PML formulation of Collino & Tsogka (2001); Marcinkovich & Olsen (2003) where each wavefield in the equations above is split into parallel and perpendicular terms. Thus, the equations A.1 and A.2 along the x direction are

$$
\begin{aligned}
\frac{\partial v_x^{\perp^x}}{\partial t} + d(x) v_x^{\perp^x} &= \frac{1}{\rho}\left(\frac{\partial \sigma_{xx}}{\partial x} + f_x\right), \\
\frac{\partial v_y^{\perp^x}}{\partial t} + d(x) v_y^{\perp^x} &= \frac{1}{\rho}\frac{\partial \sigma_{yx}}{\partial x}, \\
\frac{\partial v_z^{\perp^x}}{\partial t} + d(x) v_z^{\perp^x} &= \frac{1}{\rho}\frac{\partial \sigma_{xz}}{\partial x}, \\
\frac{\partial \sigma_{xx}^{\perp^x}}{\partial t} + d(x) \sigma_{xx}^{\perp^x} &= (\lambda + 2\mu)\frac{\partial v_x}{\partial x}, \\
\frac{\partial \sigma_{yy}^{\perp^x}}{\partial t} + d(x) \sigma_{yy}^{\perp^x} &= \lambda\frac{\partial v_x}{\partial x}, \\
\frac{\partial \sigma_{zz}^{\perp^x}}{\partial t} + d(x) \sigma_{zz}^{\perp^x} &= \lambda\frac{\partial v_x}{\partial x}, \\
\frac{\partial \sigma_{xy}^{\perp^x}}{\partial t} + d(x) \sigma_{xy}^{\perp^x} &= \mu\frac{\partial v_y}{\partial x}, \\
\frac{\partial \sigma_{xz}^{\perp^x}}{\partial t} + d(x) \sigma_{xz}^{\perp^x} &= \mu\frac{\partial v_z}{\partial x}, \\
\frac{\partial \sigma_{yz}^{\perp^x}}{\partial t} + d(x) \sigma_{yz}^{\perp^x} &= 0,
\end{aligned}
$$

$$
\begin{aligned}
\frac{\partial v_x^{\parallel^x}}{\partial t} &= \frac{1}{\rho}\left(\frac{\partial \sigma_{xy}}{\partial y} + \frac{\partial \sigma_{xz}}{\partial z}\right), \\
\frac{\partial v_y^{\parallel^x}}{\partial t} &= \frac{1}{\rho}\left(\frac{\partial \sigma_{yy}}{\partial y} + \frac{\partial \sigma_{yz}}{\partial z}\right), \\
\frac{\partial v_z^{\parallel^x}}{\partial t} &= \frac{1}{\rho}\left(\frac{\partial \sigma_{yz}}{\partial y} + \frac{\partial \sigma_{zz}}{\partial z}\right), \\
\frac{\partial \sigma_{xx}^{\parallel^x}}{\partial t} &= \lambda\left(\frac{\partial v_y}{\partial y} + \frac{\partial v_z}{\partial z}\right), \\
\frac{\partial \sigma_{yy}^{\parallel^x}}{\partial t} &= (\lambda + 2\mu)\frac{\partial v_y}{\partial y} + \lambda\frac{\partial v_z}{\partial z}, \\
\frac{\partial \sigma_{zz}^{\parallel^x}}{\partial t} &= \lambda\frac{\partial v_y}{\partial y} + (\lambda + 2\mu)\frac{\partial v_z}{\partial z}, \\
\frac{\partial \sigma_{xy}^{\parallel^x}}{\partial t} &= \mu\frac{\partial v_x}{\partial y}, \\
\frac{\partial \sigma_{xz}^{\parallel^x}}{\partial t} &= \mu\frac{\partial v_x}{\partial z}, \\
\frac{\partial \sigma_{yz}^{\parallel^x}}{\partial t} &= \mu\left(\frac{\partial v_y}{\partial z} + \frac{\partial v_z}{\partial y}\right),
\end{aligned}
\tag{A.5}
$$

along the y direction are

$$
\begin{aligned}
&\frac{\partial v_x^{\perp y}}{\partial t} + d(y) v_x^{\perp y} = \frac{1}{\rho}\frac{\partial \sigma_{xy}}{\partial y}, && \frac{\partial v_x^{\| y}}{\partial t} = \frac{1}{\rho}\left(\frac{\partial \sigma_{xx}}{\partial x} + \frac{\partial \sigma_{xz}}{\partial z}\right),\\
&\frac{\partial v_y^{\perp y}}{\partial t} + d(y) v_y^{\perp y} = \left(\frac{1}{\rho}\frac{\partial \sigma_{yy}}{\partial y} + f_y\right), && \frac{\partial v_y^{\| y}}{\partial t} = \frac{1}{\rho}\left(\frac{\partial \sigma_{xy}}{\partial x} + \frac{\partial \sigma_{yz}}{\partial z}\right),\\
&\frac{\partial v_z^{\perp y}}{\partial t} + d(y) v_z^{\perp y} = \frac{1}{\rho}\frac{\partial \sigma_{yz}}{\partial y}, && \frac{\partial v_z^{\| y}}{\partial t} = \frac{1}{\rho}\left(\frac{\partial \sigma_{xz}}{\partial x} + \frac{\partial \sigma_{zz}}{\partial z}\right),\\
&\frac{\partial \sigma_{xx}^{\perp y}}{\partial t} + d(y) \sigma_{xx}^{\perp y} = \lambda\frac{\partial v_y}{\partial y}, && \frac{\partial \sigma_{xx}^{\| y}}{\partial t} = (\lambda + 2\mu)\frac{\partial v_x}{\partial x} + \lambda\frac{\partial v_z}{\partial z},\\
&\frac{\partial \sigma_{yy}^{\perp y}}{\partial t} + d(y) \sigma_{yy}^{\perp y} = (\lambda + 2\mu)\frac{\partial v_y}{\partial y}, && \frac{\partial \sigma_{yy}^{\| y}}{\partial t} = \lambda\left(\frac{\partial v_x}{\partial x} + \frac{\partial v_z}{\partial z}\right),\\
&\frac{\partial \sigma_{zz}^{\perp y}}{\partial t} + d(y) \sigma_{zz}^{\perp y} = \lambda\frac{\partial v_y}{\partial y}, && \frac{\partial \sigma_{zz}^{\| y}}{\partial t} = \lambda\frac{\partial v_x}{\partial x} + (\lambda + 2\mu)\frac{\partial v_z}{\partial z},\\
&\frac{\partial \sigma_{xy}^{\perp y}}{\partial t} + d(y) \sigma_{xy}^{\perp y} = \mu\frac{\partial v_x}{\partial y}, && \frac{\partial \sigma_{xy}^{\| y}}{\partial t} = \mu\frac{\partial v_y}{\partial x},\\
&\frac{\partial \sigma_{xz}^{\perp y}}{\partial t} + d(y) \sigma_{xz}^{\perp y} = 0, && \frac{\partial \sigma_{xz}^{\| y}}{\partial t} = \mu\left(\frac{\partial v_x}{\partial z} + \frac{\partial v_z}{\partial x}\right),\\
&\frac{\partial \sigma_{yz}^{\perp y}}{\partial t} + d(y) \sigma_{yz}^{\perp y} = \frac{\partial v_z}{\partial y}, && \frac{\partial \sigma_{yz}^{\| y}}{\partial t} = \mu\frac{\partial v_y}{\partial z},
\end{aligned}
\tag{A.6}
$$

and along the z direction are

$$
\begin{aligned}
&\frac{\partial v_x^{\perp^z}}{\partial t} + d(z) v_x^{\perp^z} = \frac{1}{\rho}\frac{\partial \sigma_{xz}}{\partial z}, &&\frac{\partial v_x^{\|^z}}{\partial t} = \frac{1}{\rho}\left(\frac{\partial \sigma_{xx}}{\partial x} + \frac{\partial \sigma_{xy}}{\partial y}\right),\\
&\frac{\partial v_y^{\perp^z}}{\partial t} + d(z) v_y^{\perp^z} = \frac{1}{\rho}\frac{\partial \sigma_{yz}}{\partial z}, &&\frac{\partial v_x^{\|^z}}{\partial t} = \frac{1}{\rho}\left(\frac{\partial \sigma_{xy}}{\partial x} + \frac{\partial \sigma_{yy}}{\partial y}\right),\\
&\frac{\partial v_z^{\perp^z}}{\partial t} + d(z) v_z^{\perp^z} = \frac{1}{\rho}\left(\frac{\partial \sigma_{zz}}{\partial z} + f_z\right), &&\frac{\partial v_z^{\|^z}}{\partial t} = \frac{1}{\rho}\left(\frac{\partial \sigma_{xz}}{\partial x} + \frac{\partial \sigma_{yz}}{\partial y}\right),\\
&\frac{\partial \sigma_{xx}^{\perp^z}}{\partial t} + d(z) \sigma_{xx}^{\perp^z} = \lambda\frac{\partial v_z}{\partial z}, &&\frac{\partial \sigma_{xx}^{\|^z}}{\partial t} = (\lambda + 2\mu)\frac{\partial v_x}{\partial x} + \lambda\frac{\partial v_y}{\partial y},\\
&\frac{\partial \sigma_{yy}^{\perp^z}}{\partial t} + d(z) \sigma_{yy}^{\perp^z} = \lambda\frac{\partial v_z}{\partial z}, &&\frac{\partial \sigma_{yy}^{\|^z}}{\partial t} = \lambda\frac{\partial v_x}{\partial x} + (\lambda + 2\mu)\frac{\partial v_y}{\partial y},\\
&\frac{\partial \sigma_{zz}^{\perp^z}}{\partial t} + d(z) \sigma_{zz}^{\perp^z} = (\lambda + 2\mu)\frac{\partial v_z}{\partial z}, &&\frac{\partial \sigma_{zz}^{\|^z}}{\partial t} = \lambda\left(\frac{\partial v_x}{\partial x} + \frac{\partial v_y}{\partial y}\right),\\
&\frac{\partial \sigma_{xy}^{\perp^z}}{\partial t} + d(z) \sigma_{xy}^{\perp^z} = 0, &&\frac{\partial \sigma_{xy}^{\|^z}}{\partial t} = \mu\left(\frac{\partial v_x}{\partial y} + \frac{\partial v_y}{\partial x}\right),\\
&\frac{\partial \sigma_{xz}^{\perp^z}}{\partial t} + d(z) \sigma_{xz}^{\perp^z} = \mu\frac{\partial v_x}{\partial z}, &&\frac{\partial \sigma_{xz}^{\|^z}}{\partial t} = \mu\frac{\partial v_z}{\partial x},\\
&\frac{\partial \sigma_{yz}^{\perp^z}}{\partial t} + d(z) \sigma_{yz}^{\perp^z} = \mu\frac{\partial v_y}{\partial z}, &&\frac{\partial \sigma_{yz}^{\|^z}}{\partial t} = \mu\frac{\partial v_z}{\partial y}.
\end{aligned}
\tag{A.7}
$$

where the $d(x)$, $d(y)$, and $d(z)$ are the PML functions. Representatively, $d(x)$ is given as (Marcinkovich & Olsen, 2003):

$$
d(x) = \frac{\tau\beta}{\Delta x}(c_1 + c_2 n_b + c_3 n_b^2) \tag{A.8}
$$

where τ is a free scalar, β is the S-wave speed, Δx is the x grid spacing, n_b is the PML thickness (in nodes), and the polynomial coefficients are: $c_1 = \frac{8}{15}$, $c_2 = \frac{-3}{100}$ and $c_3 = \frac{1}{1500}$.

A.1.1 Discretization of elastic wave equation on staggered grid

The above equations are discretized using the preudo-spectral staggered grid discretization that yields

$$(V_x)_{i,j,k}^{n+1} = (V_x^x)_{i,j,k}^{n+1} + (V_x^y)_{i,j,k}^{n+1} + (V_x^z)_{i,j,k}^{n+1} \tag{A.9}$$

$$\frac{(V_x^x)_{i,j,k}^{n+1} - (V_x^x)_{i,j,k}^{n}}{\Delta t} + d_i^x \frac{(V_x^x)_{i,j,k}^{n+1} + (V_x^x)_{i,j,k}^{n}}{2} = \frac{1}{\rho_{i,j,k}} \left(\frac{\partial (\Sigma_{xx})_{i,j,k}^{n+\frac{1}{2}}}{\partial x} + (f_x)_{i,j,k}^{n} \right) \tag{A.10}$$

$$\frac{(V_x^y)_{i,j,k}^{n+1} - (V_x^y)_{i,j,k}^{n}}{\Delta t} + d_k^y \frac{(V_x^y)_{i,j,k}^{n+1} + (V_x^y)_{i,j,k}^{n}}{2} = \frac{1}{\rho_{i,j,k}} \frac{\partial (\Sigma_{xy})_{i,j,k}^{n+\frac{1}{2}}}{\partial y} \tag{A.11}$$

$$\frac{(V_x^z)_{i,j,k}^{n+1} - (V_x^z)_{i,j,k}^{n}}{\Delta t} + d_k^z \frac{(V_x^z)_{i,j,k}^{n+1} + (V_x^z)_{i,j,k}^{n}}{2} = \frac{1}{\rho_{i,j,k}} \frac{\partial (\Sigma_{xz})_{i,j,k}^{n+\frac{1}{2}}}{\partial z} \tag{A.12}$$

$$(V_y)_{i+\frac{1}{2},j+\frac{1}{2},k}^{n+1} = (V_y^x)_{i+\frac{1}{2},j+\frac{1}{2},k}^{n+1} + (V_y^y)_{i+\frac{1}{2},j+\frac{1}{2},k}^{n+1} + (V_y^z)_{i+\frac{1}{2},j+\frac{1}{2},k}^{n+1} \tag{A.13}$$

$$\begin{aligned} \frac{(V_y^x)_{i+\frac{1}{2},j+\frac{1}{2},k}^{n+1} - (V_y^x)_{i+\frac{1}{2},j+\frac{1}{2},k}^{n}}{\Delta t} &+ d_{i+\frac{1}{2}}^x \frac{(V_y^x)_{i+\frac{1}{2},j+\frac{1}{2},k}^{n+1} + (V_y^x)_{i+\frac{1}{2},j+\frac{1}{2},k}^{n}}{2} \\ &= \frac{1}{\rho_{i+\frac{1}{2},j+\frac{1}{2},k}} \frac{\partial (\Sigma_{xy})_{i+\frac{1}{2},j+\frac{1}{2},k}^{n+\frac{1}{2}}}{\partial x} \end{aligned} \tag{A.14}$$

$$\begin{aligned} \frac{(V_y^z)_{i+\frac{1}{2},j+\frac{1}{2},k}^{n+1} - (V_y^z)_{i+\frac{1}{2},j+\frac{1}{2},k}^{n}}{\Delta t} &+ d_{i+\frac{1}{2}}^z \frac{(V_y^z)_{i+\frac{1}{2},j+\frac{1}{2},k}^{n+1} + (V_y^z)_{i+\frac{1}{2},j+\frac{1}{2},j}^{n}}{2} \\ &= \frac{1}{\rho_{i+\frac{1}{2},j+\frac{1}{2},k}} \left(\frac{\partial (\Sigma_{zz})_{i+\frac{1}{2},j+\frac{1}{2},k}^{n+\frac{1}{2}}}{\partial z} + (f_z)_{i+\frac{1}{2}}^{n} \right) \end{aligned} \tag{A.15}$$

$$(V_z)_{i+\frac{1}{2},j,k+\frac{1}{2}}^{n+1} = (V_z^x)_{i+\frac{1}{2},j,k+\frac{1}{2}}^{n+1} + (V_z^y)_{i+\frac{1}{2},j,k+\frac{1}{2}}^{n+1} + (V_z^z)_{i+\frac{1}{2},j,k+\frac{1}{2}}^{n+1} \tag{A.16}$$

$$\begin{aligned}\frac{(V_z^x)^{n+1}_{i+\frac{1}{2},j,k+\frac{1}{2}} - (V_z^x)^{n}_{i+\frac{1}{2},j,k+\frac{1}{2}}}{\Delta t} &+ d^x_{i+\frac{1}{2}} \frac{(V_z^x)^{n+1}_{i+\frac{1}{2},j,k+\frac{1}{2}} + (V_z^x)^{n}_{i+\frac{1}{2},j,k+\frac{1}{2}}}{2} \\ &= \frac{1}{\rho_{i+\frac{1}{2},j,k+\frac{1}{2}}} \frac{\partial (\Sigma_{xz})^{n+\frac{1}{2}}_{i+\frac{1}{2},j,k+\frac{1}{2}}}{\partial x}\end{aligned} \tag{A.17}$$

$$\begin{aligned}\frac{(V_z^y)^{n+1}_{i+\frac{1}{2},j,k+\frac{1}{2}} - (V_z^y)^{n}_{i+\frac{1}{2},j,k+\frac{1}{2}}}{\Delta t} &+ d^y_{j} \frac{(V_z^y)^{n+1}_{i+\frac{1}{2},j,k+\frac{1}{2}} + (V_z^y)^{n}_{i+\frac{1}{2},j,k+\frac{1}{2}}}{2} \\ &= \frac{1}{\rho_{i+\frac{1}{2},j,k+\frac{1}{2}}} \frac{\partial (\Sigma_{yz})^{n+\frac{1}{2}}_{i+\frac{1}{2},j,k+\frac{1}{2}}}{\partial y}\end{aligned} \tag{A.18}$$

$$\begin{aligned}\frac{(V_z^z)^{n+1}_{i+\frac{1}{2},j,k+\frac{1}{2}} - (V_z^z)^{n}_{i+\frac{1}{2},j,k+\frac{1}{2}}}{\Delta t} &+ d^z_{k+\frac{1}{2}} \frac{(V_z^z)^{n+1}_{i+\frac{1}{2},j,k+\frac{1}{2}} + (V_z^z)^{n}_{i+\frac{1}{2},k+\frac{1}{2}}}{2} \\ &= \frac{1}{\rho_{i+\frac{1}{2},j,k+\frac{1}{2}}} \left(\frac{\partial (\Sigma_{zz})^{n+\frac{1}{2}}_{i+\frac{1}{2},j,k+\frac{1}{2}}}{\partial z} + (f_z)^{n}_{i+\frac{1}{2},j,k+\frac{1}{2}} \right)\end{aligned} \tag{A.19}$$

$$(\Sigma_{xx})^{n+\frac{1}{2}}_{i+\frac{1}{2},j,k} = (\Sigma^x_{xx})^{n+\frac{1}{2}}_{i+\frac{1}{2},j,k} + (\Sigma^y_{xx})^{n+\frac{1}{2}}_{i+\frac{1}{2},j,k} + (\Sigma^z_{xx})^{n+\frac{1}{2}}_{i+\frac{1}{2},j,k} \tag{A.20}$$

$$\begin{aligned}\frac{(\Sigma^x_{xx})^{n+\frac{1}{2}}_{i+\frac{1}{2},j,k} - (\Sigma^x_{xx})^{n-\frac{1}{2}}_{i+\frac{1}{2},j,k}}{\Delta t} &+ d^x_{i+\frac{1}{2}} \frac{(\Sigma^x_{xx})^{n+\frac{1}{2}}_{i+\frac{1}{2},j,k} + (\Sigma^x_{xx})^{n-\frac{1}{2}}_{i+\frac{1}{2},j,k}}{2} \\ &= (\lambda_{i+\frac{1}{2},j,k} + 2\mu_{i+\frac{1}{2},j,k}) \frac{\partial (V_x)^{n}_{i+\frac{1}{2},j,k}}{\partial x}\end{aligned} \tag{A.21}$$

$$\frac{(\Sigma^y_{xx})^{n+\frac{1}{2}}_{i+\frac{1}{2},j,k} - (\Sigma^y_{xx})^{n-\frac{1}{2}}_{i+\frac{1}{2},j,k}}{\Delta t} + d^y_{j} \frac{(\Sigma^y_{xx})^{n+\frac{1}{2}}_{i+\frac{1}{2},j,k} + (\Sigma^y_{xx})^{n-\frac{1}{2}}_{i+\frac{1}{2},j,k}}{2} = \lambda_{i+\frac{1}{2},j,k} \frac{\partial (V_y)^{n}_{i+\frac{1}{2},j,k}}{\partial y} \tag{A.22}$$

$$\frac{(\Sigma^z_{xx})^{n+\frac{1}{2}}_{i+\frac{1}{2},j,k} - (\Sigma^z_{xx})^{n-\frac{1}{2}}_{i+\frac{1}{2},j,k}}{\Delta t} + d^z_{k} \frac{(\Sigma^z_{xx})^{n+\frac{1}{2}}_{i+\frac{1}{2},j,k} + (\Sigma^z_{xx})^{n-\frac{1}{2}}_{i+\frac{1}{2},j,k}}{2} = \lambda_{i+\frac{1}{2},j,k} \frac{\partial (V_z)^{n}_{i+\frac{1}{2},j,k}}{\partial z} \tag{A.23}$$

$$(\Sigma_{zz})^{n+\frac{1}{2}}_{i+\frac{1}{2},j,k} = (\Sigma^x_{zz})^{n+\frac{1}{2}}_{i+\frac{1}{2},j,k} + (\Sigma^y_{zz})^{n+\frac{1}{2}}_{i+\frac{1}{2},j,k} + (\Sigma^z_{zz})^{n+\frac{1}{2}}_{i+\frac{1}{2},j,k} \tag{A.24}$$

$$\frac{(\Sigma^x_{zz})^{n+\frac{1}{2}}_{i+\frac{1}{2},j,k} - (\Sigma^x_{zz})^{n-\frac{1}{2}}_{i+\frac{1}{2},j,k}}{\Delta t} + d^x_{i+\frac{1}{2}} \frac{(\Sigma^x_{zz})^{n+\frac{1}{2}}_{i+\frac{1}{2},j,k} + (\Sigma^x_{zz})^{n-\frac{1}{2}}_{i+\frac{1}{2},j,k}}{2} = \lambda_{i+\frac{1}{2},j,k} \frac{\partial (V_x)^n_{i+\frac{1}{2},j,k}}{\partial x} \tag{A.25}$$

$$\frac{(\Sigma^y_{zz})^{n+\frac{1}{2}}_{i+\frac{1}{2},j,k} - (\Sigma^y_{zz})^{n-\frac{1}{2}}_{i+\frac{1}{2},j,k}}{\Delta t} + d^y_j \frac{(\Sigma^y_{zz})^{n+\frac{1}{2}}_{i+\frac{1}{2},j,k} + (\Sigma^y_{zz})^{n-\frac{1}{2}}_{i+\frac{1}{2},j,k}}{2} = \lambda_{i+\frac{1}{2},j,k} \frac{\partial (V_x)^n_{i+\frac{1}{2},j,k}}{\partial x} \tag{A.26}$$

$$\frac{(\Sigma^z_{zz})^{n+\frac{1}{2}}_{i+\frac{1}{2},k} - (\Sigma^z_{zz})^{n-\frac{1}{2}}_{i+\frac{1}{2},k}}{\Delta t} + d^z_k \frac{(\Sigma^z_{zz})^{n+\frac{1}{2}}_{i+\frac{1}{2},k} + (\Sigma^z_{zz})^{n-\frac{1}{2}}_{i+\frac{1}{2},k}}{2} = (\lambda_{i+\frac{1}{2},k} + 2\mu_{i+\frac{1}{2},k}) \frac{\partial (V_z)^n_{i+\frac{1}{2},k}}{\partial z} \tag{A.27}$$

$$(\Sigma_{xy})^{n+\frac{1}{2}}_{i,j+\frac{1}{2},k} = (\Sigma^x_{xy})^{n+\frac{1}{2}}_{i,j+\frac{1}{2},k} + (\Sigma^z_{xy})^{n+\frac{1}{2}}_{i,j+\frac{1}{2},k} \tag{A.28}$$

$$\frac{(\Sigma^x_{xy})^{n+\frac{1}{2}}_{i,j+\frac{1}{2},k} - (\Sigma^x_{xy})^{n-\frac{1}{2}}_{i,j+\frac{1}{2},k}}{\Delta t} + d^x_i \frac{(\Sigma^x_{xy})^{n+\frac{1}{2}}_{i,j+\frac{1}{2},k} + (\Sigma^x_{xy})^{n-\frac{1}{2}}_{i,j+\frac{1}{2},k}}{2} = \mu_{i,j+\frac{1}{2},k} \frac{\partial (V_y)^n_{i,j+\frac{1}{2},k}}{\partial x} \tag{A.29}$$

$$\frac{(\Sigma^y_{xy})^{n+\frac{1}{2}}_{i,j+\frac{1}{2},k} - (\Sigma^y_{xy})^{n-\frac{1}{2}}_{i,j+\frac{1}{2},k}}{\Delta t} + d^y_j \frac{(\Sigma^y_{xy})^{n+\frac{1}{2}}_{i,j+\frac{1}{2},k} + (\Sigma^y_{xy})^{n-\frac{1}{2}}_{i,j+\frac{1}{2},k}}{2} = \mu_{i,j+\frac{1}{2},k} \frac{\partial (V_x)^n_{i,j+\frac{1}{2},k}}{\partial y} \tag{A.30}$$

$$\frac{(\Sigma^z_{xy})^{n+\frac{1}{2}}_{i,j+\frac{1}{2},k} - (\Sigma^z_{xy})^{n-\frac{1}{2}}_{i,j+\frac{1}{2},k}}{\Delta t} + d^z_k \frac{(\Sigma^z_{xy})^{n+\frac{1}{2}}_{i,j+\frac{1}{2},k} + (\Sigma^z_{xy})^{n-\frac{1}{2}}_{i,j+\frac{1}{2},k}}{2} = 0 \tag{A.31}$$

$$(\Sigma_{xz})^{n+\frac{1}{2}}_{i,j,k+\frac{1}{2}} = (\Sigma^{x}_{xz})^{n+\frac{1}{2}}_{i,j,k+\frac{1}{2}} + (\Sigma^{y}_{xz})^{n+\frac{1}{2}}_{i,j,k+\frac{1}{2}} + (\Sigma^{z}_{xz})^{n+\frac{1}{2}}_{i,j,k+\frac{1}{2}} \tag{A.32}$$

$$\frac{(\Sigma^{x}_{xz})^{n+\frac{1}{2}}_{i,j,k+\frac{1}{2}} - (\Sigma^{x}_{xz})^{n-\frac{1}{2}}_{i,j,k+\frac{1}{2}}}{\Delta t} + d^{x}_{i}\frac{(\Sigma^{x}_{xz})^{n+\frac{1}{2}}_{i,j,k+\frac{1}{2}} + (\Sigma^{x}_{xz})^{n-\frac{1}{2}}_{i,j,k+\frac{1}{2}}}{2} = \mu_{i,j,k+\frac{1}{2}}\frac{\partial(V_z)^{n}_{i,j,k+\frac{1}{2}}}{\partial x} \tag{A.33}$$

$$\frac{(\Sigma^{y}_{xz})^{n+\frac{1}{2}}_{i,j,k+\frac{1}{2}} - (\Sigma^{y}_{xz})^{n-\frac{1}{2}}_{i,j,k+\frac{1}{2}}}{\Delta t} + d^{y}_{j}\frac{(\Sigma^{y}_{xz})^{n+\frac{1}{2}}_{i,j,k+\frac{1}{2}} + (\Sigma^{y}_{xz})^{n-\frac{1}{2}}_{i,j,k+\frac{1}{2}}}{2} = 0 \tag{A.34}$$

$$\frac{(\Sigma^{z}_{xz})^{n+\frac{1}{2}}_{i,j,k+\frac{1}{2}} - (\Sigma^{z}_{xz})^{n-\frac{1}{2}}_{i,j,k+\frac{1}{2}}}{\Delta t} + d^{z}_{k+\frac{1}{2}}\frac{(\Sigma^{z}_{xz})^{n+\frac{1}{2}}_{i,j,k+\frac{1}{2}} + (\Sigma^{z}_{xz})^{n-\frac{1}{2}}_{i,j,k+\frac{1}{2}}}{2} = \mu_{i,j,k+\frac{1}{2}}\frac{\partial(V_x)^{n}_{i,j,k+\frac{1}{2}}}{\partial z} \tag{A.35}$$

$$(\Sigma_{yz})^{n+\frac{1}{2}}_{i+\frac{1}{2},j+\frac{1}{2},k+\frac{1}{2}} = (\Sigma^{x}_{yz})^{n+\frac{1}{2}}_{i+\frac{1}{2},j+\frac{1}{2},k+\frac{1}{2}} + (\Sigma^{z}_{yz})^{n+\frac{1}{2}}_{i+\frac{1}{2},j+\frac{1}{2},k+\frac{1}{2}} \tag{A.36}$$

$$\frac{(\Sigma^{x}_{yz})^{n+\frac{1}{2}}_{i+\frac{1}{2},j+\frac{1}{2},k+\frac{1}{2}} - (\Sigma^{x}_{yz})^{n-\frac{1}{2}}_{i+\frac{1}{2},j+\frac{1}{2},k+\frac{1}{2}}}{\Delta t} + d^{x}_{i+\frac{1}{2}}\frac{(\Sigma^{x}_{yz})^{n+\frac{1}{2}}_{i+\frac{1}{2},j+\frac{1}{2},k+\frac{1}{2}} + (\Sigma^{x}_{yz})^{n-\frac{1}{2}}_{i+\frac{1}{2},j+\frac{1}{2},k+\frac{1}{2}}}{2} = 0 \tag{A.37}$$

$$\begin{aligned}\frac{(\Sigma^{x}_{yz})^{n+\frac{1}{2}}_{i+\frac{1}{2},j+\frac{1}{2},k+\frac{1}{2}} - (\Sigma^{x}_{yz})^{n-\frac{1}{2}}_{i+\frac{1}{2},j+\frac{1}{2},k+\frac{1}{2}}}{\Delta t} + d^{j}_{i+\frac{1}{2}}\frac{(\Sigma^{x}_{yz})^{n+\frac{1}{2}}_{i+\frac{1}{2},j+\frac{1}{2},k+\frac{1}{2}} + (\Sigma^{x}_{yz})^{n-\frac{1}{2}}_{i+\frac{1}{2},j+\frac{1}{2},k+\frac{1}{2}}}{2} \\ = \mu_{i+\frac{1}{2},j+\frac{1}{2},k+\frac{1}{2}}\frac{\partial(V_z)^{n}_{i+\frac{1}{2},j+\frac{1}{2},k+\frac{1}{2}}}{\partial y}\end{aligned} \tag{A.38}$$

$$\begin{aligned}\frac{(\Sigma^{z}_{yz})^{n+\frac{1}{2}}_{i+\frac{1}{2},j+\frac{1}{2},k+\frac{1}{2}} - (\Sigma^{z}_{yz})^{n-\frac{1}{2}}_{i+\frac{1}{2},j+\frac{1}{2},k+\frac{1}{2}}}{\Delta t} + d^{z}_{k+\frac{1}{2}}\frac{(\Sigma^{z}_{yz})^{n+\frac{1}{2}}_{i+\frac{1}{2},j+\frac{1}{2},k+\frac{1}{2}} + (\Sigma^{z}_{yz})^{n-\frac{1}{2}}_{i+\frac{1}{2},j+\frac{1}{2},k+\frac{1}{2}}}{2} \\ = \mu_{i+\frac{1}{2},j+\frac{1}{2},k+\frac{1}{2}}\frac{\partial(V_y)^{n}_{i+\frac{1}{2},j+\frac{1}{2},k+\frac{1}{2}}}{\partial z}.\end{aligned} \tag{A.39}$$

A.1.2 Variables on the mesh.

Each variable is projected on the mesh with the following stencil scheme:

(i, j, k) : V_x, ρ, f_x

$(i+\frac{1}{2}, j+\frac{1}{2}, k)$: V_y, ρ, f_y

$(i+\frac{1}{2}, j, k+\frac{1}{2})$: V_z, ρ, f_z

$(i+\frac{1}{2}, j, k)$: Σ_{xx}, Σ_{zz}, Σ_{yy}, λ, μ

$(i, j+\frac{1}{2}, k)$: Σ_{xy}, μ

$(i, j, k+\frac{1}{2})$: Σ_{xz}, μ

$(i+\frac{1}{2}, j+\frac{1}{2}, k+\frac{1}{2})$: Σ_{yz}, μ.

The PLM finctions d_x, d_y, d_z are defined on each point on the staggered grid.

A.1.3 Calculation of spatial derivatives using the pseudo-spectral staggered grid

The spatial derivatives are calculated by spectral method according to Carcione (1999).

1. Apply FFT: $V_i \rightarrow \hat{V}_i$.
2. Multiply $\hat{V}_i$ by $jKe^{\pm j\frac{K}{2}dx} \rightarrow \tilde{V}_{i\pm\frac{1}{2}}$, where K is a wavenumber and $j = \sqrt{(-1)}$.
3. Apply inverse FFT: $\tilde{V}_{i\pm\frac{1}{2}} \rightarrow \frac{\partial V_{i\pm\frac{1}{2}}}{\partial x}$.

A.2 Explicit forms of $\nabla\nabla\cdot$ and $\nabla\times\nabla\times$

For any vector $\underline{u} = (u_x, u_y, u_z)$:

$$\nabla\nabla\cdot\underline{u} = \begin{pmatrix} \partial^2_{xx}u_x + \partial_x\partial_y u_y + \partial_x\partial_z u_z \\ \partial_y\partial_x u_x + \partial^2_{yy}u_y + \partial_y\partial_z u_z \\ \partial_z\partial_x u_x + \partial_z\partial_y u_y + \partial^2_{zz}u_z \end{pmatrix}, \tag{A.40}$$

and

$$\nabla \times \nabla \times u = \begin{pmatrix} \partial_y \partial_x u_y - \partial_{yy}^2 u_x + \partial_z \partial_x u_z - \partial_{zz}^2 u_x \\ \partial_x \partial_y u_x - \partial_{xx}^2 u_y + \partial_z \partial_y u_z - \partial_{zz}^2 u_y \\ \partial_x \partial_z u_x - \partial_{xx}^2 u_z + \partial_y \partial_z u_y - \partial_{yy}^2 u_z \end{pmatrix}, \tag{A.41}$$

where each derivative is calculated using the pseudo-spectral method, described above.

Appendix B

Derivation of the SICP-WEMVA

B.1 Maximum space-lag selection procedure

For choosing the optimal maximum space-lags, $\underline{H}$, we need to derive and solve another optimization problem. Although we do not solve the optimization problem explicitly, here we give a recipe for the simple selection of a nearly optimal $\underline{H}$. We reduce the space-lag 3D domain to 1D along the x direction and take the derivative of equation 4.7, the objective functional of SICP-WEMVA, with respect to maximum space-lags, H_x, using the finite difference approximation, and set it to zero as

$$\frac{\partial J}{\partial H_x} \approx \frac{1}{2\Delta H_x}\left(\int\int_{-H_{x_2}}^{H_{x_2}} h_x^2 I^2(\underline{x}, h_x) dh_x d\underline{x} - \int\int_{-H_{x_1}}^{H_{x_1}} h_x^2 I^2(\underline{x}, h_x) dh_x d\underline{x}\right) = 0, \tag{B.1}$$

where $\Delta H_x = H_{x_2} - H_{x_1}$. For the sake of simplicity we omit the dependence on $\underline{x}$, and by manipulating the limits of integration, Equation B.1 becomes

$$\frac{\partial J}{\partial H_x} \approx \frac{1}{2\Delta H_x}\left(\int_{H_{x_1}}^{H_{x_2}} h_x^2 I^2(h_x) dh_x - \int_{-H_{x_1}}^{-H_{x_2}} h_x^2 I^2(h_x) dh_x\right) = 0 \tag{B.2}$$

or

$$\frac{\partial J}{\partial H_x} \approx \frac{1}{2\Delta H_x}\left(\int_{H_{x_1}}^{H_{x_1}+\Delta H_x} h_x^2 I^2(h_x) dh_x - \int_{-H_{x_1}}^{-H_{x_1}-\Delta H_x} h_x^2 I^2(h_x) dh_x\right) = 0. \tag{B.3}$$

Thus, to obtain the nearly-optimal solution for H_x we calculate the integrals in equation B.3 solely between $-H_{x_1}$ and $-H_{x_1}-\Delta H_x$ and between H_{x_1} and $H_{x_1}+\Delta H_x$, which in general are small. We use the regula falsi algorithm (e.g., Stoer & Bulirsch, 2002, page 339) to iteratively solve equation B.3 to select the values of H_{x_1}.

B.2 Derivation of the sensitivity kernels for SICP-WEMVA

To derive the sensitivity kernels, $K_{\hat{\alpha}}$ and $K_{\hat{\beta}}$, we perturb the objective function (equation 4.7) and obtain

$$\delta J = \int\int \delta I(\underline{x},\underline{h}) R(\underline{x},\underline{h}) d\underline{x} d\underline{h}, \tag{B.4}$$

where $R(\underline{x},\underline{h}) = \underline{h}^2 I(\underline{x},\underline{h})$ and

$$\delta I(\underline{x},\underline{h}) = \sum_{j}^{N_e} \int \left(\delta\underline{\ddot{u}}_p^j(\underline{x}-\underline{h},t)\cdot\underline{\ddot{u}}_s^j(\underline{x}+\underline{h},t) + \underline{\ddot{u}}_p^j(\underline{x}-\underline{h},t)\cdot\delta\underline{\ddot{u}}_s^j(\underline{x}+\underline{h},t)\right) dt. \tag{B.5}$$

Substituting equation B.5 into equation B.4 yields

$$\delta J := \delta J_p + \delta J_s, \tag{B.6}$$

where

$$\delta J_p := \sum_{j}^{N_e} \int\int\int \left(\delta\underline{\ddot{u}}_p^j(\underline{x}-\underline{h},t)\cdot\underline{\ddot{u}}_s^j(\underline{x}+\underline{h},t)\right) R(\underline{x},\underline{h}) dt d\underline{x} d\underline{h} \tag{B.7}$$

and

$$\delta J_s := \sum_{j}^{N_e} \int\int\int \left(\underline{\ddot{u}}_p^j(\underline{x}-\underline{h},t)\cdot\delta\underline{\ddot{u}}_s^j(\underline{x}+\underline{h},t)\right) R(\underline{x},\underline{h}) dt d\underline{x} d\underline{h}. \tag{B.8}$$

To find $\delta\underline{\ddot{u}}_p^j$ and $\delta\underline{\ddot{u}}_s^j$ in equations B.7 and B.8, we perturb equation 4.4 and obtain:

$$\delta\underline{\ddot{u}}_p^j = \delta\hat{\alpha}\nabla\nabla\cdot\underline{u}^j + \hat{\alpha}\nabla\nabla\cdot\delta\underline{u}^j \tag{B.9}$$

and

$$\delta\underline{\ddot{u}}_s^j = -\delta\hat{\beta}\nabla\times\nabla\times\underline{u}^j - \hat{\beta}\nabla\times\nabla\times\delta\underline{u}^j, \tag{B.10}$$

both of which depend on $\delta\underline{u}^j$. To evaluate $\delta\underline{u}^j$, we consider equation 4.2 with any input source function $\underline{f}$ as a linear system given as

$$L\underline{u}^j = \underline{f}, \tag{B.11}$$

where L is the isotropic elastic wave operator defined as

$$L = \hat{\alpha}\nabla\nabla\cdot - \hat{\beta}\nabla\times\nabla\times - \partial_t^2. \tag{B.12}$$

By perturbing equation B.11 we obtain

$$\delta L\underline{u}^j + L\delta\underline{u}^j = 0, \tag{B.13}$$

or

$$\delta\underline{u}^j = -L^{-1}\delta L\underline{u}^j. \tag{B.14}$$

The perturbation of the modeling operator, L, is

$$\delta L = \delta\hat{\alpha}\,(\nabla\nabla\cdot) - \delta\hat{\beta}\,(\nabla\times\nabla\times)\,, \tag{B.15}$$

which turns equation B.14 into

$$\delta\underline{u}^j = -L^{-1}(\delta\hat{\alpha}\frac{\underline{\ddot{u}}_p^j}{\hat{\alpha}} + \delta\hat{\beta}\frac{\underline{\ddot{u}}_s^j}{\hat{\beta}}), \tag{B.16}$$

where $\frac{\underline{\ddot{u}}_p^j}{\hat{\alpha}} = \nabla\nabla\cdot\underline{u}^j$ and $\frac{\underline{\ddot{u}}_s^j}{\hat{\beta}} = -\nabla\times\nabla\times\underline{u}^j$ (see equation 4.4).

Substituting equation B.16 into equations B.9 and B.10 yields

$$\delta\underline{\ddot{u}}_p^j = \frac{\delta\hat{\alpha}}{\hat{\alpha}}\underline{\ddot{u}}_p^j - \hat{\alpha}\nabla\nabla\cdot L^{-1}(\frac{\delta\hat{\alpha}}{\hat{\alpha}}\underline{\ddot{u}}_p^j + \frac{\delta\hat{\beta}}{\hat{\beta}}\underline{\ddot{u}}_s^j) \tag{B.17}$$

and

$$\delta\ddot{\underline{u}}_s^j = \delta\hat{\beta}\frac{\ddot{\underline{u}}_s^j}{\hat{\beta}} + \hat{\beta}\nabla\times\nabla\times L^{-1}\left(\delta\hat{\alpha}\frac{\ddot{\underline{u}}_p^j}{\hat{\alpha}} + \delta\hat{\beta}\frac{\ddot{\underline{u}}_s^j}{\hat{\beta}}\right). \tag{B.18}$$

Since model parameters $\hat{\alpha}$ and $\hat{\beta}$ are smooth, we assume that the perturbation in P- and S-wavefields are not affected by perturbations in S- and P-wave speeds, respectively. Thus, we can drop the $\delta\hat{\beta}$ term in $\delta\ddot{\underline{u}}_p^j$ and the $\delta\hat{\alpha}$ term in $\delta\ddot{\underline{u}}_s^j$ to obtain

$$\delta\ddot{\underline{u}}_p^j = \frac{\delta\hat{\alpha}}{\hat{\alpha}}\ddot{\underline{u}}_p^j - \hat{\alpha}\nabla\nabla\cdot L^{-1}\frac{\delta\hat{\alpha}}{\hat{\alpha}}\ddot{\underline{u}}_p^j, \tag{B.19}$$

and

$$\delta\ddot{\underline{u}}_s^j = \frac{\delta\hat{\beta}}{\hat{\beta}}\ddot{\underline{u}}_s^j + \hat{\beta}\nabla\times\nabla\times L^{-1}\frac{\delta\hat{\beta}}{\hat{\beta}}\ddot{\underline{u}}_s^j. \tag{B.20}$$

Next, we substitute equations B.19 into B.7 and obtain

$$\begin{aligned}
\delta J_p =& \sum_j^{N_e}\int\int\int\left(\frac{\delta\hat{\alpha}(\underline{x}-\underline{h})}{\hat{\alpha}(\underline{x}-\underline{h})}\ddot{\underline{u}}_p^j(\underline{x}-\underline{h},t) - \hat{\alpha}(\underline{x}-\underline{h})\nabla\nabla\cdot L^{-1}\frac{\delta\hat{\alpha}(\underline{x}-\underline{h})}{\hat{\alpha}(\underline{x}-\underline{h})}\ddot{\underline{u}}_p^j(\underline{x}-\underline{h},t)\right)\\
&\cdot\left(\ddot{\underline{u}}_s^j(\underline{x}+\underline{h},t)R(\underline{x},\underline{h})\right)dtd\underline{x}d\underline{h}\\
=& \sum_j^{N_e}\int\int\int\frac{\delta\hat{\alpha}(\underline{x}-\underline{h})}{\hat{\alpha}(\underline{x}-\underline{h})}\ddot{\underline{u}}_p^j(\underline{x}-\underline{h},t)\cdot\ddot{\underline{u}}_s^j(\underline{x}+\underline{h},t)R(\underline{x},\underline{h})dtd\underline{h}d\underline{x}\\
&-\sum_j^{N_e}\int\int\int\left(\hat{\alpha}(\underline{x}-\underline{h})\nabla\nabla\cdot L^{-1}\frac{\delta\hat{\alpha}(\underline{x}-\underline{h})}{\hat{\alpha}(\underline{x}-\underline{h})}\ddot{\underline{u}}_p^j(\underline{x}-\underline{h},t)\right)\\
&\cdot\left(\ddot{\underline{u}}_s^j(\underline{x}+\underline{h},t)R(\underline{x},\underline{h})\right)dtd\underline{x}d\underline{h}.
\end{aligned} \tag{B.21}$$

In the second sum/integral we recognize an inner product and so we can replace it with an adjoint operator (i.e., $\left(\hat{\alpha}\nabla\nabla\cdot L^{-1}\right)^* = (L^{-1})^*\nabla\nabla\cdot\hat{\alpha}$, where superscript $*$ refers to adjoint) in order to isolate $(\delta\hat{\alpha})/\hat{\alpha}$:

$$\begin{aligned}
\delta J_p =& \sum_j^{N_e}\int\int\int\frac{\delta\hat{\alpha}(\underline{x}-\underline{h})}{\hat{\alpha}(\underline{x}-\underline{h})}\ddot{\underline{u}}_p^j(\underline{x}-\underline{h},t)\cdot\ddot{\underline{u}}_s^j(\underline{x}+\underline{h},t)R(\underline{x},\underline{h})dtd\underline{h}d\underline{x}\\
&-\sum_j^{N_e}\int\int\int\frac{\delta\hat{\alpha}(\underline{x}-\underline{h})}{\hat{\alpha}(\underline{x}-\underline{h})}\ddot{\underline{u}}_p^j(\underline{x}-\underline{h},t)\\
&\cdot\left((L^{-1})^*\nabla\nabla\cdot\hat{\alpha}(\underline{x}-\underline{h})\ddot{\underline{u}}_s^j(\underline{x}+\underline{h},t)R(\underline{x},\underline{h})\right)dtd\underline{h}d\underline{x}.
\end{aligned} \tag{B.22}$$

To make the second integral computationally efficient and integrate over $\underline{h}$ only once before applying the adjoint operator, we apply a shift in spatial coordinates (e.g., Shen, 2004), and obtain

$$
\begin{aligned}
\delta J_p &= \int \frac{\delta\hat{\alpha}(\underline{x})}{\hat{\alpha}(\underline{x})} \left(\sum_j^{N_e} \int\int \underline{\ddot{u}}_p^j(\underline{x},t) \cdot \underline{\ddot{u}}_s^j(\underline{x}+2\underline{h},t) R(\underline{x}+\underline{h},\underline{h}) dt d\underline{h} \right) d\underline{x} \\
&- \int \frac{\delta\hat{\alpha}(\underline{x})}{\hat{\alpha}(\underline{x})} \\
&\left(\sum_j^{N_e} \int \underline{\ddot{u}}_p^j(\underline{x},t) \cdot \left((L^{-1})^* \nabla\nabla \cdot \left\{ \int \hat{\alpha}(\underline{x}) \underline{\ddot{u}}_s^j(\underline{x}+2\underline{h},t) R(\underline{x}+\underline{h},\underline{h}) d\underline{h} \right\} \right) dt \right) d\underline{x} \\
&= \int \frac{\delta\hat{\alpha}(\underline{x})}{\hat{\alpha}(\underline{x})} \left(\sum_j^{N_e} \int\int \underline{\ddot{u}}_p^j(\underline{x},t) \cdot \underline{\ddot{u}}_s^j(\underline{x}+2\underline{h},t) R(\underline{x}+\underline{h},\underline{h}) dt d\underline{h} \right) d\underline{x} \\
&- \int \frac{\delta\hat{\alpha}(\underline{x})}{\hat{\alpha}(\underline{x})} \left(\sum_j^{N_e} \int_T^0 \underline{\ddot{u}}_p^j(\underline{x},t) \cdot \underline{v}_p^j(\underline{x},T-t) dt \right) d\underline{x} \\
&:= \int \delta\hat{\alpha}(\underline{x}) \left(K_{\hat{\alpha}}^D(\underline{x}) + K_{\hat{\alpha}}^A(\underline{x}) \right) d\underline{x}.
\end{aligned}
\tag{B.23}
$$

The sensitivity kernels in the first and second integrals are denoted by $K_{\hat{\alpha}}^D$ and $K_{\hat{\alpha}}^A$, where the superscripts D and A refer to *direct* and *adjoint*, respectively, based on their computation procedure (i.e., for the *direct* term, adjoint wavefield is not calculated). Note that in our experience with the examples above $K_{\hat{\alpha}}^D$ is significantly smaller than $K_{\hat{\alpha}}^A$ and thus are dropped. We therefore use $K_{\hat{\alpha}}^A$ for the sensitivity kernel used in equation 4.9. However, if $K_{\hat{\alpha}}^A$ is not small it might underestimate the gradient calculation.

Similarly we substitute equations B.20 into B.8 to derive δJ_s:

$$
\begin{aligned}
\delta J_s =& \sum_j^{N_e} \int\int\int \underline{\ddot{u}}_p^j(\underline{x}-\underline{h},t)\cdot\frac{\delta\hat{\beta}(\underline{x}+\underline{h})}{\hat{\beta}(\underline{x}+\underline{h})}\underline{\ddot{u}}_s^j(\underline{x}+\underline{h},t)dtR(\underline{x},\underline{h})d\underline{x}d\underline{h}\\
&+\sum_j^{N_e} \int\int\int \left(\underline{\ddot{u}}_p^j(\underline{x}-\underline{h},t)\cdot\hat{\beta}(\underline{x}+\underline{h})\nabla\times\nabla\times L^{-1}\frac{\delta\hat{\beta}(\underline{x}+\underline{h})}{\hat{\beta}(\underline{x}+\underline{h})}\underline{\ddot{u}}_s(\underline{x}+\underline{h},t)\right)R(\underline{x},\underline{h})dtd\underline{x}d\underline{h}\\
&=\sum_j^{N_e} \int\int\int \frac{\delta\hat{\beta}(\underline{x}+\underline{h})}{\hat{\beta}(\underline{x}+\underline{h})}\underline{\ddot{u}}_p^j(\underline{x}-\underline{h},t)\cdot\underline{\ddot{u}}_s^j(\underline{x}+\underline{h},t)dtR(\underline{x},\underline{h})d\underline{x}d\underline{h}\\
&+\sum_j^{N_e} \int\int\int \frac{\delta\hat{\beta}(\underline{x}+\underline{h})}{\hat{\beta}(\underline{x}+\underline{h})}\left(\left(L^{-1}\right)^*\nabla\times\nabla\times\hat{\beta}(\underline{x}+\underline{h})\underline{\ddot{u}}_p^j(\underline{x}-\underline{h},t)R(\underline{x},\underline{h})\right)\\
&\cdot\underline{\ddot{u}}_s^j(\underline{x}+\underline{h},t)dtd\underline{x}d\underline{h}\\
&=\int\frac{\delta\hat{\beta}(\underline{x})}{\hat{\beta}(\underline{x})}\sum_j^{N_e}\int\int\underline{\ddot{u}}_p^j(\underline{x}-2\underline{h},t)\cdot\underline{\ddot{u}}_s^j(\underline{x},t)dtR(\underline{x}-\underline{h},\underline{h})d\underline{x}d\underline{h}\\
&+\int\frac{\delta\hat{\beta}(\underline{x})}{\hat{\beta}(\underline{x})}\sum_j^{N_e}\int\left(\left(L^{-1}\right)^*\nabla\times\nabla\times\left\{\int\hat{\beta}(\underline{x})\underline{\ddot{u}}_p^j(\underline{x}-2\underline{h},t)R(\underline{x}-\underline{h},\underline{h})d\underline{h}\right\}\right)\\
&\cdot\underline{\ddot{u}}_s^j(\underline{x},t)dtd\underline{x}\\
&=\int\frac{\delta\hat{\beta}(\underline{x})}{\hat{\beta}(\underline{x})}\sum_j^{N_e}\int\int\underline{\ddot{u}}_p^j(\underline{x}-2\underline{h},t)\cdot\underline{\ddot{u}}_s^j(\underline{x},t)dtR(\underline{x}-\underline{h},\underline{h})d\underline{x}d\underline{h}\\
&+\int\frac{\delta\hat{\beta}(\underline{x})}{\hat{\beta}(\underline{x})}\sum_j^{N_e}\int_T^0\underline{v}_s^j(\underline{x},T-t)\cdot\underline{\ddot{u}}_s^j(\underline{x},t)dtd\underline{x}:=\int\delta\hat{\beta}(\underline{x})\left(K_{\hat{\beta}}^D(\underline{x})+K_{\hat{\beta}}^A(\underline{x})\right)d\underline{x}.
\end{aligned}
\tag{B.24}
$$

As for $K_{\hat{\alpha}}(\underline{x})$, the sensitivity kernel, $K_{\hat{\beta}}(\underline{x})$, given in equation 4.10, is simply $K_{\hat{\beta}}^A(\underline{x})$, and $K_{\hat{\beta}}^D(\underline{x})$ is dropped because of being significantly small in the examples above. However the effect of the *direct* terms on the full sensitivity kernels requires further investigation.

B.3 An efficient calculation of the step length for SICP-WEMVA optimization

To find an optimal step length, ν, for the gradient-based optimization in equation 4.15, we need to choose a step length that will set to zero the derivative of the objective functional with respect to the step length. In other words, if

$$J(\nu_{i_k}) = J(\underline{m}_{i+1}) = J(\underline{m}_i + \nu_{i_k}\underline{p}_i),$$

then

$$\frac{\partial J}{\partial \nu_{i_k}}(\nu_{optimal}) = \frac{\partial J}{\partial \underline{m}_{i+1}} \cdot \frac{\partial \underline{m}_{i+1}}{\partial \nu_{i_k}} = \underline{g}_{i_k} \cdot \underline{p}_i = 0. \tag{B.25}$$

One way to find the optimal ν's is to use the line search method: start with an initial guess and use the bisection method (e.g., Rodi & Mackie, 2001) or the regula falsi algorithm for iterative update of ν, such that equation B.25 is satisfied. To satisfy this equation we need to calculate gradient, $\underline{g}_{i_k}$, at each iteration of the line search along a given search direction. Hence the calculation of each gradient (in SICP-WEMVA) is accomplished with two propagations in equations 4.9 and 4.10. We propose a faster way to calculate the ν's without calculating the gradient at each iteration; we calculate the objective functional for two consecutive ν's (from either initial guesses or bisection method) with only one propagation and then calculate the derivative of equation B.25 using the finite difference approximation as

$$\frac{\partial J}{\partial \nu_{i_k}} = \frac{J(\nu_{i_k}) - J(\nu_{i_{k-1}})}{\nu_{i_k} - \nu_{i_{k-1}}} = 0. \tag{B.26}$$

Note that for equation B.26, we calculate the gradient solely when we define a new search direction.

Appendix C

Analytical derivation of the elastic wave speed sensitivity for the SICP-WEMVA

C.1 Sensitivity of the SICP-WEMVA moveouts to wave speed variations

In this appendix, we present an analytical derivation of the sensitivity of the moveouts in the extended space-lag domain common image gather, discussed in section 4.3.1 for SICP-WEMVA. Our derivation starts with equations for travel times between a conversion point in the subsurface and recordings of the P- and S-waves at two receivers at the surface (see Figure C-1). The travel time for the P-wave is given as

$$t_p = \frac{d_p}{\alpha_0} = \frac{\sqrt{(x_p - x_0)^2 + z_0^2}}{\alpha_0} = \frac{\sqrt{(x_s + dx - x_0)^2 + z_0^2}}{\gamma_0 \beta_0}, \tag{C.1}$$

and for the S-wave as

$$t_s = \frac{d_s}{\beta_0} = \frac{\sqrt{(x_s - x_0)^2 + z_0^2}}{\beta_0}, \tag{C.2}$$

where d_p and d_s, are the P- and S-wave distances, α_0 and β_0 are the **true** P- and S-wave speeds, and γ_0 is their ratio (i.e., $\gamma_0 = \alpha_0/\beta_0$). The distance between two receivers is $dx = x_p - x_s$.

The extended SICP imaging condition, given in section 4.3.1, for a single source is:

$$I(x_0, h_x, z) = \int_T^0 \underline{\ddot{u}}_p(x_0 + h_x, z, t) \cdot \underline{\ddot{u}}_s(x_0 - h_x, z, t)dt, \tag{C.3}$$

where $I(x_0, h_x, z)$ is the extended image (i.e., common image gather), and $\underline{\ddot{u}}_p$ and $\underline{\ddot{u}}_s$ are the acceleration wavefields. Note that $z = z_0 \pm \delta z$ where δz is defined within the bars in Figure C-2.

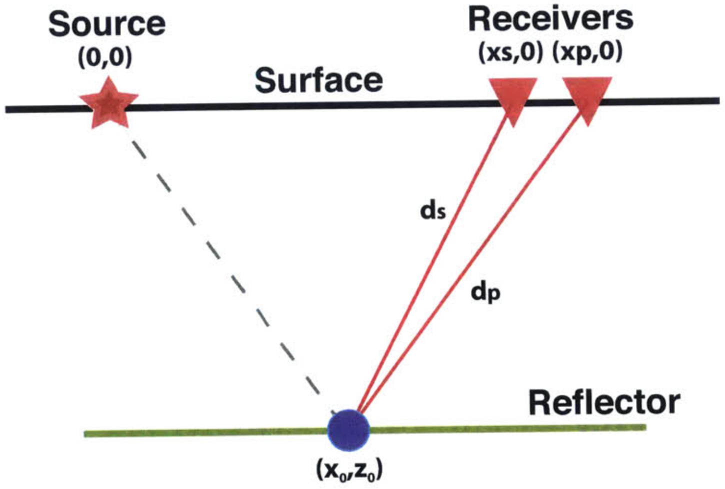

Figure C-1: The path of the interfering P- and S-waves from a conversion point in the subsurface with two receivers at the surface.

Since the wavefields $\underline{\ddot{u}}_p$ and $\underline{\ddot{u}}_s$ propagate using the **migration** wave speeds, α_1, β_1 and $\gamma_1 = \alpha_1/\beta_1$, we analyze the interference of the wavefields in the horizontal space-lag extended image point (gather) by shifting the S-wave by h to the left (i.e., $-h$) and the P-wave by h to the right (i.e., $+h$) and keeping the same propagation travel times as those given in equations C.1 and C.2 (see Figure C-2(a)). We now compute the travel times for the migration wave speeds. For the P-wave travel time, we obtain,

$$t_p = \frac{\sqrt{(x_s + dx - x_0 - h_x)^2 + z^2}}{\gamma_1 \beta_1}, \tag{C.4}$$

and for the S-wave,

$$t_s = \frac{\sqrt{(x_s - x_0 + h_x)^2 + z^2}}{\beta_1}. \tag{C.5}$$

Then, we enforce that these travel times are equal to the recorded times. For the P-wave, we equate equations C.1 and C.4, and obtain:

$$(x_s + dx - x_0)^2 + z_0^2 = \left(\frac{\gamma_0\beta_0}{\gamma_1\beta_1}\right)^2 \left[(x_s + dx - x_0 - h_x)^2 + z^2\right], \tag{C.6}$$

or

$$(x_s - x_0)^2 + z_0^2 = \left(\frac{\gamma_0\beta_0}{\gamma_1\beta_1}\right)^2 \left[(x_s + dx - x_0 - h_x)^2 + z^2\right] - 2(x_s - x_0)dx - (dx)^2, \tag{C.7}$$

and by equating equations C.2 and C.5, we obtain:

$$(x_s - x_0)^2 + z_0^2 = \left(\frac{\beta_0}{\beta_1}\right)^2 \left[(x_s - x_0 + h_x)^2 + z^2\right]. \tag{C.8}$$

Next, we equate equations C.7 with C.8, and obtain,

$$\left(\frac{\gamma_0\beta_0}{\gamma_1\beta_1}\right)^2 \left[(x_s + dx - x_0 - h_x)^2 + z^2\right] - 2(x_s - x_0)dx - (dx)^2 = \left(\frac{\beta_0}{\beta_1}\right)^2 \left[(x_s - x_0 + h_x)^2 + z^2\right], \tag{C.9}$$

and after several rearrangement steps, we obtain:

$$z^2 = \frac{(x_s - x_0 + h_x)^2 - \left(\frac{\gamma_0}{\gamma_1}\right)^2 (x_s + dx - x_0 - h_x)^2 + \left(\frac{\beta_1}{\beta_0}\right)^2 (2(x_s - x_0)dx + (dx)^2)}{\left(\left(\frac{\gamma_0}{\gamma_1}\right)^2 - 1\right)}, \tag{C.10}$$

or

$$z = \sqrt{\frac{(x_s - x_0 + h_x)^2 - \left(\frac{\gamma_0}{\gamma_1}\right)^2 (x_s + dx - x_0 - h_x)^2 + \left(\frac{\beta_1}{\beta_0}\right)^2 (2(x_s - x_0)dx + (dx)^2)}{\left(\left(\frac{\gamma_0}{\gamma_1}\right)^2 - 1\right)}}. \tag{C.11}$$

This equation shows how the depth, z, of the moveout changes as a function of the horizontal space lag, h_x, for a fixed ratio between the true and migration S-wave speeds, β_0/β_1, and the ratio between the true and migration P- to S- wave speed ratio, γ_0/γ_1, the subsurface horizontal position x_0, the surface position of the S-wave receiver, x_s, and its distance to the P-wave receiver, dx. Note that the equations C.10 and C.11 are not well defined when $\gamma_0 = \gamma_1$.

The same procedure is applied for analyzing the inference when we shift the S-wave by h to the right (i.e., $+h$) and the P-wave by h to the left (i.e., $-h$) (see Figure C-2(b). The final equation for this case is

$$z = \sqrt{\frac{(x_s - x_0 - h_x)^2 - \left(\frac{\gamma_0}{\gamma_1}\right)^2 (x_s + dx - x_0 + h_x)^2 + \left(\frac{\beta_1}{\beta_0}\right)^2 (2(x_s - x_0)dx + (dx)^2)}{\left(\left(\frac{\gamma_0}{\gamma_1}\right)^2 - 1\right)}}. \tag{C.12}$$

C.2 Plots of the SICP-WEMVA sensitivity moveouts

To show the behavior of the moveout, $z(h)$, in equations C.11 and C.12, we plot them in Figure C-3 for a fixed $x_0 = 2000\ m$ and $x_s = 4000\ m$, and for five varying dx values between 600 m and 3000 m. The blue color corresponds to equation C.11 and green color to equation C.12. The big red dot marks the interference point where all energy will constructively interfere by adding more moveouts from different values of dx. Three main observations can be deduced from this Figure. First, we observe constructive interference for different values of dx that correspond implicitly to different numbers of shots (earthquakes). Second, although the depth in Figure C-3(a) for $\gamma_0/\gamma_1 = 1.000001$ is unrealistic because the equations C.11 and C.12 are not well-defined, constructive interference occurs at $h_x = 0\ m$ for correct wave speed models, as was shown in Figure 4-3(d) (note that this is a limitation of the analytical derivation, not of the underlying theory of SICP-WEMVA). Third, when the ratios

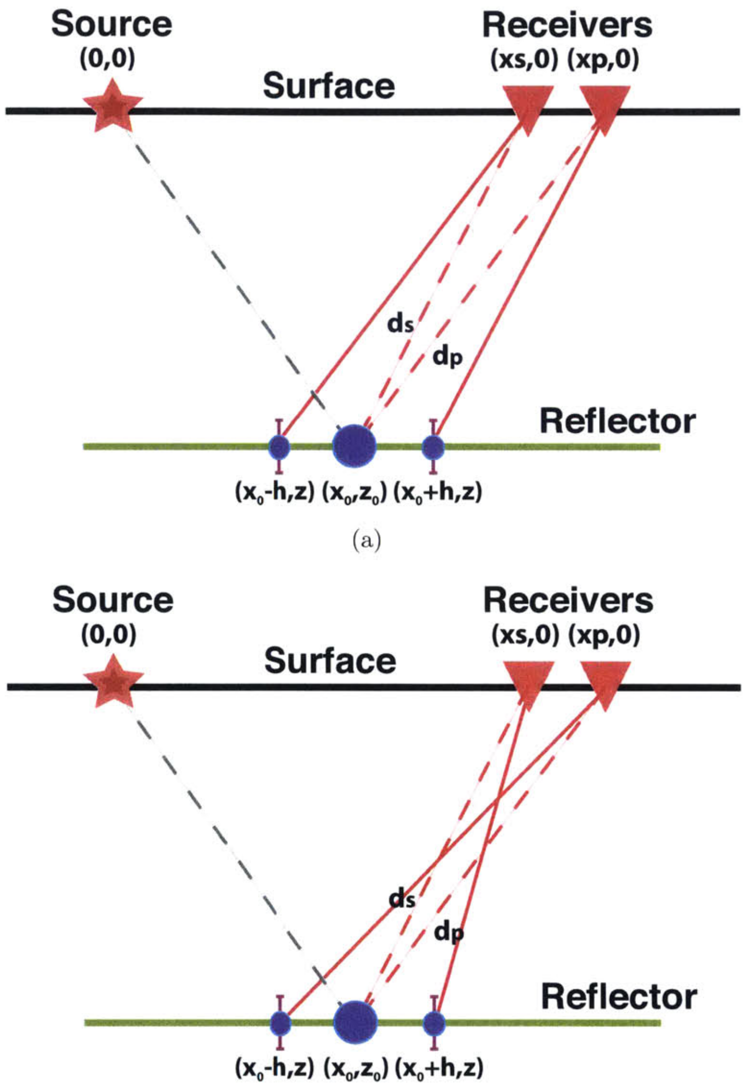

(a)

(b)

Figure C-2: The paths of the interfering P- and S-waves for the extended horizontal space-lag imaging condition: (a) shifting P-wave to $x_0 + h$ and S-wave to $x_0 - h$, (b) shifting P-wave to $x_0 - h$ and S-wave to $x_0 + h$. The bars at the points $(x_0 - h, z)$ and $(x_0 + h, z)$ indicate that the interference is depth dependent.

of β and γ increase and decrease on the same scale, the constructive interference can also occur at $h_x = 0\ m$ (see Figures C-3(e) and C-3(f)), and then the SICP-WEMVA might stop updating the wave-speeds. However, although this effect might exist, the range of S-wave speed variation is generally not on the same order as that for the P- to S-wave ratios.

In Figure C-4, we show the squared depths of the moveout, $z^2(h)$. Note that the moveouts for $z^2(h)$ are linear in contrast to elliptical moveout for $z(h)$ as shown in Figure C-3. Although the same observations apply for $z^2(h)$ as were given for $z(h)$, the stability and convergence of the SICP-WEMVA may be considerably different if the moveout is constructed as a function of $z^2(h)$. This is a subject of future research.

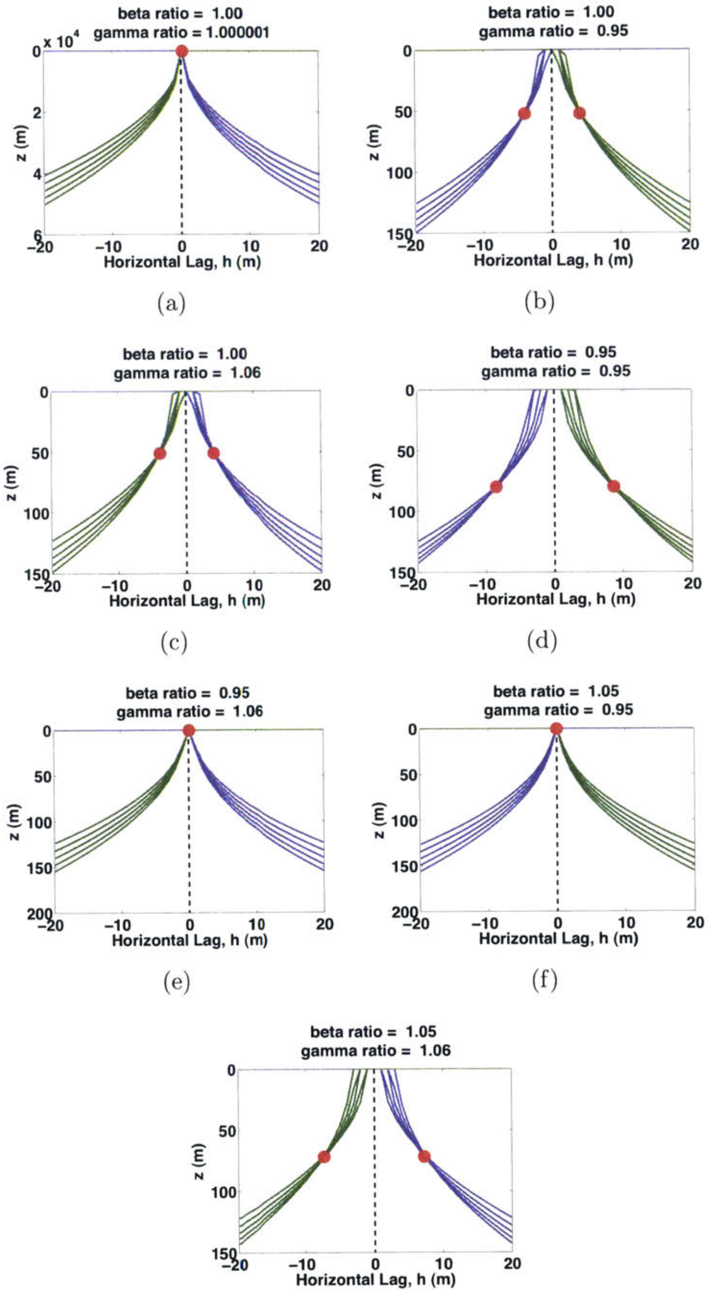

(a) (b)

(c) (d)

(e) (f)

(g)

Figure C-3: Interference between moveouts in the z-h plane for SICP-WEMVA as a function of dx for a fixed β_0/β_1 and γ_0/γ_1. The zone of constructive interference is marked with the red dot.

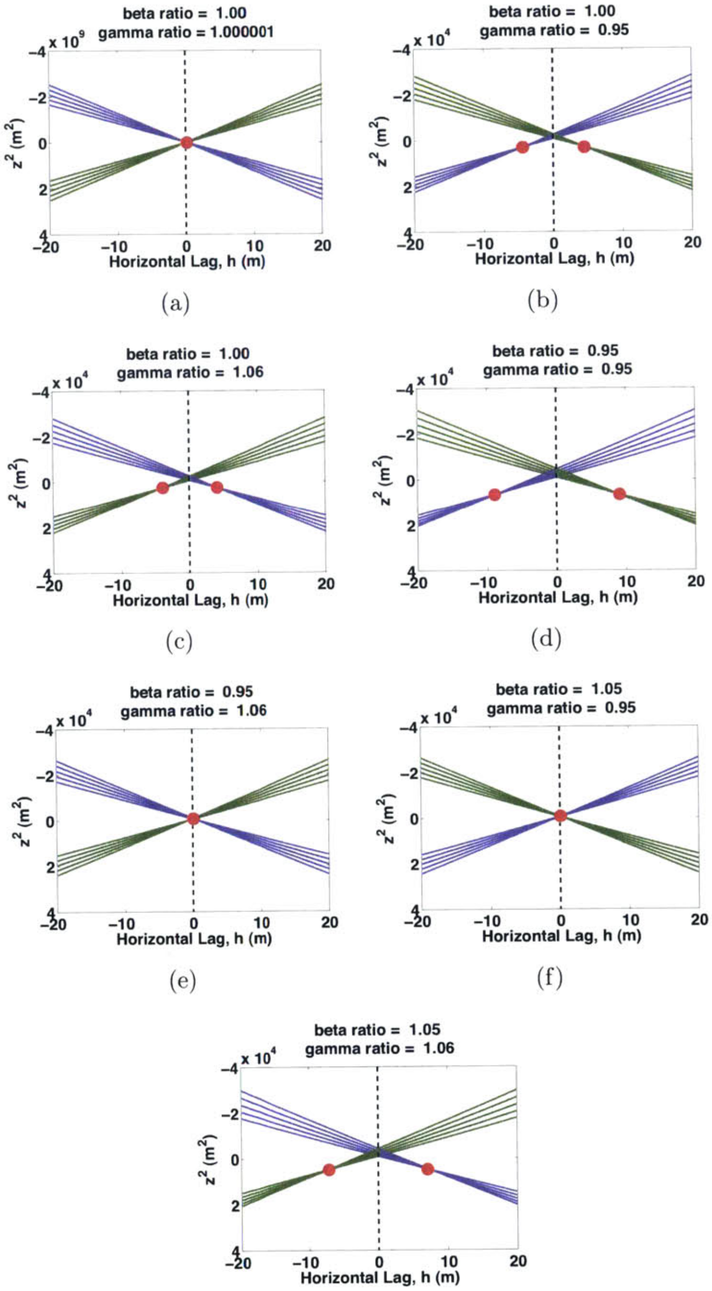

(a) (b) (c) (d) (e) (f) (g)

Figure C-4: Interference between moveouts in the z^2-h plane for SICP-WEMVA as a function of dx for a fixed β_0/β_1 and γ_0/γ_1. The zone of constructive interference is marked with the red dot.

Bibliography

Abma, R. & Kabir, N., 2006. 3d interpolation of irregular data with a pocs algorithm, *Geophysics*, **71**(6), E91–E97.

Aki, K. & Richards, P. G., 2002. *Quantitative seismology, Theory and Methods*, University Science Books, 2nd edn.

Albertin, U., Sava, P., Etgen, J., & Maharramov, M., 2006. Adjoint wave-equation velocity analysis, *SEG Expanded Abstracts*, pp. 1–5.

Alkhalifah, T., Fomel, S., et al., 2001. The space–time domain: theory and modelling for anisotropic media, *Geophysical Journal International*, **144**(1), 105–113.

Árnason, K., Karlsdóttir, R., Eysteinsson, H., Flóvenz, Ó. G., & Gudlaugsson, S. T., 2000. The resistivity structure of high-temperature geothermal systems in iceland, in *Proceedings of the World Geothermal Congress 2000, Kyushu-Tohoku, Japan*, pp. 923–928.

Árnason, K., Eysteinsson, H., & Hersir, G. P., 2010. Joint 1d inversion of tem and mt data and 3d inversion of mt data in the hengill area, sw iceland, *Geothermics*, **39**(1), 13–34.

Batir, J., Davatzes, N. C., & Asmundsson, R., 2012. Preliminary model of fracture and stress state in the hellisheidi geothermal field, hengill volcanic system, iceland, in *Thirty-Seventh Workshop on Geothermal Reservoir Engineering, Stanford University, Stanford, California*, p. 18.

Baysal, E., Kosloff, D. D., & Sherwood, J., 1983. Reverse time migration, *Geophysics*, **48**(11), 1514–1524.

Berenger, J.-P., 1994. A perfectly matched layer for the absorption of electromagnetic waves, *Journal of computational physics*, **114**(2), 185–200.

Beylkin, G., 1985. Imaging of discontinuities in the inverse scattering problem by inversion of a causal generalized radon transform, *Journal of Mathematical Physics*, **26**(1), 99–108.

Biondi, B. & Sava, P., 1999. Wave-equation migration velocity analysis, *SEG Expanded Abstracts*, pp. 1723–1726.

Bleistein, N., 1987. On the imaging of reflectors in the earth, *Geophysics*, **52**(7), 931–942.

Bleistein, N. & Jaramillo, H., 2000. A platform for kirchhoff data mapping in scalar models of data acquisition, *Geophysical Prospecting*, **48**(1), 135–162.

Bleistein, N., Cohen, J., K., & Hagin, F., G., 1987. Two and one half dimensional Born inversion with an arbitrary reference, *Geophysics*, **52**, 26–36.

Bording, R. P., Gersztenkorn, A., Lines, L. R., Scales, J. A., & Treitel, S., 1987. Applications of seismic travel-time tomography, *Geophysical Journal International*, **90**(2), 285–303.

Bostock, M., Rondenay, S., & Shragge, J., 2001. Multiparameter two-dimensional inversion of scattered teleseismic body waves 1. theory for oblique incidence, *Journal of Geophysical Research: Solid Earth (1978–2012)*, **106**(B12), 30771–30782.

Brytic, V., de Hoop, M. V., & van der Hilst, R. D., 2012. Elastic-wave inverse scattering based on reverse time migration with active and passive source reflection data, *Inverse Problems and Applications: Inside Out II*, **60**, 411.

Carcione, J., 1999. Staggered mesh for the anisotropic and viscoelastic wave equation, *Geophysics*, **64**, 1863–1866.

Cerjan, C., Kosloff, D., Kosloff, R., & Reshef, M., 1985. A nonreflecting boundary condition for discrete acoustic and elastic wave equations, *Geophysics*, **50**(4), 705–708.

Chang, W.-F. & McMechan, G. A., 1986. Reverse-time migration of offset vertical seismic profiling data using the excitation-time imaging condition, *Geophysics*, **51**(1), 67–84.

Chang, W.-F. & McMechan, G. A., 1994. 3-d elastic prestack, reverse-time depth migration, *Geophysics*, **59**(4), 597–609.

Chattopadhyay, S. & McMechan, G. A., 2008. Imaging conditions for prestack reverse-time migration, *Geophysics*, **73**(3), S81–S89.

Claerbout, J. F., 1971. Toward a unified theory of reflector mapping, *Geophysics*, **36**(3), 467–481.

Claerbout, J. F., 1982. Imaging the earth's interior.

Clayton, R. & Engquist, B., 1977. Absorbing boundary conditions for acoustic and elastic wave equations, *Bulletin of the Seismological Society of America*, **67**(6), 1529–1540.

Collino, F. & Tsogka, C., 2001. Application of the perfectly matched absorbing layer model to the linear elastodynamic problem in anisotropic heterogeneous media, *Geophysics*, **66**(1), 294–307.

Curry, W., 2010. Interpolation with fourier-radial adaptive thresholding, *Geophysics*, **75**(6), WB95–WB102.

Dellinger, J. & Etgen, J., 1990. Wave-field separation in two-dimensional anisotropic media, *Geophysics*, **55**(7), 914–919.

Dong, S., Cai, J., Guo, M., Suh, S., Zhang, Z., Wang, B., Li, Z., et al., 2012. Least-squares reverse time migration: Towards true amplitude imaging and improving the resolution, in *2012 SEG Annual Meeting*, Society of Exploration Geophysicists.

Du, Q., Zhu, Y., & Ba, J., 2012. Polarity reversal correction for elastic reverse time migration, *Geophysics*, **77**(2), S31–S41.

Duquet, B., Marfurt, K. J., & Dellinger, J. A., 2000. Kirchhoff modeling, inversion for reflectivity, and subsurface illumination, *Geophysics*, **65**(4), 1195–1209.

Esmersoy, C., 1990. Inversion of p and sv waves from multicomponent offset vertical seismic profiles, *Geophysics*, **55**(1), 39–50.

Evans, J. R., Foulger, G., Julian, B. R., & Miller, A. D., 1996. Crustal shear-wave splitting from local earthquakes in the hengill triple junction, southwest iceland, *Geophysical research letters*, **23**(5), 455–458.

Farra, V. & Madariaga, R., 1988. Non-linear reflection tomography, *Geophysical Journal International*, **95**(1), 135–147.

Fei, W. & Williamson, P., 2010. On the gradient artifacts in migration velocity analysis based on differential semblance optimization, in *SEG, Expanded Abstracts*, vol. 29, pp. 4071–4076.

Fichtner, A., Bleibinhaus, F., & Capdeville, Y., 2011. *Full seismic waveform modelling and inversion*, Springer.

Fomel, S., 2003. Seismic reflection data interpolation with differential offset and shot continuation, *Geophysics*, **68**(2), 733–744.

Foulger, G., 1988a. Hengill triple junction, sw iceland 1. tectonic structure and the spatial and temporal distribution of local earthquakes, *Journal of Geophysical Research: Solid Earth (1978–2012)*, **93**(B11), 13493–13506.

Foulger, G., 1988b. Hengill triple junction, sw iceland 2. anomalous earthquake focal mechanisms and implications for process within the geothermal reservoir and at accretionary plate boundaries, *Journal of Geophysical Research: Solid Earth (1978–2012)*, **93**(B11), 13507–13523.

Foulger, G. & Toomey, D., 1989. Structure and evolution of the hengill-grensdalur volcanic complex, iceland: Geology, geophysics, and seismic tomography, *Journal of Geophysical Research: Solid Earth (1978–2012)*, **94**(B12), 17511–17522.

Foulger, G. R. & Julian, B. R., 1993. Non-double-couple earthquakes at the hengill-grensdalur volcanic complex, iceland: Are they artifacts of crustal heterogeneity?, *Bulletin of the Seismological Society of America*, **83**(1), 38–52.

Franzson, H., Gunnlaugsson, E., Árnason, K., Saemundsson, K., Steingrimsson, B., & Hardarson, B., 2010. The hengill geothermal system, conceptual model and thermal evolution, in *Proceedings World Geothermal Congress*.

Guest, T. & Curtis, A., 2011. On standard and optimal designs of industrial-scale 2-d seismic surveys, *Geophysical Journal International*, **186**(2), 825–836.

Gülünay, N., 2003. Seismic trace interpolation in the fourier transform domain, *Geophysics*, **68**(1), 355–369.

Gunnlaugsson, E. & Gíslason, G., 2005. Preparation for a new power plant in the hengill geothermal area, iceland, in *Proceedings World Geothermal Congress 2005, Antalya, Turkey*.

Haraldsdóttir, S. H., ranzson, H., & Árnason, K., 2012. Preliminary study of down-hole resistivity from 72 boreholes in the s-hengill geothermal field, sw-iceland, with respect to surface resistivity data and alteration minerals.

Hardage, B. A., DeAngelo, M. V., Murray, P. E., & Sava, D., 2011. *Multicomponent seismic technology*, Society of Exploration Geophysicists.

Hardarson, B., Einarsson, G. M., Kritsjánsson, B., Gunnarsson, G., Helgadóttir, H. M., Franzson, H., Árnason, K., Agutsson, K., & Gunnlaugsson, E., 2010. Geothermal reinjection at the hengill tripple juncion, sw iceland, in *Proceedings World Geothermal Congress, Bali, Indonesia*, pp. 25–29.

Herrmann, F. J. & Hennenfent, G., 2008. Non-parametric seismic data recovery with curvelet frames, *Geophysical Journal International*, **173**(1), 233–248.

Hestenes, M. R. & Stiefel, E., 1952. *Methods of conjugate gradients for solving linear systems*, vol. 49, NBS.

Jackson, G., Mason, I., & Greenhalgh, S., 1991. Principal component transforms of triaxial recordings by singular value decomposition, *Geophysics*, **56**(4), 528–533.

Jousset, P., Haberland, C., Bauer, K., & Arnason, K., 2011. Hengill geothermal volcanic complex (iceland) characterized by integrated geophysical observations, *Geothermics*, **40**(1), 1–24.

Julian, B. R. & Foulger, G., 1996. Earthquake mechanisms from linear-programming inversion of seismic-wave amplitude ratios, *Bulletin of the Seismological Society of America*, **86**(4), 972–980.

Kaelin, B., Guitton, A., et al., 2006. Imaging condition for reverse time migration, in *2006 SEG Annual Meeting*, Society of Exploration Geophysicists.

Kosloff, D., Reshef, M., & Loewenthal, D., 1984. Elastic wave calculations by the fourier method, *Bulletin of the Seismological Society of America*, **74**(3), 875–891.

Li, Y., 2013. Image-guided WEMVA for azimuthal anisotropy, *SEG Expanded Abstracts*, pp. 1–5.

Li, Y., Biondi, B., et al., 2011. Migration velocity analysis for anisotropic models, in *SEG Technical Program Expanded Abstracts*, pp. 201–206.

Li, Y., Shen, P., & Perkins, C., 2012. VTI migration velocity analysis using RTM, *SEG Expanded Abstracts*, pp. 1–5.

Li, Y., Biondi, B., Clapp, R., & Nichols, D., 2014. Wave-equation migration velocity analysis for vti models, *Geophysics*, **79**(3), WA59–WA68.

Marcinkovich, C. & Olsen, K., 2003. On the implementation of perfectly matched layers in a three-dimensional fourth-order velocity-stress finite difference scheme, *Journal of Geophysical Research*, **108**(B5), 18:1–16.

Marquardt, D. W., 1963. An algorithm for least-squares estimation of nonlinear parameters, *Journal of the Society for Industrial & Applied Mathematics*, **11**(2), 431–441.

Maurer, H., Curtis, A., & Boerner, D. E., 2010. Recent advances in optimized geophysical survey design, *Geophysics*, **75**(5), 75A177–75A194.

Menke, W., Brandsdottir, B., Jakobsdottir, S., & Stefansson, R., 1994. Seismic anisotropy in the crust at the mid-atlantic plate boundary in south-west iceland, *Geophysical Journal International*, **119**(3), 783–790.

Miller, A., Julian, B., & Foulger, G., 1998. Three-dimensional seismic structure and moment tensors of non-double-couple earthquakes at the hengill–grensdalur volcanic complex, iceland, *Geophysical Journal International*, **133**(2), 309–325.

Naghizadeh, M. & Sacchi, M. D., 2007. Multistep autoregressive reconstruction of seismic records, *Geophysics*, **72**(6), V111–V118.

Nemeth, T., Wu, C., & Schuster, G. T., 1999. Least-squares migration of incomplete reflection data, *Geophysics*, **64**(1), 208–221.

Popovici, A. M., 1996. Prestack migration by split-step dsr, *Geophysics*, **61**(5), 1412–1416.

Pratt, R. G., 1999. Seismic waveform inversion in the frequency domain, part 1: Theory and verification in a physical scale model, *Geophysics*, **64**(3), 888–901.

Purnell, G. W., 1992. Imaging beneath a high-velocity layer using converted waves, *Geophysics*, **57**(11), 1444–1452.

Rickett, J. E. & Sava, P. C., 2002. Offset and angle-domain common image-point gathers for shot-profile migration, *Geophysics*, **67**(3), 883–889.

Rodi, W. & Mackie, R. L., 2001. Nonlinear conjugate gradients algorithm for 2-d magnetotelluric inversion, *Geophysics*, **66**(1), 174–187.

Rondenay, S., Bostock, M., & Shragge, J., 2001. Multiparameter two-dimensional inversion of scattered teleseismic body waves 3. application to the cascadia 1993 data set, *Journal of Geophysical Research: Solid Earth (1978–2012)*, **106**(B12), 30795–30807.

Sava, P. & Biondi, B., 2004. Wave-equation migration velocity analysis. i. theory, *Geophysical Prospecting*, **52**(6), 593–606.

Schleicher, J., Costa, J. C., & Novais, A., 2008. A comparison of imaging conditions for wave-equation shot-profile migration, *Geophysics*, **73**(6), S219–S227.

Schneider, W. A., 1978. Integral formulation for migration in two and three dimensions, *Geophysics*, **43**(1), 49–76.

Shabelansky, A., Malcolm, A., & Fehler, M., 2012a. Monitoring seismic attenuation changes using a 4d relative spectrum method in athabsca heavy oil reservoir, canada, in *74th EAGE Conference & Exhibition*.

Shabelansky, A. H., 2007. *Full Wave Inversion*, Master's thesis, Tel Aviv University.

Shabelansky, A. H., Malcolm, A. H., & Fehler, M. H., 2011. Visibility analysis using reverse time wave sensitivity for time-lapse target-oriented imaging, in *2011 SEG Annual Meeting*.

Shabelansky, A. H., Malcolm, A., Fehler, M., & Bakku, S. K., 2012b. Seismic imaging of hydraulically-stimulated fractures: A numerical study of the effect of the source mechanism, in *2012 SEG Annual Meeting*, Society of Exploration Geophysicists.

Shabelansky, A. H., Fehler, M. C., & Malcolm, A. E., 2013a. Converted-phase seismic imaging of the hengill region, southwest iceland, *AGU Fall Meeting Abstracts*, p. A2461.

Shabelansky, A. H., Malcolm, A., & Fehler, M., 2013b. Data-driven estimation of the sensitivity of target-oriented time-lapse seismic imaging to source geometry, *Geophysics*, **78**(2), R47–R58.

Shabelansky, A. H., Malcolm, A., Fehler, M., Shang, X., & Rodi, W., 2013c. Converted phase elastic migration velocity analysis, in *2013 SEG Annual Meeting*, Society of Exploration Geophysicists.

Shabelansky, A. H., Bernabe, Y., Mok, U., & Evans, J., 2014a. Temperature influence on permeability of sioux quartzite containing mixtures of water and carbon dioxide, *International Journal of Rock Mechanics and Mining Sciences*, **70**, 546–551.

Shabelansky, A. H., Malcolm, A., Fehler, M., & Rodi, W., 2014b. Migration-based seismic trace interpolation of sparse converted phase micro-seismic data, in *2014 SEG Annual Meeting*, Society of Exploration Geophysicists.

Shabelansky, A. H., Malcolm, A., & Fehler, M., 2015a. Monitoring viscosity changes from time-lapse seismic attenuation: case study from a heavy oil reservoir, *Geophysical Prospecting*.

Shabelansky, A. H., Malcolm, A. E., Fehler, M. C., Shang, X., & Rodi, W. L., 2015b. Source-independent full wavefield converted-phase elastic migration velocity analysis, *Geophysical Journal International*, **200**(2), 954–968.

Shan, G. & Wang, Y., 2013. RTM based wave equation migration velocity analysis, *SEG Expanded Abstracts*, pp. 1–5.

Shang, X., de Hoop, M., & van der Hilst, R., 2012. Beyond receiver functions: Passive source reverse time migration and inverse scattering of converted waves, *Geophysical Research Letters*, **39**, 1–7.

Shen, P., 2004. *Wave equation migration velocity analysis by differential semblance optimization*, Ph.D. thesis, Rice University.

Shen, P., 2012. An RTM based automatic migration velocity analysis in image domain, *SEG Expanded Abstracts*, pp. 1–5.

Shen, P. & Simes, W., 2013. Subsurface domain image warping by horizontal contraction and its application to wave-equation migration velocity analysis, in *SEG, Expanded Abstracts*.

Shen, P. & Symes, W. W., 2008. Automatic velocity analysis via shot profile migration, *Geophysics*, **73**(5), VE49–VE59.

Spitz, S., 1991. Seismic trace interpolation in the fx domain, *Geophysics*, **56**(6), 785–794.

Stewart, R. R., 1991. Rapid map and inversion of p-sv waves, *Geophysics*, **56**(6), 859–862.

Stewart, R. R., Gaiser, J. E., Brown, R. J., & Lawton, D. C., 2003. Converted-wave seismic exploration: Applications, *Geophysics*, **68**(1), 40–57.

Stoer, J. & Bulirsch, R., 2002. *Introduction to numerical analysis*, vol. 12, Springer.

Stoffa, P., Fokkema, J. T., de Luna Freire, R., & Kessinger, W., 1990. Split-step fourier migration, *Geophysics*, **55**(4), 410–421.

Symes, W. & Carazzone, J. J., 1991. Velocity inversion by differential semblance optimization, *Geophysics*, **56**(5), 654–663.

Tarantola, A., 1984. Inversion of seismic reflection data in the acoustic approximation, *Geophysics*, **49**, 1259–1266.

Tarantola, A., 1986. A strategy for nonlinear elastic inversion of seismic reflection data, *Geophysics*, **51**(10), 1893–1903.

Tryggvason, A., Flóvenz, Ó. G., et al., 2002. Three-dimensional imaging of the p- and s-wave velocity structure and earthquake locations beneath southwest iceland, *Geophysical Journal International*, **151**(3), 848–866.

Valenciano, A., Biondi, B., et al., 2003. 2-d deconvolution imaging condition for shot-profile migration, in *73rd Ann. Internat. Mtg., Soc. of Expl. Geophys., Expanded Abstracts*, pp. 1059–1062.

Vidale, J. E., 1986. Complex polarization analysis of particle motion, *Bulletin of the Seismological society of America*, **76**(5), 1393–1405.

Vinnik, L., 1977. Detection of waves converted from p to sv in the mantle, *Physics of the Earth and planetary interiors*, **15**(1), 39–45.

Vinnik, L., Avetisjan, R., & Mikhailova, N., 1983. Heterogeneities in the mantle transition zone from observations of p-to-sv converted waves, *Physics of the earth and planetary interiors*, **33**(3), 149–163.

Virieux, J. & Operto, S., 2009. An overview of full-waveform inversion in exploration geophysics, *Geophysics*, **74**(6), WCC1–WCC26.

Vyas, M. & Tang, Y., 2010. Gradients for wave-equation migration velocity analysis, in *2010 SEG Annual Meeting*.

Wanjohi, A. W., 2007. Monitoring of microearthquakes and acoustic emissions within the hengill-hellisheidi geothermal reservoirs, june-august 2007.

Weibull, W. W. & Arntsen, B., 2013. Anisotropic migration velocity analysis using reverse-time migration, *Geophysics*, **79**(1), R13–R25.

Xiao, X. & Leaney, W., 2010. Local vertical seismic profiling (VSP) elastic reverse-time migration and migration resolution: Salt-flank imaging with transmitted P-to-S waves, *Geophysics*, **75**(2), S35–S49.

Yan, J., 2010. *Wave-mode separation for elastic imaging in transversely isotropic media*, Ph.D. thesis, Colorado School of Mines.

Yan, J. & Sava, P., 2009. Elastic wave-mode separation for vti media, *Geophysics*, **74**(5), WB19–WB32.

Yan, J. & Sava, P., 2010. Analysis of converted-wave extended images for migration velocity analysis, *SEG Expanded Abstracts*, pp. 1666–1671.

Yan, J. & Sava, P., 2011. Improving the efficiency of elastic wave-mode separation for heterogeneous tilted transverse isotropic media, *Geophysics*, **76**(4), T65–T78.

Zakharova, O. & Spichak, V., 2012. Geothermal fields of hengill volcano, iceland, *Journal of Volcanology and Seismology*, **6**(1), 1–14.

Zhang, Q. & McMechan, G. A., 2010. 2d and 3d elastic wavefield vector decomposition in the wavenumber domain for vti media, *Geophysics*, **75**(3), D13–D26.

Bibliography